A GEOMECHANICAL PROPERTY MODEL OF THE TRATTNACH OIL FIELD IN THE UPPER AUSTRIAN MOLASSE BASIN

Master's thesis

For the degree of Master of Science at Montanuniversitaet Leoben

Autor:
Katrin Schmid, BSc.
September, 2018

The work of this thesis was supervied by:
Univ.-Prof. Mag. rer. nat. Dr. mont. Reinhard F. Sachsenhofer
Dr. mont. Wilfried Gruber

.

Affidavit

I declare in lieu of oath, that I wrote this thesis and performed the associated research myself, using only literature cited in this volume.

Abstract

The Trattnach field was discovered in 1975 and produces oil from Cenomanian sandstones ever since. Multiple studies and investigations have been made for this area, concentrating mainly on the Cretaceous (Cenomanian) reservoir section. In this thesis a geomechanical model is established. It includes the crystalline basement and the entire basin fill reaching from Jurassic units to the Miocene sediments of the Innviertel Group. An existing reservoir model provided by RAG is extended and modified to fulfil the requirements to build a geomechanical grid. The geomechanical gridding is performed using the "Reservoir Geomechanics" plug-in from Schlumberger´s Petrel software package. The reservoir section and the additional under- and overlying horizons up to the earth's surface are now embedded in a cube of side- and underburden cells. These allow a smooth simulation using the VISAGE simulator, a finite-element geomechanics simulator developed by Schlumberger. Running such a simulation requires a reservoir simulation model and a geomechanic grid which is populated with geomechanic parameters like Young's-, bulk and shear modulus, as well as porosity and density data.

These parameters are calculated using geophysical log data provided by RAG, including compressional sonic velocities, gamma ray and various resistivity logs. The compressional sonic velocities are used to calculate missing density, porosity and shear sonic velocity data. Density logs are created by using Gardner's empirical relationship. Wyllie's time average equation is used for the missing porosity logs and the v_p-v_s relationship developed by Castagna is used for the calculation of shear sonic velocities.

With the shear-, compressional velocities and densities of a rock it is possible to calculate geomechanical parameters like Young's moduli, Poisson ratios, as well as shear and bulk moduli. Additionally performed laboratory measurements on core plugs of the reservoir rocks provide the uniaxial compressive strengths. The Jurassic limestones are the stiffest material with an averaged Young's modulus of 48 GPa, the seal rock of the CET1 formation has a averaged Young's modulus of 36 GPa and the reservoir rocks formed by the CET2 and CET3 formations have a averaged Young's modulus of 24 GPa.

The grid has been been populated with all input data combined and represents a new basis for further geomechanical studies concerning the Trattnach oil reservoir.

Kurzfassung

Das Ölfeld Trattnach wurde 1975 entdeckt und dient seither zur Ölproduktion. Zahlreiche Studien und Arbeiten zu diesem Ölfeld sind im Laufe der Zeit entstanden, welche sich allerdings hauptsächlich auf die kretazischen (cenomanen) Speichergesteine konzentrieren. Das in dieser Arbeit erstellte geomechanische Modell berücksichtigt die gesamte stratigrafische Entwicklung des oberösterreichischen Molassebeckens, vom Kristallin der Böhmischen Masse bis hin zu den miozänen Sedimenten der Innviertel-Gruppe. Als Grundlage dient ein von der RAG bereitgestelltes Reservoir Simulationsmodell. Dieses wurde im Rahmen dieser Arbeit erweitert und modifiziert um allen Anforderungen eines geomechanischen Modells zu entsprechen. Die Umwandlung vom Reservoir Modell zum geomechanischen Modell erfolgt in „Reservoir Geomechanics“ einem Plug-in des Petrel Software Paketes. Der geomechanische Raster bettet das originale Modell und die hinzugefügten seichteren Horizonte in einen Kubus von Simulationszellen ein. Diese werden mit geomechanischen Parametern befüllt und ermöglichen die Verwendung des von Schlumberger entwickelten Finite-Elemente Simulators VISAGE.

Als Grundlage für die Berechnung der geomechanischen Parameter dient ein von RAG bereitgestellter Datensatz an geophysikalischen Bohrlochdaten. Die Daten der Kompressionsgeschwindigkeiten wurden verwendet um die fehlenden Dichten, Porositäten und Scherwellengeschwindigkeiten zu berechnen. Die Dichtewerte wurden mittels Gardners empirischer Gleichung berechnet. Zur Ermittlung der Porositäten diente Wyllie’s „time-average“ Gleichung und die fehlenden Scherwellengeschwindigkeiten wurden mit der von Castagna entwickelten Kompressions-Scherwellengeschwindigkeitsbeziehung berechnet.

Mittels Dichte und Wellengeschwindigkeiten lassen sich die geomechanischen Parameter Elastizitäts-, Kompressions- und Schermodul, sowie die Poissonzahl berechnen. Die einaxiale Druckfestigkeit wurde an Kernproben der Speichergesteine im Labor ermittelt. Die jurassischen Karbonate haben mit einem gemitteltеten Elastizitätsmodul von 48 GPa die größte Gesteinsfestigkeit. Die Speichergesteine der CET2 und CET3 Einheiten haben einen gemittelten Elastizitätsmodul von 24 GPa und werden von der Einheit CET1, welche einen gemittelten Elastizitätsmodul von 36 GPa aufweist, abgedichtet.

Das neu erstellte geomechanische Modell wurde mit all diesen Parametern befüllt und dient nun als Grundlage für zukünftige gesteinsphysikalische Untersuchungen des Ölfeldes Trattnach.

CONTENTS

1 Introduction 7

2 Theoretical Background and Geological Setting 9

2.1 Geomechanical Background 9

2.1.1 Stress 9
2.1.2 Strain 11
2.1.3 Stress – Strain Relations 12
2.1.4 Principal Stress & Principal Coordinate System 15
2.1.5 Stress Regimes 16
2.1.6 Rock Strength 18
2.1.7 Interpretation of elastic moduli from uniaxial compression tests 20
2.1.8 Pore Pressure 22

2.2 Geological Setting 24

2.2.1 Basin fill 25
2.2.2 Stratigraphy 26
2.2.3 Petroleum Systems 29

2.3 The Trattnach Field 30

2.3.1 Production History 30
2.3.2 Field Structure and Geology 31
2.3.3 The Trattnach Reservoir 32

3 Dataset 35

3.1 Data Review and Organization 35

3.1.1 Well Data 35
3.1.2 Core Data 36
3.1.3 Model Data 36
3.1.4 Additional Data 37

4 Reservoir Model Setup 38

4.1 Grid 39

4.2 Horizons and Zones 39

4.2.1 Horizon modeling 40
4.2.2 Zonation 41

4.3 Layering 42

5 Geomechanical Model 44

5.1 Creating a Geomechanical Grid 44

5.1.1 Settings 44
5.1.2 Gridding 45

5.2 Property Modeling 50

5.2.1 Density Data 50
5.2.2 Porosity 56
5.2.3 Shear velocity data 62
5.2.4 Elastic properties 65
5.2.5 Uniaxial compressive strength 71

5.3 Grid Population 86
5.3.1 Upscaling 86
5.3.2 Data Analysis 88
5.3.3 Petrophysical Modeling 88
5.4 Geomechanical Material Modeling 90
5.4.1 Creating intact rock materials 90
5.4.2 Creating discontinuity materials 94
5.5 Populate Properties 95
6 Conclusion 100
7 List of Figures 101
8 List of Acronyms and Abbreviations 104
9 References 106
10 Appendix 109
10.1 Density Calculation 109
10.2 Porosity Calculation 110
10.3 Shear Sonic velocity Calculation 111
10.4 Core Plug Data 112
10.5 Well log plot TRAT1 113
10.6 Well log plot TRAT2 114
10.7 Well log plot TRAT3 115
10.8 Well log plot TRAT4 116
10.9 Well log plot TRAT6 117
10.10 Well log plot TRAT7 118
10.11 Well log plot TRAT8 119
10.12 Well log plot TRAT9 120
10.13 Well log plot TRAT10 121
10.14 Well log plot TRAT11 122
10.15 Well log plot TRAT12 123
10.16 Well log plot Weinberg1 124
10.17 Well log plot Gaspoldshofen1 125

1 INTRODUCTION

The role of geomechanics becomes steadily more important for the exploration and production of oil and gas (Dusseault, 2011). As the structurally and tectonically simpler fields are already developed, the industry is exploring at greater depths and targets reservoirs which are more challenging. A good geomechanical model can enable a better understanding of the hydrocarbon reservoir and is applicable during the entire exploration and production process. For example during the exploration stage, with the prediction of pore pressure or by interpretation of a potential leakage of the seal. The knowledge of pressure conditions helps to optimize the wellbore stability during the development phase. It is also applicable in the production phase, by monitoring and interpreting changes in reservoir performance. The increasing drive and willingness for a better understanding of geomechanical processes related to a hydrocarbon reservoir, led to the development of several geomechanical software packages. One of these are the Reservoir Geomechanics and VISAGE plug-in for the Petrel Software (Schlumberger, 2014). With these software packages it is now possible, in theory, to combine a geomechanical model with a reservoir model, enabling deeper insights in the behaviour of the reservoir reacting to geomechanical phenomena.

This study aims to create a first geomechanical model filled with all required properties to describe and model the geomechanical behaviour of the Trattnach area using this software package.

The Trattnach field was discovered in 1975 and produces oil ever since. It is the subject of multiple studies, but most of them concentrate on the Cenomanian reservoir section. Such a Cenomanian reservoir simulation model forms the foundation for this study. The scope of the study can be divided into three main tasks.

- The first task is the extension of the existing reservoir model up to earth's surface. The new model covers the entire basin fill from Jurassic sandstones up to the Miocene Innviertel Group. This model represents all geologic features including faults, stratigraphic formations and their zonation.
- The next task is to fill this model with all required petrophysical data, which enable the calculation of the geomechanical properties. The calculated density, porosity and sonic velocity data is assigned to the model and allows the calculation of all geomechanical parameters including Young's modulus, Bulk modulus and Poisson's ratio. A series of uniaxial compressive tests are performed to determine the uniaxial compressive strength of rock samples from the reservoir section.

- The last task involves the conversion of the geological model into a geomechanical model. The geological model is simplified to fulfil the requirements for a geomechanical grid, which is populated with all relevant geomechanical properties describing the different rock materials.

After the completion of all the above mentioned tasks the model can act as a foundation for further geomechanical simulations. This, however, would require an operational reservoir simulation model including the history matched production data and pressure changes, which is not available at moment.

Before going into further detail of the simulation dataset, the next section describes the important parameters and details of the studied oilfield.

2 THEORETICAL BACKGROUND AND GEOLOGICAL SETTING

2.1 GEOMECHANICAL BACKGROUND

This chapter summarizes some geomechanical principles which form the foundation of the following chapters and calculations. It starts with the basic principles of stress–strain relationships and how these can be connected to the propagation velocity of seismic waves. Further the different stress regimes during faulting are explained using Mohr Coulomb's failure criteria and rock strength. The last section of chapter 2.1 covers pore pressure.

2.1.1 Stress

Stress (σ) in its simplest form is force (F) acting on an area (A), therefore it can be assumed that by constant force the stress increases with decreasing area, Eq. 1 (Tipler, 1991).

$$\boldsymbol{\sigma = \frac{F}{A}} \qquad \textbf{Eq. 1}$$

When considering a sedimentary basin with almost horizontal surfaces and homogenous sediments the vertical stress represents the sediment thickness times density. However a basin is not uniformly filled and the simplification that bulk density (ρ_b) is constant over the sediment thickness can be improved when integrating the varying density over depth for each basin layer separately (Eq. 2). A rock at a depth z must have a normal compressive strength that is sufficient to support the weight of the overburden, the so called overburden stress (σ_v) (Jaeger et al., 1979; Zoback, 2014).

$$\boldsymbol{\sigma_v = \int_{z1}^{0} \rho_{z1} * g * z_1 + \int_{z2}^{z1} \rho_{z2} * g * z_2 + \ldots} \qquad \textbf{Eq. 2}$$

A rock body can be separated into rock matrix, formed by the mineral grains and pore space in between those grains, which can be filled either with water, oil or gas. Therefore the force acting on a body at depth depends not only on the weight of the overburden, but also on the weight of fluid in the pore space (Terzaghi, 1925). Eq. 3 shows that the total stress is a combination of effective stress σ'_v and pore pressure (P_p), which is explained in more detail in chapter 2.1.8.

$$\boldsymbol{\sigma_v = \sigma'_v + P_P} \qquad \textbf{Eq. 3}$$

Effective stress introduced by (Terzaghi, 1925) represents the stress transmitted through the grain framework and therefore governs the mechanical compaction. Sandstones for example can show high effective stresses due to the small grain to grain contacts. However forces do

not always act normal to a surface, in the case of oblique acting forces it is convenient to divide the force into their x and y-component (Jaeger et al., 1979).

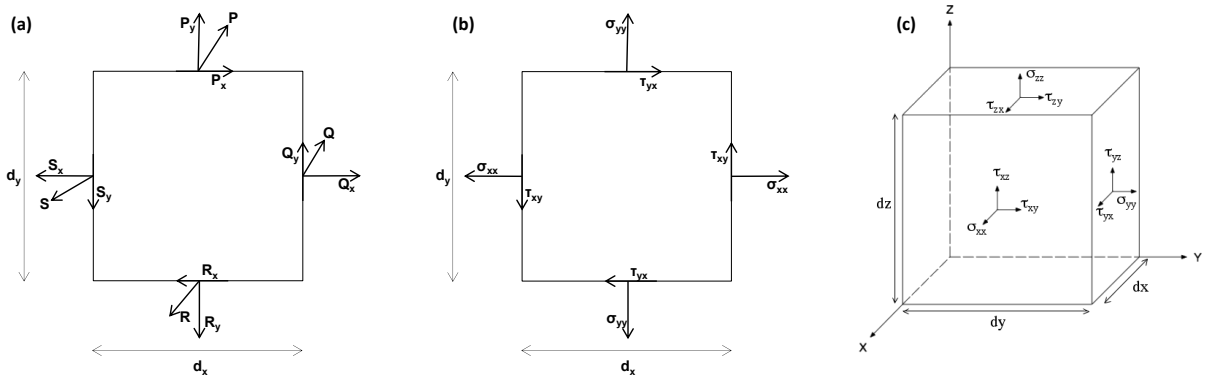

Fig. 2.1 Schematic Stress Tensor in 2D and 3D.
(a) Shows a two-dimensional rectangle with 4 oblique acting forces;
(b) Normal and shear stresses acting on a two-dimensional rectangle;
(c) Shear and normal stresses acting on a three-dimensional cube;

Fig. 2.1a shows a two-dimensional rectangle with four oblique acting forces. Splitting these four forces into their x and y components leads to four normal and four parallel acting forces. Dividing the normal forces P_y and R_y by d_y and S_x and Q_x by d_x results in the normal stresses σ_{yy} and σ_{xx}. The same is applied to P_x, R_x, Q_y and S_y, which tend to shear the body and therefore are called shear stresses (τ). For this thesis the notations σ_{ij} and τ_{ij} are used, i stands for the face the force is acting on and j for the face it is directing to (Fjar et al., 2008). Fig. 2.1b shows the stresses acting on the body and to fully describe this state of stress it is common to use the stress tensor notation. The same can be applied to a three dimensional cube, Fig. 2.1c, resulting in a stress tensor for the three dimensional case including nine stresses, see Eq. 4 (Fjar et al., 2008).

$$\boldsymbol{\sigma} = \begin{pmatrix} \boldsymbol{\sigma_{xx}} & \boldsymbol{\tau_{xy}} & \boldsymbol{\tau_{xz}} \\ \boldsymbol{\tau_{yx}} & \boldsymbol{\sigma_{yy}} & \boldsymbol{\tau_{yz}} \\ \boldsymbol{\tau_{zx}} & \boldsymbol{\tau_{zy}} & \boldsymbol{\sigma_{zz}} \end{pmatrix} \qquad \textbf{Eq. 4}$$

Three normal stresses forming the diagonal plane and six shear stresses off-diagonal. The rows describe the planes the force is acting on and the columns correspond to the direction of the forces. Geomechanics deals with static, non-moving bodies, allowing the assumption of rotational and translational equilibrium. Due to rotational equilibrium, τ_{xy} must be equal but opposite to τ_{yx}. The fact that τ_{xy} equals τ_{yx}, τ_{xz} equals τ_{zx} and τ_{yz} equals τ_{zy} reduces the number of stresses to fully describe the stress state to six (Fjar et al., 2008).

$$\boldsymbol{\sigma} = \begin{pmatrix} \boldsymbol{\sigma_{xx}} & \boldsymbol{\tau_{xy}} & \boldsymbol{\tau_{xz}} \\ \boldsymbol{\tau_{xy}} & \boldsymbol{\sigma_{yy}} & \boldsymbol{\tau_{yz}} \\ \boldsymbol{\tau_{xz}} & \boldsymbol{\tau_{yz}} & \boldsymbol{\sigma_{zz}} \end{pmatrix} \qquad \textbf{Eq. 5}$$

Independend whether a body is exposed to one or three demensional stress, it will deform in a certain amount due to the acting stress, this deformation is called strain.

2.1.2 Strain

Strain is a quantity of deformation due to stress acting on a body. Depending on the orientation of the stress, this deformation can be a change of shape or change of size. A change of shape is characteristic for shear deformation, whereas a change of size is an indication for compressive or tensile strain (Kearey et al., 2002). In Fig. 2.2 all different kinds of strain are displayed and the sketches show how compressive stress leads to a reduction in size, whereas tensile stress results in an extension of the body. In general strain (ε) is measured by dividing the change of length (Δl) by the original length (l_0) (see Eq. 6) (Tipler, 1991).

$$\varepsilon = \frac{\Delta l}{l_0} \qquad \text{Eq. 6}$$

For geomechanic purposes, tensile stress and strain can be neglected, because the tensile strength of rock is so low, that tensile stresses cannot be supported in earth (Zoback, 2014). Another reason is the presence of pore fluid, the least compressive stress cannot have equal or lower values than the prevailing pore pressure. Otherwise the earth would self hydrofrack, so just sufficiently large compressive stresses are allowed (Zoback, 2014).

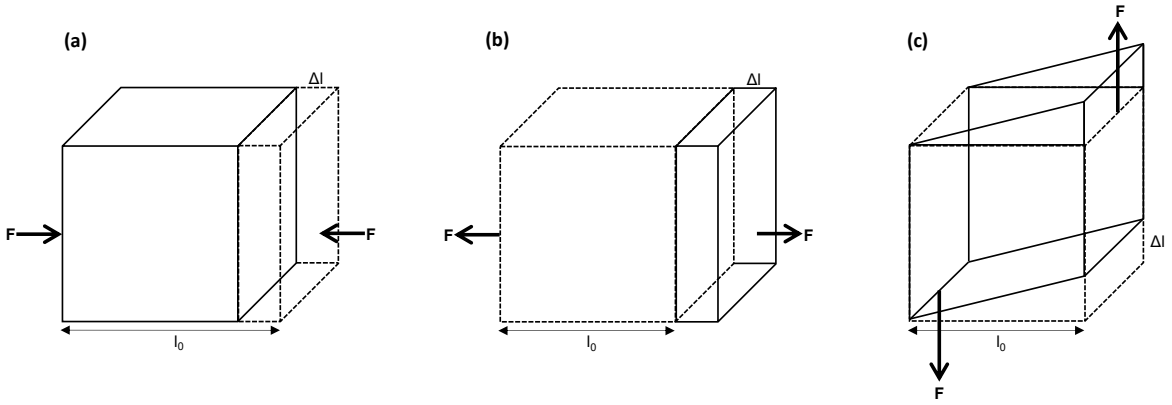

Fig. 2.2 Types of strain.
(a) Compressive strain as a result of compressive stress;
(b) Tensile strain as a result of tensile stress;
(c) Shear strain due to shear stress;

2.1.3 Stress – Strain Relations

There are various models to describe the relationship between stress and strain, these constitutive behaviours describe how stress and strain are connected for a specific material under load. The existing constitutive models describe the materials responses in either the case of elasticity, plasticity, viscosity and creep or a combination of these models. Each constitutive model has a set of equations to describe the relation of stress and strain (Brady et al., 1999).
This thesis, concentrates on elasticity, which is the most common constitutive behaviour and a very useful tool for describing rock behaviour and especially the behaviour of seismic waves. A rock subjected to stress strains, which means that the rock changes in shape and / or size, if this deformation vanishes after the stress is released one speaks of elastic deformation (Kearey et al., 2002). Elastic deformation can be compared to Hook's law, which states that up to a certain limit of stress, the so called yield strength, stress can be assumed to be directly proportional to strain. Exceeding the yield strength leads to non-linear and partly irreversible strain, described as ductile or plastic deformation, depending on the rock behaviour. Further stress increase would lead to failure (Kearey et al., 2002).
The most interesting deformation in the case of geophysics and geomechanics is the elastic deformation, because seismic waves show an elastic behaviour when propagating in earth. In more detail, they can be described as bundles of elastic strain energy that propagate in radial direction from a seismic source. This assumption is not true in the immediate vicinity of the seismic source, like an explosion (Kearey et al., 2002). The elastic behaviour of waves makes it very convenient to describe the seismic velocities by the elastic moduli and the density of the rocks through which they travel (see Eq. 9) (Yilmaz, 2001). An elastic modulus is a material specific parameter, derived from the constitutive equations for an elastic material. These are based on a generalized Hook's law, where the stiffness tensor or elasticity tensor [c_{ij}] describes the stress-strain relation in a more complex three-dimensional way (see Eq. 7). The elasticity tensor is a fourth order tensor with 21 independent constants, but for an isotropic solid with infinitesimal small deformations, just two constants remain independent. Simplifying the elasticity tensor from 21 to 2 independent constants leads to Eq. 8, where μ and λ are elastic moduli, which describe the linear relationship between stress and strain (Yilmaz, 2001).

$$\begin{bmatrix}\sigma_{xx}\\ \sigma_{yy}\\ \sigma_{zz}\\ \sigma_{xy}\\ \sigma_{yz}\\ \sigma_{zx}\end{bmatrix} = \begin{bmatrix}c_{11} & c_{12} & c_{13} & c_{14} & c_{15} & c_{16}\\ c_{21} & c_{22} & c_{23} & c_{24} & c_{25} & c_{26}\\ c_{31} & c_{32} & c_{33} & c_{34} & c_{35} & c_{36}\\ c_{41} & c_{42} & c_{43} & c_{44} & c_{45} & c_{46}\\ c_{51} & c_{52} & c_{53} & c_{54} & c_{55} & c_{56}\\ c_{61} & c_{62} & c_{63} & c_{64} & c_{65} & c_{66}\end{bmatrix} * \begin{bmatrix}\varepsilon_{xx}\\ \varepsilon_{yy}\\ \varepsilon_{zz}\\ \varepsilon_{xy}\\ \varepsilon_{yz}\\ \varepsilon_{zx}\end{bmatrix} \quad \textbf{Eq. 7}$$

$$\begin{bmatrix}\sigma_{xx}\\ \sigma_{yy}\\ \sigma_{zz}\\ \sigma_{xy}\\ \sigma_{yz}\\ \sigma_{zx}\end{bmatrix} = \begin{bmatrix}\lambda+2\mu & \lambda & \lambda & 0 & 0 & 0\\ \lambda & \lambda+2\mu & \lambda & 0 & 0 & 0\\ \lambda & \lambda & \lambda+2\mu & 0 & 0 & 0\\ 0 & 0 & 0 & 2\mu & 0 & 0\\ 0 & 0 & 0 & 0 & 2\mu & 0\\ 0 & 0 & 0 & 0 & 0 & 2\mu\end{bmatrix} * \begin{bmatrix}\varepsilon_{xx}\\ \varepsilon_{yy}\\ \varepsilon_{zz}\\ \varepsilon_{xy}\\ \varepsilon_{yz}\\ \varepsilon_{zx}\end{bmatrix} \quad \textbf{Eq. 8}$$

There are various elastic moduli depending on the orientation of strain and stress, e.g. the bulk modulus (K) describing the relationship of volumetric stress and the resulting volumetric strain or the shear modulus (μ), describing the linkage between shear stress and shear strain (Kearey et al., 2002). Eq. 9 indicates an inversely proportional relationship between seismic wave velocity and density, however in most cases an increase in density leads to higher velocities. This can be explained by the fact that an increasing density is followed by an increasing ability to resist compressional and shear stresses and therefor results in a higher value for the elastic moduli (Yilmaz, 2001).

$$\boldsymbol{\nu = \sqrt{\frac{\text{appropriate elastic modulus of material}}{\text{density of material } \rho}}} \quad \textbf{Eq. 9}$$

Seismic waves can be divided in body waves and surface waves. Body waves are important for seismic acquisitions, because they travel through the internal volume of a body. The second type are surface waves, they propagate along boundaries and are important for earthquake analysis. Body waves are divided into two groups, one being shear waves and the other are compressional waves (Kearey et al., 2002).

Shear Waves

Shear waves are a result of shear stress and characterized by particle movement perpendicular to the direction of propagation, see Fig. 2.3a. The shear stress causes a change in particle shape, the so-called shear strain, which defines the shear modulus (μ), see Eq. 11 and Fig. 2.3b. The more the rock resists shear stress the higher is the shear modulus and consequently the shear wave velocity Eq. 11 (Yilmaz, 2001).

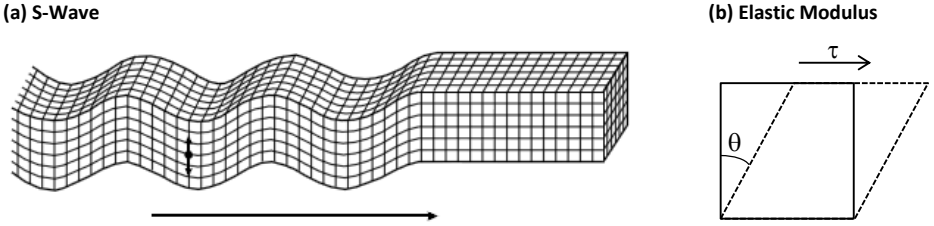

Fig. 2.3 **Elastic deformation caused by shear waves (after Kearey et al., 2002).**
(a) Elastic deformation and ground particle movement associated with the passage of a shear wave;
(b) Components forming the elastic shear modulus

$$\mu = \frac{\text{shear stress } \tau}{\text{shear strain } \tan\theta} \qquad \text{Eq. 10}$$

$$v_s = \sqrt{\frac{\mu}{\rho}} \qquad \text{Eq. 11}$$

Compressional Waves

Compressional waves are induced by a compressional stress and characterized by a particle movement in the direction of the wave propagation, see Fig. 2.4a. The compressional or volume stress cause a change in particle size, see Eq. 12 and Fig. 2.4b, which define the bulk modulus. The more the rock resists the compressional stress the higher is the bulk modulus and consequently the compressional wave velocity, see Eq. 13 (Yilmaz, 2001).

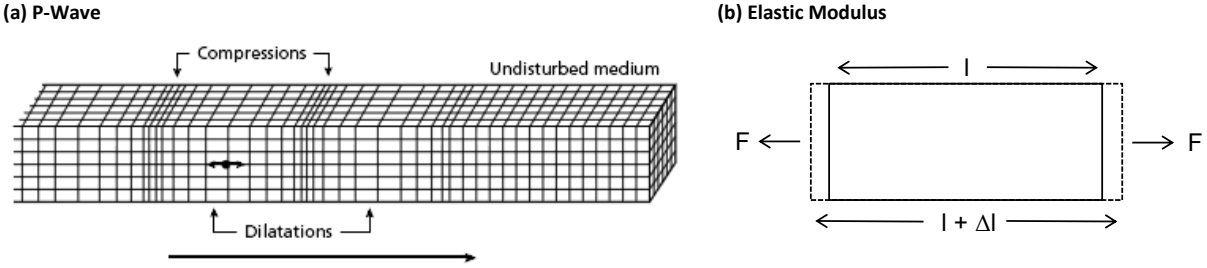

Fig. 2.4 **Elastic deformation caused by compressional waves (after Kearey et al., 2002).**
(a) Elastic deformation and ground particle movement associated with the passage of a compressional wave;
(b) Components forming the elastic bulk modulus;

$$K = \frac{\text{volume stress } P}{\text{volume strain } \frac{\Delta V}{V}} \qquad \text{Eq. 12}$$

$$v_p = \sqrt{\frac{K + \frac{4}{3}\mu}{\rho}} \qquad \text{Eq. 13}$$

So the knowledge of seismic wave velocities and the densities they travel through is a useful tool to calculate the compressional and shear moduli. Also most of the modern sonic tool measurements provide the full digital wave train, including compressional, shear and Stonley wave arrival times, thus the velocity – elastic moduli can be calculated directly from the well log measurements (Kearey et al., 2002).

2.1.4 Principal Stress & Principal Coordinate System

In a principal coordinate system no shear stress acts along the three orthogonal planes and all present stresses are normal stresses, acting in the direction of the principal axes. Each of them has equal-magnitude but an oppositely directed force component (Kearey et al., 2002). A principal coordinate system is defined, by rotating the initial coordinate system until all shear stresses disappear (Jaeger et al., 1979). This rotation leads to three normal stresses acting on a rock body, the so called principal stresses (Fig. 2.5). Eq. 14 shows that the stress tensor gets even simpler containing just the three normal stresses, being the first big advantage of a principal coordinate system (Zoback, 2014).

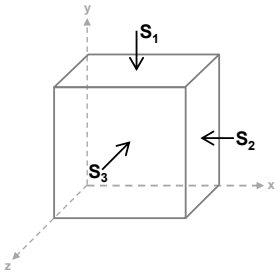

$$\sigma = \begin{pmatrix} \boldsymbol{S1} & \mathbf{0} & \mathbf{0} \\ \mathbf{0} & \boldsymbol{S2} & \mathbf{0} \\ \mathbf{0} & \mathbf{0} & \boldsymbol{S3} \end{pmatrix} \qquad \textbf{Eq. 14}$$

Fig. 2.5 Principal Coordinate System.
S1, S2 and S3 are the principal stresses acting on a rock, parallel to the 3 principal axes.

Another advantage is that a principal coordinate system is particularly good for describing the state of stress in the earth, because the earth's surface is either in contact with water or air and both of them cannot support shear stresses. The fact that a principle plane is a plane where the shear stress vanishes, makes defining a principal coordinate system very convenient for geomechanical applications. In close proximity to the earth's surface one principal stress is vertical and two are horizontal, like in Fig. 2.5, this concept can be applied to hydrocarbon reservoirs, considering the relatively big earth surface compared to a common reservoir depth. After computing the geomechanical calculations in the principal coordinate system, the stresses are mathematically transformed into the insitu coordinate system. This transformation is done by computer software (Zoback, 2014).

2.1.5 Stress Regimes

E.M. Anderson discovered in the 1930s that the stress field is a result of geologic processes which can be categorized into three major stress regimes (Anderson, 1951). These stress regimes are based on the fact that the three principal stresses vary in magnitude according to the prevailing geologic process. As mentioned in chapter 2.1.4 the principal stresses effecting a rock at depth are divided into one vertical stress (S_v) and two horizontal stresses, the maximum principal horizontal stress (S_{Hmax}) and the minimum principal horizontal stress (S_{hmin}). Variations of these three stresses Sv, SHmax and Shmin result in different faulting regimes. They can be described as either a normal faulting regime (NFR), strike-slip faulting regime (SSFR) or a reverse faulting regime (RFR), depending the biggest of these three stresses (Anderson, 1951; Zoback, 2014). Some assumptions count for all stress regimes, like the stresses under the earth's surface are always compressive, the least principal stress ought to be greater than the pore pressure, otherwise the earth would self hydrofrac and the strength of pre-existing faults will always limit the existing stress magnitudes (Zoback, 2014).

Normal Faulting Regime

A normal faulting regime is characterized by a down moving hanging wall with respect to the foot wall, occurring when maximum principal stress is vertical (Anderson, 1951; Zoback, 2014). Fig. 2.6 shows an extensional fault, which strikes in the direction of the maximum horizontal stress (S_{Hmax}) being the intermediate stress and dips in the direction of the minimum horizontal stress (S_{hmin}), which represents the least principal stress. Faulting occurs if the vertical stress is sufficiently larger than the minimum horizontal stress, $S_v > S_{Hmax} > S_{hmin}$ (Fig. 2.6) (Zoback, 2014).

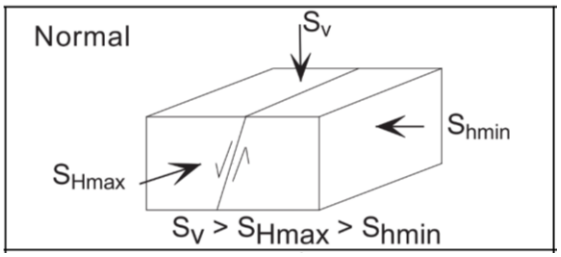

Fig. 2.6 Schematic Normal Fault.
Extensional fault, which strikes in the direction of S_{Hmax} and slip in the direction of S_{hmin}, (after Zoback , 2014)

Strike Slip Faulting Regime

In a strike slip faulting regime the faults are nearly vertical and develop with an angle of 30 degree in respect to the maximum horizontal stress, which in this case forms the maximum principal stress, see Fig. 2.7. As a result, the vertical stress forms the intermediate stress and the minimum horizontal stress the least principal stress. In this case faulting occurs, if the maximum horizontal stress is sufficiently larger than the minimum horizontal stress, $S_{Hmax} > S_v > S_{hmin}$ (Fig. 2.7) (Anderson, 1951; Zoback, 2014).

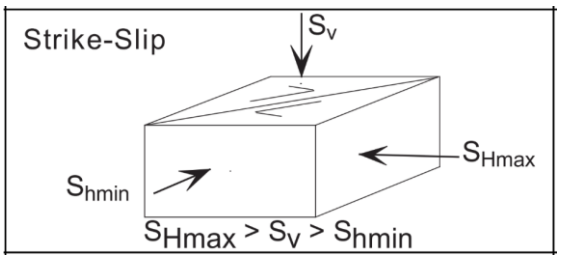

Fig. 2.7 Schematic Strike Slip Fault.
These are nearly vertical faults, which strike in approximately 30 degrees to S_{Hmax} (after Zoback, 2014)

Reverse Faulting Regime

A reverse faulting system is the most compressive stress state in earth, because both horizontal stresses exceed the vertical stress (Sv), which forms in this case the least principal stress. In this stress regime, the hanging wall moves up with respect to the foot wall and the fault dips with 30 degrees in the direction of the maximum horizontal stress, see Fig. 2.8. Faulting occurs if $S_{Hmax} > S_{hmin} > S_v$ (Anderson, 1951; Zoback, 2014).

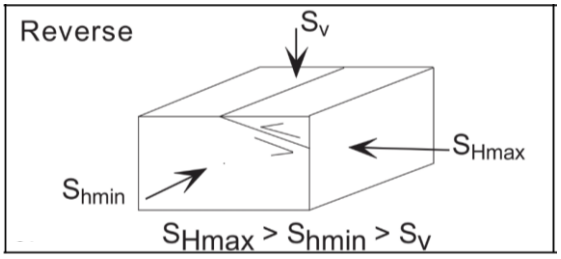

Fig. 2.8 Schematic Reverse Fault.
Reverse faults strike in the direction of S_{hmin} and dip about 30 degrees in the direction of S_{Hmax} (after Zoback, 2014)

2.1.6 Rock Strength

Andersons faulting theory can be combined with Mohr Coulombs Failure criteria (Anderson, 1951; Jaeger & Cook, 1979; Zoback, 2014), plotting the almost always known vertical stress can be a good and useful tool for identifying the current faulting regime. The Mohr circle construction, see Fig. 2.9b, is a graphical evaluation of prevailing shear stress (τ_f) and effective normal stress (σ_N) during a fault formation, due to the applied principal stresses σ_1 and σ_3. To measure these applied stresses a triaxial test is performed, it is a common procedure for rock strength analysis. Fig. 2.9a shows a schematic illustration of such a triaxial test, a cylindrical rock sample is put into an apparatus and subjected to controlled stresses until a shear plane forms. This test describes the situation at depth sufficiently well, with σ_1 reflecting the overburden pressure S_v and σ_3 the confining pressure.

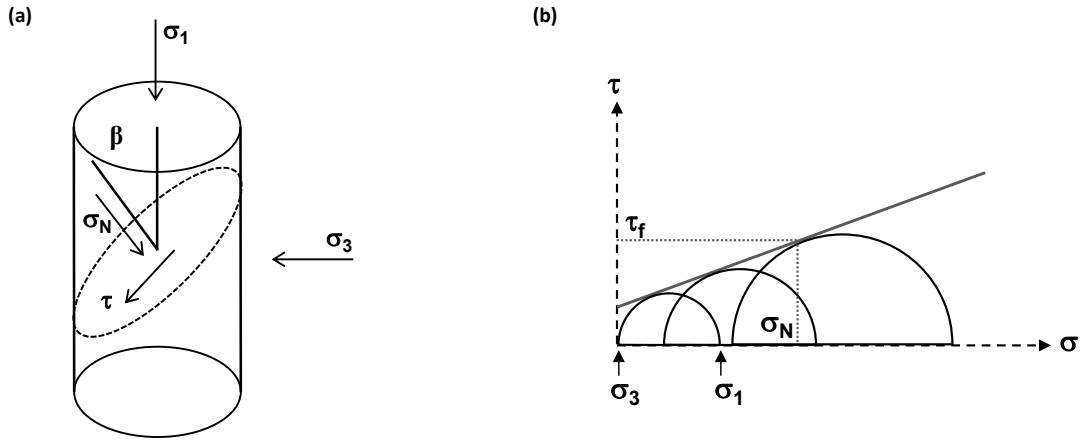

Fig. 2.9 **Triaxial Test and Mohr Circle Construction.**
(a) shear and effective normal stress acting on a fault plain, which forms at an angle β to the main principal stress;
(b) Mohr circles and envelope as a result of a series of triaxial tests

Fig. 2.10 shows the plotted stress – strain data from a triaxial test. Starting with axial loading the cracks of the rock sample begin to close, once all these cracks are closed the rock exhibits linear elastic behaviour, in other words the rock strains linearly in response to the applied stress. Each rock type has a characteristic elastic behaviour, represented by its Young's modulus (E), shales can reach values of 60 GPa, sandstones 70 GPa and limestones up to 100 GPa. Due to further loading elastic behaviour cannot be maintained and the deformation starts to become inelastic, so the rock matrix begins to break in an irreversible, permanent manner. At some point, in Fig. 2.10 at about 45 MPa, the yield strength of the rock is reached this is indicated by the onset of failure, where the sample loses its ability to support the applied stress. Failure can be either gradual for ductile materials, such as poorly cemented sands or very abrupt in the case of brittle materials due to formation of a shear plain (Zoback, 2014).

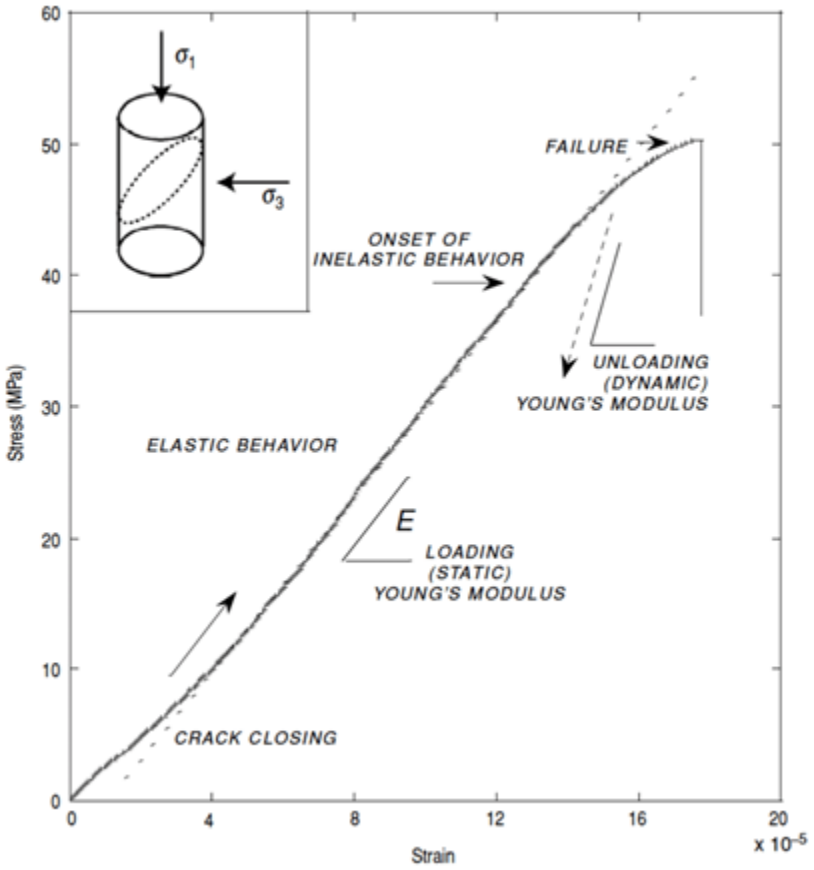

Fig. 2.10 Triaxial Test / Stress – Strain Diagram (Zoback, 2014).

The fact that the sample strength increases monotonically with increasing confining pressure makes it very convenient to display the test results in Mohr Circles. As seen in Fig. 2.9b the shear stress is plotted on the vertical and effective normal stress on the abscissa. Plotting the different circles in a τ / σ diagram leads to a Mohr failure envelope, which is the result of a series of triaxial tests performed at different confining pressures and marks the upper limit of rock strength (Jaeger et al., 1979; Zoback, 2014).

Looking at the Mohr Circles some predictions can be easily made. The most important one is that all allowable stress states do not intersect with the Mohr envelope and because failure would have occurred prior. Another important aspect is the pore pressure influence, with increasing pore pressure the stress magnitudes will decrease, Mohr Circles will shift towards left, because we plot effective normal stresses on the horizontal axis, $\sigma_N = S_V - P_P$ (Zoback, 2014).

The shear and effective normal stress depend not only on the principal stresses and pore pressure, but also on the orientation of the fault with respect to the principal stress. This results in characteristic Mohr Circles for each faulting regime, see Fig. 2.11. All circles are based on two assumptions, an internal coefficient of friction (μ) of 0.6, the same depth and same values

for S_v. Normal faulting allows the smallest stress magnitudes and is characterized by the lowest possible value for S_{hmin}. In reverse faulting the vertical stress is the least principal stress and therefore characterized by the largest possible Mohr circles, or highest values for S_{Hmax}. Strike slip faulting represents intermediate stress magnitudes and is often combined with normal or reverse faulting (Zoback, 2014).

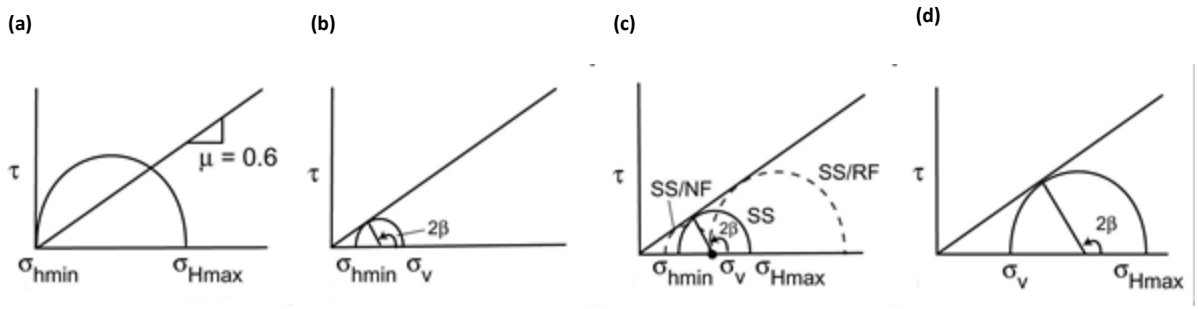

Fig. 2.11 Mohr Failure criteria for different faulting regimes (after Zoback, 2014).
(a) General assumption of 0.6 for the internal coefficient of friction and zero cohesion;
(b) Normal faulting regime; (c) Strike slip faulting regime and (d) Reverse faulting regime

2.1.7 Interpretation of elastic moduli from uniaxial compression tests

By executing a uniaxial compression test, the elastic modulus can be interpreted using the strain stress curve. Such a stress-strain curve is the result of either a triaxial test or the simplified uniaxial compression test, where the sample is subjected to an axial load with zero confining pressure. The applied axial stress is plotted versus the axial deformation ($\Delta\varepsilon_z$) and the peak stress marks the unconfined compressive strength (UCS) (Fjar et al., 2008). The slope of the linear part of the stress-strain curve allows the calculation of Young's modulus using Eq. 15.

$$\mathbf{E} = \frac{\boldsymbol{\Delta\sigma_z}}{\boldsymbol{\Delta\varepsilon_z}} \qquad \textbf{Eq. 15}$$

If the samples are sufficiently large, with a minimum length of 60 mm, an extensometer is mounted, which measures the radial deformation ($\Delta\varepsilon_R$). This enables the calculation of the Poisson's ratio (ν) using Eq. 16.

$$\boldsymbol{\nu} = -\frac{\boldsymbol{\Delta\varepsilon_R}}{\boldsymbol{\Delta\varepsilon_z}} \qquad \textbf{Eq. 16}$$

In case of a nonlinear stress-strain response the Young's modulus can be interpreted as a secant, tangent or initial modulus, Fig. 2.12 (Fjar et al., 2008).

- The initial modulus (E_I) represents the initial slope of the stress-strain curve.
- The secant modulus (E_S) is a measure from the origin up to a chosen percentage of the uniaxial compressive strength.
- The tangent modulus (E_T) is the slope of the stress-strain response at a specific percentage (commonly at 50% of the uniaxial compressive strength).

The uniaxial compressive strength is strongly influenced by the inheterogeneities of a rock sample, a careful sample preparation is key for representative uniaxial compression tests, because flaws and cracks can reduce the rock strength immensely (Witt, 2008).

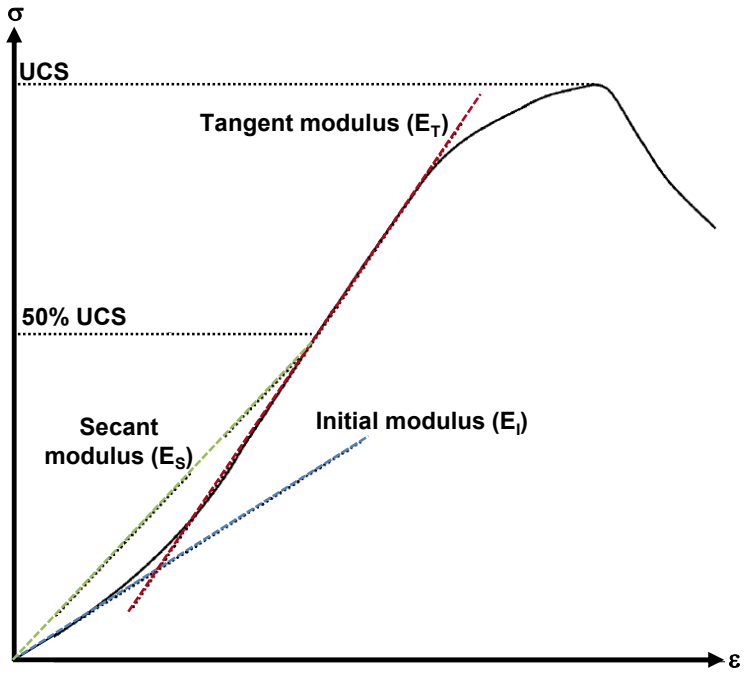

Fig. 2.12 **Three ways to calculate elastic moduli from an axial strain-stress curve (black). Secant modulus (E_S) (green), Initial modulus (E_I) (blue), Tangent modulus (E_T) (red). Uniaxial compressive strength (UCS) and the 50% value of UCS are marked (after Fjar et al., 2008)**

2.1.8 Pore Pressure

During drilling or reservoir analysis it is essential to understand the behavior of fluids present in the rocks. A good tool is the analysis of pore pressure and pressure gradients, these allow fluid type prediction and indication of overpressure zones, which can be fatal for wellbore drilling (Zoback, 2014). Fluid pressure is isotropic, hence the pressure is transmitted through the whole fluid and has the same value in all directions. Therefore, pore pressure depends just on the height of the water column and the density of the fluid. The resulting unit kg/cm² is not very common in oil industry, but can be converted into psi with the conversion factor of 14.2233 psi which corresponds to 1 kg/cm² (Rider et al., 2011). Normal pressure or hydrostatic pore pressure is calculated as seen in Eq. 17 and increases with 10 MPa/km, corresponding to 0.44 psi/ft for freshwater. This value can vary for other water salinities.

$$\mathbf{P_P^{hydro}} = \int_{\mathbf{z}}^{\mathbf{0}} \boldsymbol{\rho_w(z)gdz} \approx \boldsymbol{\rho_w g z_w} \qquad \textbf{Eq. 17}$$

A classic result of pore pressure measurements in a sedimentary basin, see Fig. 2.13, shows the usefulness of pore pressure gradients. At a first glance, one can divide the underground in three different pressure zones, characterized by three distinct rates of pressure increase with depth (Zoback , 2014). The proportionality of the insitu fluid and the gradient allows gas and oil detection, due to the different pressure gradients (Rider et al., 2011).

Pressure zone one from 0 to 8300 ft represents the hydrostatic zone, this implies an interconnected pore space and fracture network from bottom to earth surface, since hydrostatic pressure can exist only as long as there is a connectivity and permeability among the pore space at depth and the surface. At 8300 ft the pore pressure starts to increase rapidly and a pressure barrier, for example an impermeable shale, isolates this zones from the shallower above, otherwise it would equilibrate. Beginning with pressure zone two, the measurements are in the overpressure zone, which is defined as any pressure above the normal. A water gradient in an overpressure zone is the same as for the hydrostatic zone, just the absolute (over)pressure is higher. For example the fast burial of fluid filled sediments, can lead to overpressure if the fluid cannot escape in time. Furthermore overpressure results in lower effective stresses and decelerates mechanic compaction (Zoback, 2014).

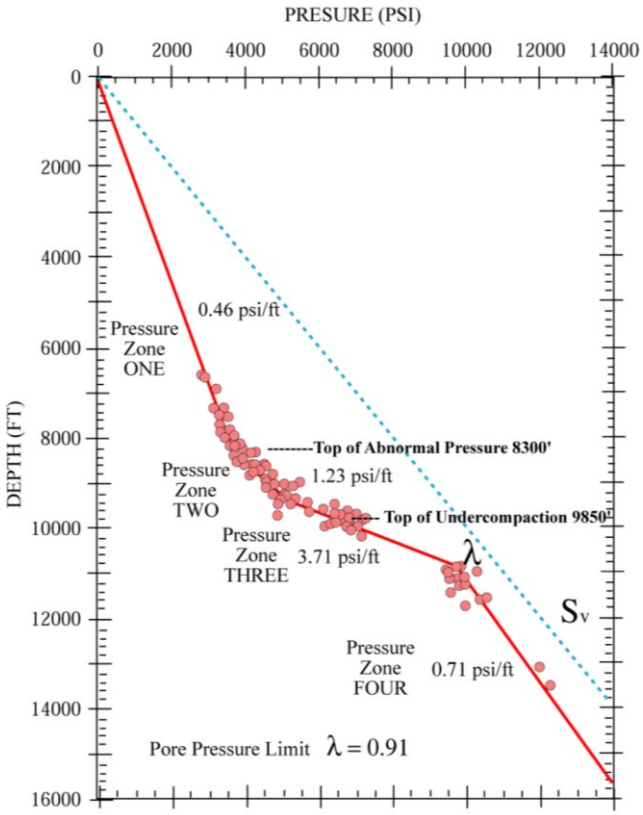

Fig. 2.13 **Pore Pressure Measurements (Zoback, 2014).**
Red line indicates the pore pressure gradient and the dotted blue line the overburden stress gradient (S_v) or lithostatic gradient.

Subsequently underpressure is characterized by values lower than normal pressure and is often a result of uplift (Bjørlykke, 2015). At the transition from pressure zone three to four the pore pressure reaches a level close to the overburden pressure or lithostatic gradient, indicated by the blue dotted line. The lithostatic gradient depends on rock density and marks the highest possible pressures in a well and forms the upper boundary for overpressure. Plotting the hydrostatic gradient and lithostatic gradient in a diagram with pressure versus depth, generates a window in which all possible formation pressures must lie (Rider et al., 2011). Another option is to calculate the ratio of pore pressure and overburden pressure with Eq. 18, in the case of Fig. 2.13 a pore pressure limit of 0.91 is reached (Zoback, 2014).

$$\lambda = \frac{P_p}{S_v}, \qquad \textbf{Eq. 18}$$

Looking at fluid saturated rocks a second constitutive law is of importance, because a porous fluid saturated rock shows poroelastic behavior. In contrast to elasticity this law considers the fact that the stiffness of saturated rocks depends on the rate the external forces are applied. In more detail fast loading results in apparently higher stiffness, because the porewater cannot drain fast enough and carries some of the applied stress. Whereas slow loading leads to a similar rock stiffness as if no fluids are present (Zoback, 2014).

2.2 GEOLOGICAL SETTING

The study area of the Trattnach Oil Field is part of the North Alpine Foreland Basin, Fig. 2.14, also referred to as the Molasse Basin. Located north of the Alpine fold and thrust belt, the Molasse Basin forms a peripheral basin with a lateral extent of 700 km, beginning in western French Savoie and ending in Lower Austria. Fig. 2.14 shows the entire geographic extent and its division into a western, central and eastern part. The Trattnach oil field is located in the eastern part, where the Bohemian Massif and North Alpine thrust belt lie close together. It is an asymmetric basin with a maximum width of 150 km in Germany, whereas the western and eastern parts reach only 20 km (Sissingh, 1997).

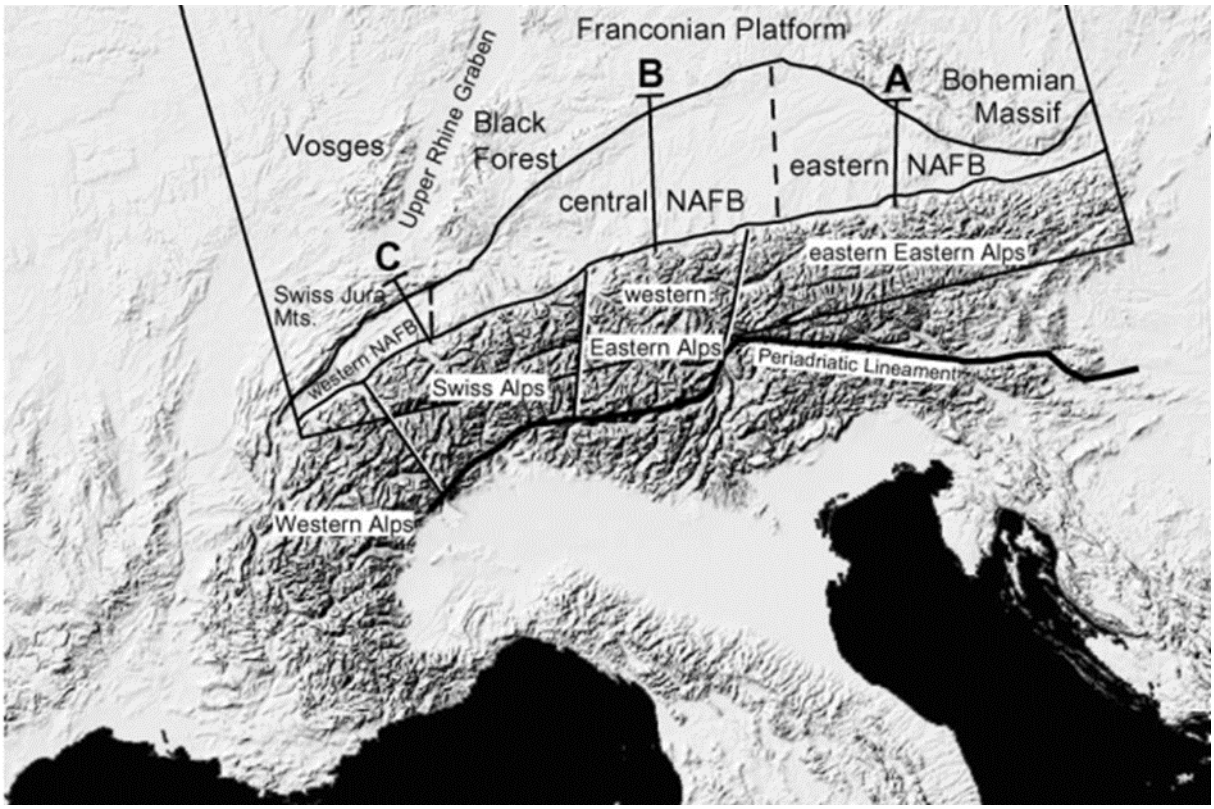

Fig. 2.14 Digital Elevation Model of central Europe.
The North Alpine Foreland Basin (NAFB) is divided into a western, central and eastern part (Kuhlemann, et al., 2002)

The Austrian sector of the Molasse Basin is characterized by an asymmetric basin geometry, which is dominated by the outcropping basement of the Bohemian Massif in the north and the Alpine thrust front in the south. Basically, the basin fill represents three marine regression and transgression cycles (Wagner, 1996). The first cycle, from early Jurassic in the east to middle Jurassic and early Cretaceous times in the west, correlates with the Arctic – North Atlantic rifting and the basin was part of the middle European platform (Wagner, 1998; Ziegler, 1982). Upper Cretaceous sandstones and glauconitic shales represent the second cycle, which ended in early Eocene times, initiated through the collision of the Alps with the southern margin of

the European platform. Due to the Alpine orogeny the North Alpine Foreland Basin was formed and the basin infill from late Eocene to present is summarized as the third cycle (Wagner, 1998; Ziegler, 1982)

2.2.1 Basin fill

The basin fill ranges from Mesozoic rocks at the bottom up to Miocene sediments at the top. Fig. 2.15 shows a generalised north - south cross section through the eastern part of the Molasse Basin. The crystalline basement at the bottom is followed by Jurassic carbonates and upper Cretaceous sediments. The Eocene layer marks the actual beginning of Molasse evolution which continued up to the Freshwater Molasse at the top. During the Alpine orogeny the African continental plate overthrusted the European plate, as a result the loading of the stacked plates led to a flexural downbending of the European plate in front of the thrust belt (Andeweg et al., 1998). This deformation changed the basin shape to its present day geometry, with a steep tectonically active slope in the south and a wide stable slope in the north (De Ruig, 2003).

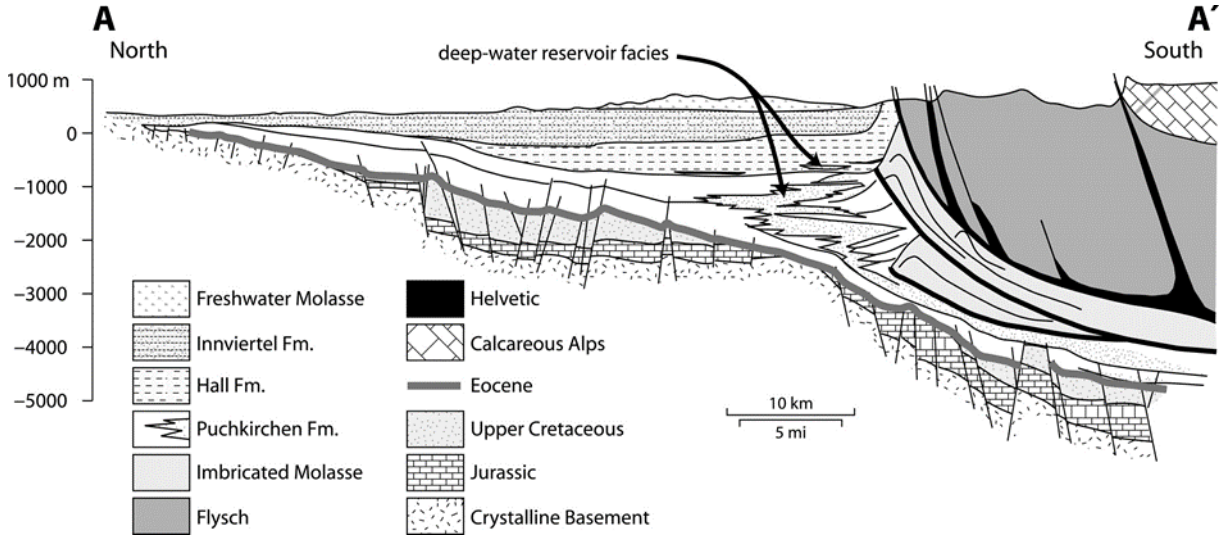

Fig. 2.15 Generalized Cross Section through the Austrian Molasse basin. Cross section A on Fig. 2.14 for geographic location, modified (after Wagner, 1996; by De Ruig & Hubbard, 2006))

2.2.2 Stratigraphy

The Bohemian Massif, being part of the European Craton, forms the crystalline basement of the North Alpine Foreland Basin.

Mesozoic Succession

The Jurassic evolution started with deposition of fluvial and shallow marine sandstones on the Mesozoic shelf of stable Europe. The clastic sediments are overlain by an extensive Upper Jurassic carbonate platform which was uplifted and eroded in early Cretaceous times, see Fig. 2.16. Parts of the karstified carbonate platform are covered by fluvial sandstones, called Schutzfels Formation. These can reach depths up to 100 m beneath the Jurassic surface (Gross et al., 2015).

The Cenomanian succession consists of storm-dominated, shallow marine, glauconitic sandstones, reaching a thickness of 15-70 m. These Cenomanian sandstones form the main oil reservoir of the Trattnach oil field and are divided into three units. CET1 forms the uppermost part and comprises fossil rich calcareous sandstones and conglomerates, which are often cemented. A 1-2 m thick red marker forms the base of CET1, it is interpreted as a mixture of shallow marine sediments, glauconitic matrix, calcareous sandstones, and terrestrial debris flows. The CET1 horizon forms the seal rock, for the reservoir rocks located in CET 2 and CET 3, which form the lower part of the Cenomanian succession. CET 2 and 3 show lithological similarities. In general they comprise greenish, glauconite rich fine-grained sandstone, with some silt and coarser grained sandstone layers in-between. The boundary between CET2 and 3 is a thin layer of well cemented coarse-grained sandstone (Gross et al., 2015).

These Cenomanian sandstones are overlain by upper Cretaceous marls (Wagner, 1998). An erosion event characterizes the Mesozoic – Cenozoic border, where an uplift of the European plate led to extensive erosion of the Mesozoic sediments.

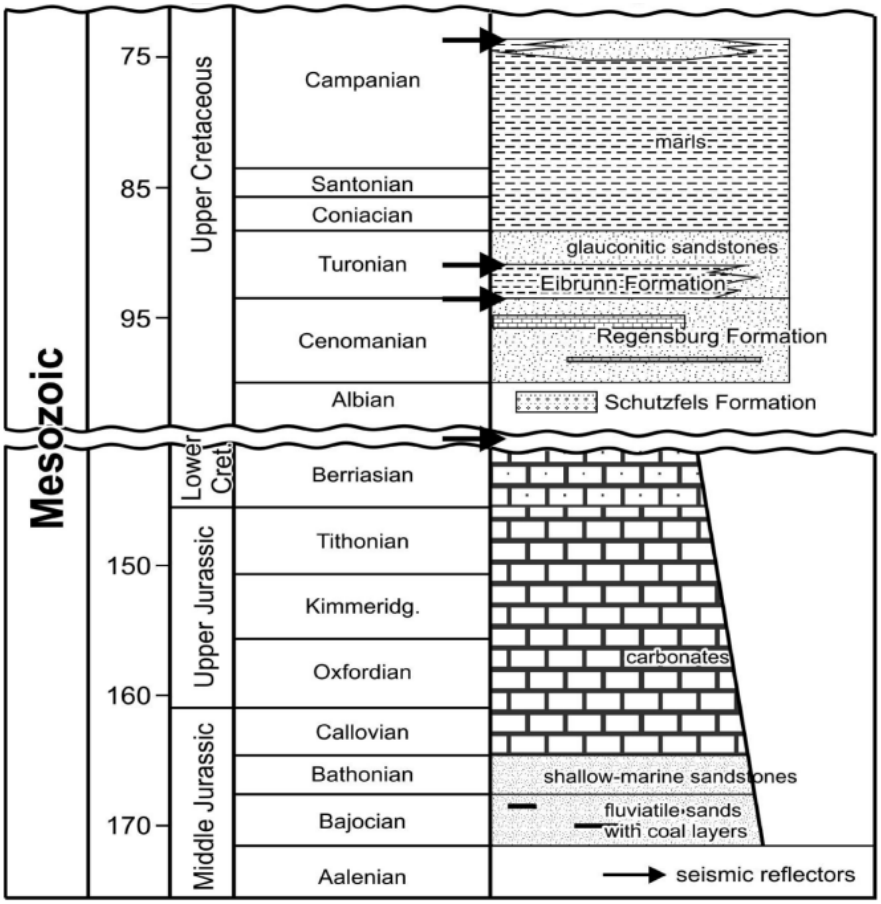

Fig. 2.16 The Mesozoic evolution of the Austrian Molasse Basin (Gross et al., 2015).

Cenozoic Succession

The Cenozoic sediments reach a thickness up to 3000 m in front of the Alps, whereas only a few meters cover the Bohemian Massif in the north (Nachtmann & Wagner, 1987). According to Steininger the molasses sediments can be subdivided into three tectonic units (Steininger et al., 1999). The Autochthonous Molasse includes flat lying sediments in front and underneath the Alps. In contrast, the Allochthonous Molasse consists molasses sediments, which have been incorporated into the Alpine nappe stack. Some molasse sediments rest transgressively on top of various Alpine units and have been transported on their back. They form the Parautochthonous Molasse.

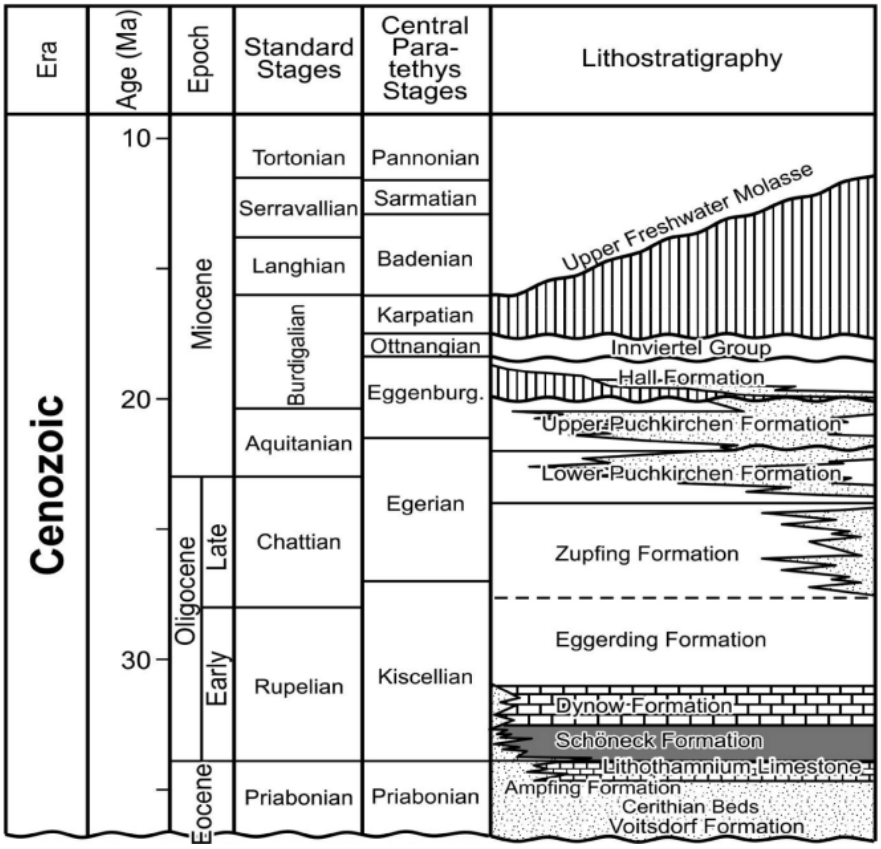

Fig. 2.17 Cenozoic Evolution of the Austrian Molasse Basin (Gross et al., 2015).

The stratigraphic chart in Fig. 2.17 shows the Cenozoic basin fill in more detail, beginning with fluvial and shallow marine sandstones of the Voitsdorf Formation, Cerithian Beds and Ampfing sandstones which grade into shallow marine Lithothamnium Limestones. This Lithothamnium platform drowned in early Oligocene times, due to an abrupt deepening and widening of the basin (Sissingh, 1997). During these deep water conditions, sometimes organic rich, deep-water sediments, divided into Schöneck, Dynow, Eggerding and Zupfing Formation, accumulated in the Molasse Basin (Sachsenhofer et al., 2010). From Mid Oligocene on the debris from the ascending Alps stopped the starved basin conditions and began to slowly fill up the Molasse Basin (De Ruig, 2003). From middle Oligocene times on rivers filled the foreland basin with the Lower Freshwater Molasse and the German and Swiss part of the North Alpine Foreland Basin east of Munich became dry land (Wagner, 1996). In Austria deep marine conditions prevailed until early Miocene, a narrow deep marine trough, the so called Puchkirchen Basin formed the accommodation space for conglomerates, turbidity currents and debris flows derived from the rising Alps (Nachtmann et al., 1987). New insights, based on the correlation of 3D seismic data, indicate that the material derived from west and was transported along the low sinuosity, west-east trending deep water channel (De Ruig et al., 2006).

The ongoing northward movement of the Alps formed the Imbricated Molasse sediments, where parts of the Puchkirchen Formation have been incorporated into the thrust sheets (De Ruig, 2003). A subaqueous erosional interval separates the deep marine Hall Formation from the Puchkirchen Group (Gross et al., 2015). Beginning in Badenian times the sedimentation of the Upper Freshwater Molasse affected the Austrian part of the Molasse Basin. It is composed of coal bearing clays, sands and fluvial gravels, reaching a thickness of several hundred meters (Gusterhuber et al., 2013). Most of this thick succession got eroded after Pannonian times, where up to 800 m sediments have been removed (Gusterhuber et al., 2012).

2.2.3 Petroleum Systems

The Austrian Molasse Basin contains two petroleum systems. One contains thermally generated oil and gas, reaching from Mesozoic to Oligocene times and the second system is of Oligocene to Miocene age, containing biogenetic gas (Wagner, 1998; Gross et al., 2018). The thermogenic petroleum system is charged by Oligocene source rocks, which were deposited during the first isolation of the Paratethys after the Eocene-Oligocene boundary, where starved basin conditions led to the deposition of organic matter rich sediments (Schulz et al., 2002; Sachsenhofer et al., 2010). The Oligocene source rocks comprise, from bottom to top, the Schöneck, Dynow, Eggerding and Zupfing Formations (Fig. 2.17). The Schöneck Formation, formerly Fish shale, consists of organic rich marls and shales and forms with total organic carbon (TOC) contents up to 12 % and hydrogen index values between 500 and 600 mgHC/gTOC the most prominent source rock interval. The overlying organic rich marls and limestones of the Dynow Formation and dark grey laminated pelites forming the lower Eggerding Formation, both play a minor role for oil and gas generation (Gratzer et al., 2011). Important reservoir rocks are the upper Eocene basal sandstones, these contain most of the oil. Minor reservoirs are Cenomanian sandstones, some Oligocene horizons and the Eocene Lithothamnium Limestones. The microbial gas is charged from Oligocene to lower Miocene pelitic rocks and trapped inside the turbiditic and sandy conglomerates of the Puchkirchen Group and the Hall Formation. Oil accumulation in the Trattnach field commenced during Miocene times and is produced from lower Cenomanian green sandstones reservoirs, which are sealed by low permeability Cenomanian rocks and Turonian shales (Gross et al., 2015).

2.3 THE TRATTNACH FIELD

The Trattnach field contains two separate oil fields. The main oil field is located inside the Trattnach mega anticlinale and the second field is located along the Aistersheim fault in the northern part of the Trattnach area and therefore called North Field. Both produce from Cenomanian reservoir rocks.

2.3.1 Production History

The main Trattnach oil field was discovered in 1975, the smaller Trattnach North field in 1983. Both oil fields produced from Cenomanian sandstones, whereas most of the remaining Upper Austrian oil reservoirs produce from Eocene sandstones. These Eocene sandstones are dry in both Trattnach fields. Ten wells were drilled, nine until 1980 and a horizontal well in 2012, with the aim to increase production. Production from Trattnach North Field was abandoned in 1998 and three wells continue production from the Trattnach oil field. TRAT 11 and 12 are drilled into the North Field. Except TRAT 3 all other wells are drilled into the anticlinal dome. The horizontal well drilled in 2012 is an extension of well TRAT 7.

Fig. 2.18 shows the cumulative production history of both Trattnach fields between 1975 and 2015. No recent data is available, because the model was built in 2015. The oil production (blue line) reached its peak in 1978 and declined until 2012. A new horizontal well, drilled in 2012 led to a minor increase in oil production. The gas production (orange line) is strongly varying since the beginning. Water injection started in 1979.

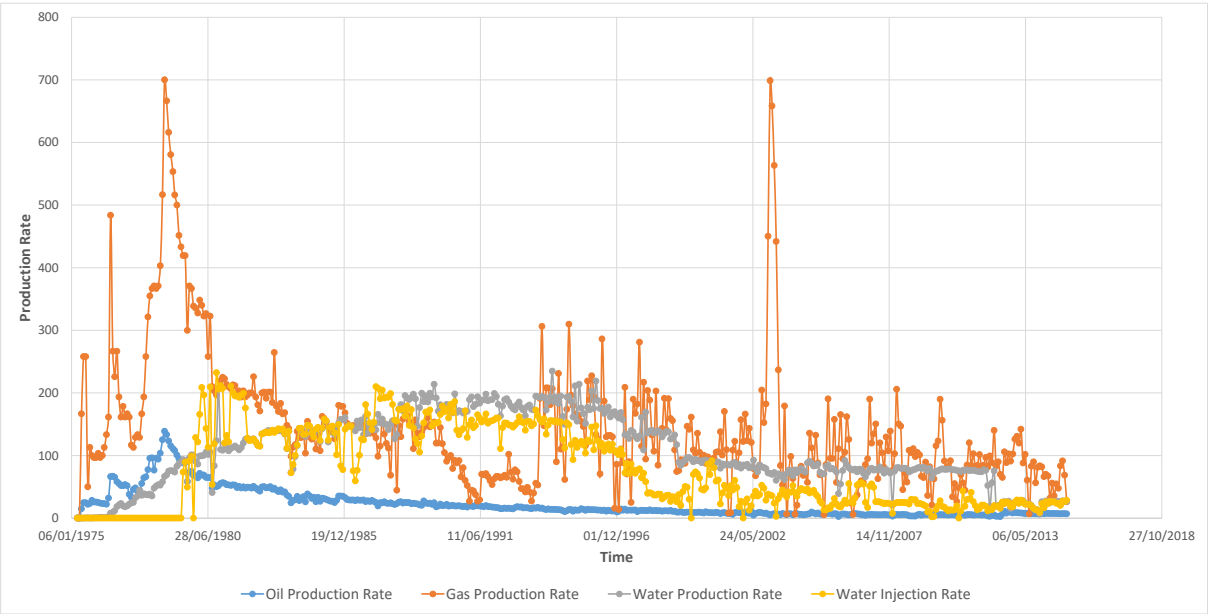

Fig. 2.18 Production History of the Trattnach oil field.

2.3.2 Field Structure and Geology

The faults in the Upper Austrian sector of the Molasse Basin can be separated into a Mesozoic fault system, with roughly N-S trending faults and a Cenozoic fault system (Fig. 2.19). The Cenozoic fault system is characterized by a dense network of E-W trending faults, which are a result of the Alpine nappe loading (Ziegler, 1987).

The Trattnach area is defined by three major faults. Fig. 2.20 shows the Aistersheim fault, forming the northern border of the study area and the Gaspoldshofen fault in the south, both show a west – east trend and belong to the Cenozoic fault system. The third is the north-south trending Schwanenstadt fault, which forms the western border of the reservoir, located in the so called Trattnach mega-anticlinal. It is a dome structure, containing the sealed oil reservoir of the Trattnach field. The lower section of Cenomanian green sandstones (CET2, 3) form the producing reservoir units, whereas the tighter uppermost Cenomanian section (CET1) and overlying Turonian marls form the seal rock. The North Field is located in an anticlinal structure which is sealed by the Aistersheim fault in the north. Its producing reservoir rock and seal rock are from the same lithology as the bigger Trattnach field. Both fields have an initial oil water contact (OWC) of ~1150m TVDS (true vertical depth subsea).

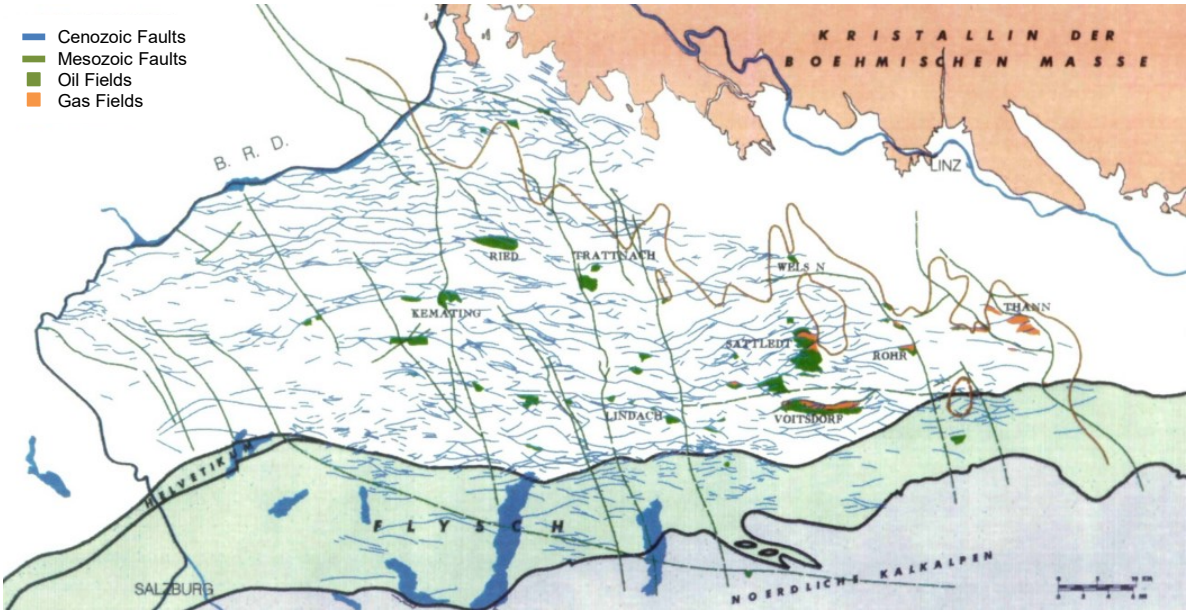

Fig. 2.19 **Fault Systems in Upper Austria.**
Green N-S trending faults are of Mesozoic age, blue W-E trending faults have a Cenozoic age (after Nachtmann, 1995)

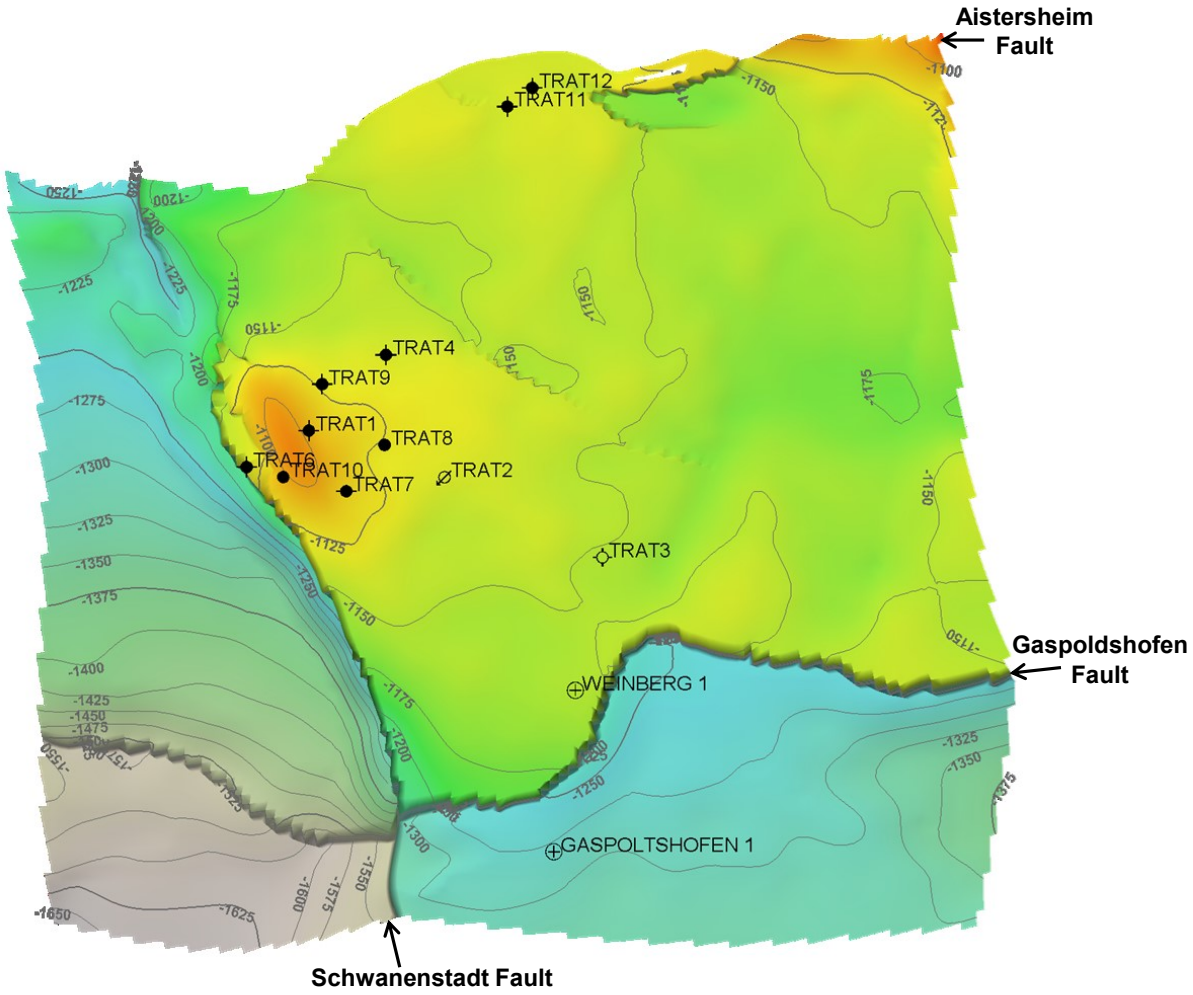

Fig. 2.20 **Depth map of the CET2 horizon.**
The map includes all Trattnach wells, the Weinberg 1 and Gaspoldshofen 1 well. The three major faults are the Schwanenstadt, Aistersheim and Gaspoldshofen faults.

2.3.3 The Trattnach Reservoir

The Trattnach reservoir lies within the Cenomanian sandstones. Based on differences in lithology and its geophysical properties they are divided into three subdivisions.

CET1

CET1 is the uppermost Cenomanian sandstone layer with a thickness between 7 and 12 m. The zone is characterized by varying microlaterolog (MLL) measurements, a generally lower gamma ray (GR) reading than CET2 and CET3, whereas the compressional wave velocity (v_p) is highest in CET1. RAG performed core measurements in the 1970s including porosity, permeability and matrix density. The results are displayed in Fig. 2.21 (porosity data in red, permeability in green and matrix density data in blue). The porosity measurements for the CET1 zone are in a range of 9 to 22 %, with an average porosity of 11 %. The permeability varies between 1.9 and 1200 mD. The matrix density varies between 2.55 and 2.85 g/cm³.

CET2

CET 2 forms the intermediate Cenomanian sandstone layer with a varying thickness of 5 and up to 13 m. Fig. 2.22 shows a very smooth MLL and v_p log. The GR log measurements are unsteady and not very informative. The core measurement show porosity values between 10 and 25 %, with an average porosity of 18 %. The permeability varies between 1.6 and 1100 mD. The matrix density varies between 2.61 and 2.77 g/cm³.

CET3

CET 3 is the lowermost Cenomanian sandstone layer with a minimum thickness of 10 m, reaching up to 16 m. It shows similar log pattern as CET2, reflecting similarities in lithology. The porosity measurements vary between 10 and 28 % with an average porosity of 21 %. The permeability varies between 0.6 and 1900 mD. The matrix density varies between 2.65 and 2.77 g/cm³.

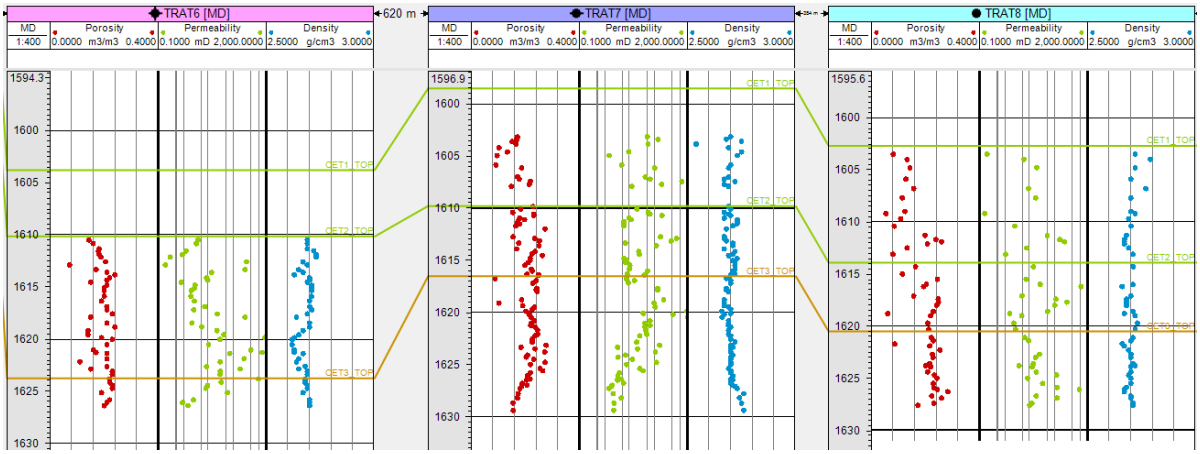

Fig. 2.21 **Core Measurements of the Cenomanian Sandstone.**
Red: porosity data, green: permeability data and blue matrix density. Including the Well Tops Cenomanian_Top corresponding to CET1 Top in pink, CET2_Top in green and CET3_Top and Base in orange.

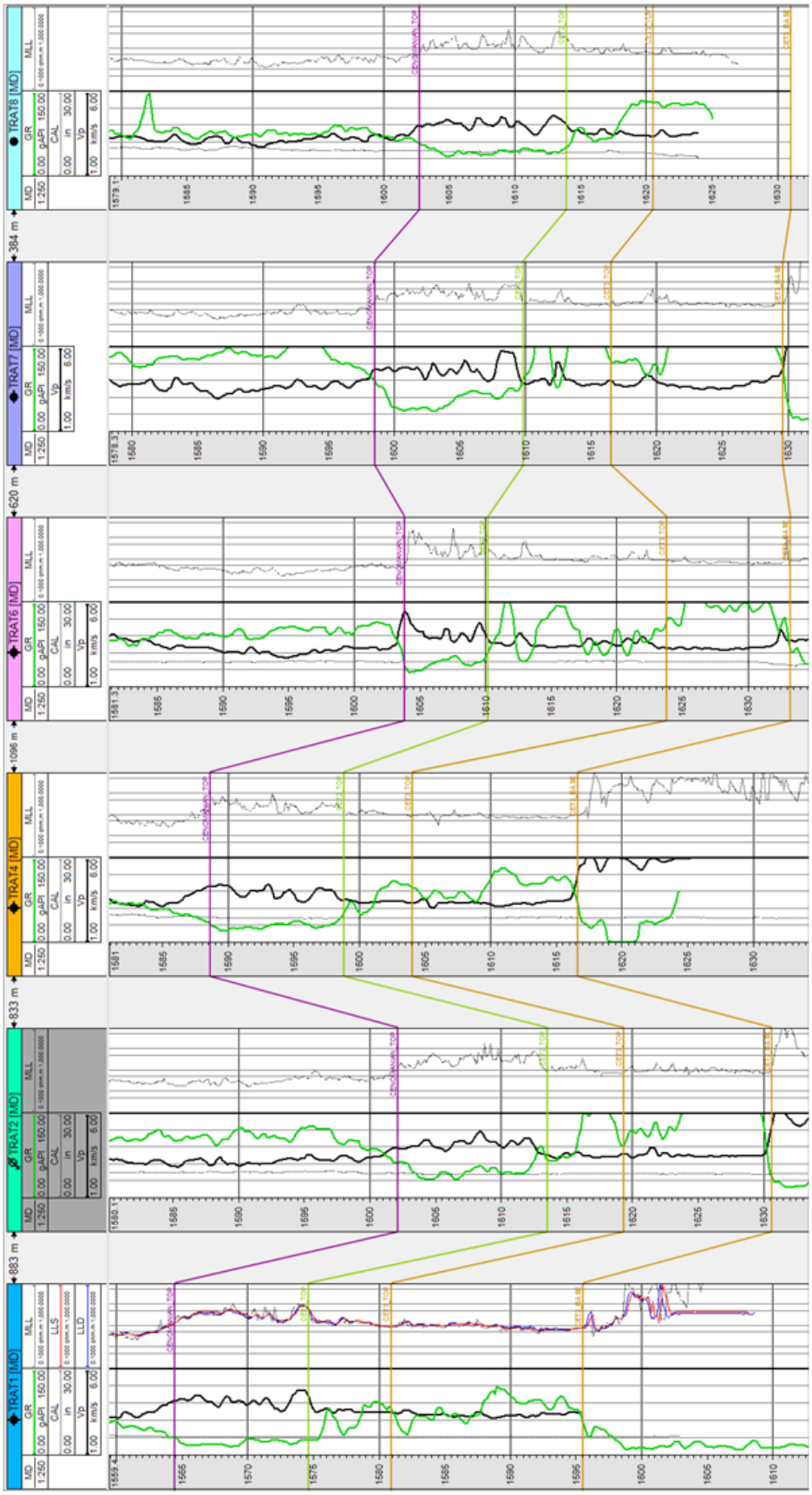

Fig. 2.22 **Well log measurements of the Cenomanian Sandstone.**
The left column shows sonic measurements in black, gamma ray log in green and the black dotted caliper log. Resitivity measurements in the right column. Including the Well Tops Cenomanian_Top corresponding to CET1 Top in pink, CET2_Top in green and CET3_Top and Base in orange.

3 DATASET

Within a university-industry corporation, RAG provided their Trattnach dataset including a 70 km² seismic cube and data of 16 wells including log measurements. To simplify the initial stages of the reservoir model setup, RAG further provided their static geological model, which covers the Cenomanian reservoir. The first step was the collection of information, to get an overview of available data, followed by data organization, with the aim to extract all useful data for a proper model setup. The focus lies on data usable for the calculation of elastic parameters, such as density, porosity and compressional and shear wave velocities. The second part are the faults and interpreted or modelled horizons, those build the basic framework for the geomechanical model setup.

3.1 DATA REVIEW AND ORGANIZATION

3.1.1 Well Data

The well data includes all available wells and their corresponding well measurements, as well as calculated well data. Fifteen wells are available, eleven are drilled into the main Trattnach field, two wells target the Trattnach Nord field and the Weinberg and Gaspoldshofen well cover the area close to the Gaspoldshofen fault.
Existing well measurements cover the most frequent geophysical logs:

- Gamma ray (GR), spontaneous potential (SP) and sonic log (Δt) are available for all wells. The reservoir section has a good data quality, the logs show big gaps beginning from Turonian levels up to the surface.
- Resistivity logs, include Induction, Conduction, Micrologs and Laterologs. Occasionally they cover the entire well track, but mostly confine to the Cenomanian and Eocene part.
- Six wells have a neutron porosity log (NPHI), only the two wells drilled into Trattnach North have a density log (RHOB)

The lack of shear wave logs and the low data density of RHOB logs are compensated by manual calculation, based on petrophysical principals (see chapter 5.2).

One aim is the setup of a proper well section window, for further interpretation and quality control of picked well tops. To accomplish this all logging measurements are categorized,

systematically named and combined. Now the GR track represents all available gamma ray measurements for all wells. This applies for sonic, density, spontaneous potential, neutron and all resistivity logs. Additionally, all well tops are renamed and organized according to the stratigraphic chart seen in Fig. 2.17, all stages and lithostratigraphic formations are located in subfolders corresponding to their age and are labelled accordingly. Mostly the well tops show a higher resolution, than the stratigraphic chart, like the zone of the Innviertel Group, which contains five subgroups.

3.1.2 Core Data

Core measurements were performed by RAG, the data includes porosity, permeability, saturation and matrix density measurements. All results are linked to their corresponding wells. Additionally all coring reports were available, containing all performed core measurements and a detailed core description.

3.1.3 Model Data

The provided reservoir model includes four Petrel models. A geological model built by Montanuniversitaet Leoben (Chair Petroleum Geology), a geological model built by RAG and two Reservoir Models built by RAG.

The static model from RAG covers the Cenomanian sandstones, including four horizons: Top CET1, 2 and 3, as well as Base CET3. The fault model includes 68 faults. The grid contains bulk volume, porosity and permeability data. This model forms the foundation for RAG's reservoir model, but no actual data was used during this study.

RAG's reservoir model is based on their static model, therefore the geographic extent and number of horizons are equal. The fault model contains just 16 faults, the difference of the fault models can be seen in Fig. 3.1, with the bigger fault model on the left-hand side and the simplified fault model on the right-hand side.

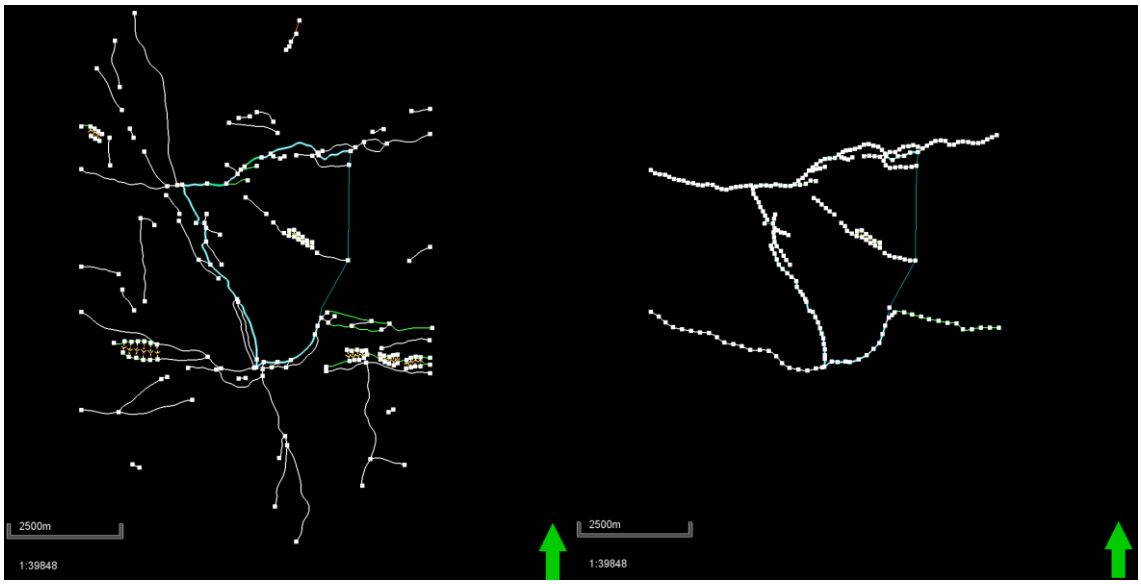

Fig. 3.1 Differences of RAG's fault models.
The left fault model includes 68 faults and the right fault model includes 16 faults.

The reservoir grid is populated with porosity, permeability, water and residual oil saturation. Further properties are simulation results like recoverable oil, gas saturation and pressure data. This model serves as main input data for this study. The 16 faults and modelled Cenomanian horizons were copied and built the foundation for the geomechanical model setup.

The model created by students and employees of Leoben also covers the Cenomanian succession, including three horizons and 10 faults. It includes oil, gas and water saturation from 1975 until 2010, but no pressure data. Although not included in the model, they interpreted additional horizons. The shallower Base Hall and Base Eocene horizon and the deeper JUBSS (Upper Jurassic Base Sandstone) horizon. These interpreted horizons are used as model input for the study, the rest of the model is not used for the geomechanical model setup.

3.1.4 Additional Data

- Completion logs from nine wells, showing the log measurements, lithologies, position of coring and open hole test results,
- Drilling reports and drilling fluid reports,
- Oil and gas analyses,
- Petroleum reports, including open hole test results,
- Post completion reports

4 RESERVOIR MODEL SETUP

RAG's reservoir model covers the Cenomanian succession, including the produced reservoir units, formed by the green sandstones (CET3, CET2) and the low permeable seal rock (CET1). For time saving reasons the picked faults as well as the horizons CET1 Top, CET2 Top, CET3 Top and Base are copied from RAG's reservoir model, by doing this the history match performed by the reservoir engineer can be used as well. The main object during the model extension is to keep all changes in the reservoir area as small as possible, so that the history match of the reservoir simulation, still fits for the new model.

When performing a geomechanical study the whole section from the earth's surface down to the crystalline basement is of interest. Therefore, the model extension up to the earth's surface is inevitable. Furthermore the horizontal extent of the model is increased and covers now an area of approximately 25 km², the exact location of the entire study area and all available drilled logs are shown in Fig. 4.1.

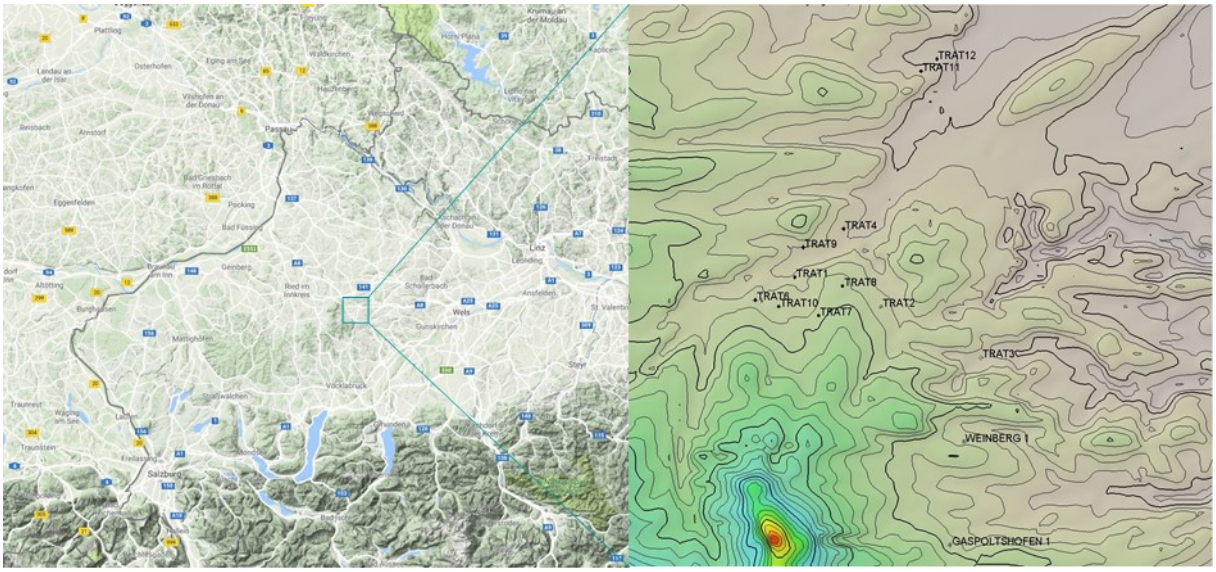

Fig. 4.1 Study area of the Trattnach Oil Field.
(a) Map of Salzburg and Upper Austria, shows the location of the Trattnach oil field
(b) Detailed view of the study area, with an geographic extent of 6 km²; Location of wells.

4.1 GRID

The first task involves a fault model extension up to 500 m above sea-level, although the base Hall surface marks the end of active faults. However because Petrel cannot stop faults at certain horizons, the faults of a geomechanical model must cover the entire model depth. The 16 faults from RAG's simulation model are copied into a new model and mark the beginning of the modeling process. Those faults start at -700 m, about the beginning of Rupelian section and end at -1900 m, this is sufficiently deep because the faults go deeper than the lowermost interpreted horizon JUBSS. The extension keeps the original course of each fault, but the shallower parts need manual editing and a new alignment, due to an extension of up to 800 m pre-existing fault orientation leed to fault crossovers in shallow areas. The new fault model seeks a perfect match of the interpreted faults in the lower sections, whereas the upper parts are kept as smooth as possible. The conversion of listric to curved faults, especially in close proximity to reservoir areas, yield very good results. Faults close to the border, remain listric faults, to keep the fault model simple. The new fault model defines the new model boundary for the pillar gridding process.

The first run results in a bad grid, with two distinctive weak spots. Normally Petrel has no problem when gridding y faults, but due to the extension up to the earth's surface the grid buckling is so severe, that an exclusion of the fault rendered to be the best solution. A sufficiently large distance to the reservoir and a secondary role concerning the fault model justifies this simplification. The second modification is the extension of the Schwanenstadt fault in the southern part of the Gaspoldshofen fault. Examination of seismic sections verified the fault extension in that direction. After these minor modifications and an insertion of several trends the pillar gridding process results in a sufficiently uniform grid.

4.2 HORIZONS AND ZONES

Some input surfaces for the "make horizons" process are in time domain, this requires a depth conversion based on a velocity model. The setup of an advanced velocity model leads to a model through evaluation of characteristic interval velocities (v_{int}) or a time depth relationship for each zone of interest. A depth conversion is applied to three surfaces:

- Base Hall is converted with a linear time depth relationship $v = v_0 – 0.66 *z$
- Top Eocene is converted with a linear time depth relationship $v = v_0 – 0.90*z$
- JUBSS is converted using the interval velocity $v = v_0 = v_{int}$

With v_0 being the velocity, in m/s, at the top of each zone and z the depth in meters. Subsequently all input surfaces are available in depth domain. Including the four Cenomanian surfaces and earth surface, a total of eight surfaces are interpolated along the new grid boundary defined by the fault model. As a result, all input surfaces have the same area of approximately 25 km².

4.2.1 Horizon modeling

Conversion of these surfaces into horizons, maintains the original structure and location, but links them to the grid and its comprising faults. Linking faults and horizons allows the determination of fault cut back, this is a manipulation of offset distances or how much drag is allowed for a certain fault. The surface to horizon conversion involves multiple horizon cross-overs in areas of low data density, especially for the Cenomanian horizons which are separated by very little distances. In a second run a step by step approach resultes in a very good horizon model. Beginning with the creation of the CET1_Top horizon and stacking of the CET1 thickness maps beneath, marking the technical start of the CET2 horizon. By doing this, the horizon fault lines at the base of zone CET1, which fit perfectly to those of CET2_Top, can be stored and used as an additional input for the second run of CET2_Top horizon creation. All Cenomanian horizons are created by using this method. Due to the lack of convenient well tops for the JUBSS horizon, a thickness map creation is not possible and consequently stacking is no option for the lower model part. The vertical distance between JUBSS and CET3_Base is sufficiently large, so there are no horizon crossovers present. Fig. 4.2 (b) shows that the NW-SE trending faults stop at the Base Eocene horizon, so stacking Top Eocene succession on top of the CET1 horizon cannot be performed. Both Cenozoic horizons, Top_Eocene and Base_Hall are created via the conventional workflow. Summarizing, the Mesozoic horizons are characterized by two different faulting regimes, one in NW-SE direction and a second in E-W direction. The Eocene Horizon is displaced by E-W oriented faults, whereas the Base_Hall and Surface horizons have no active faults (Fig. 4.2).

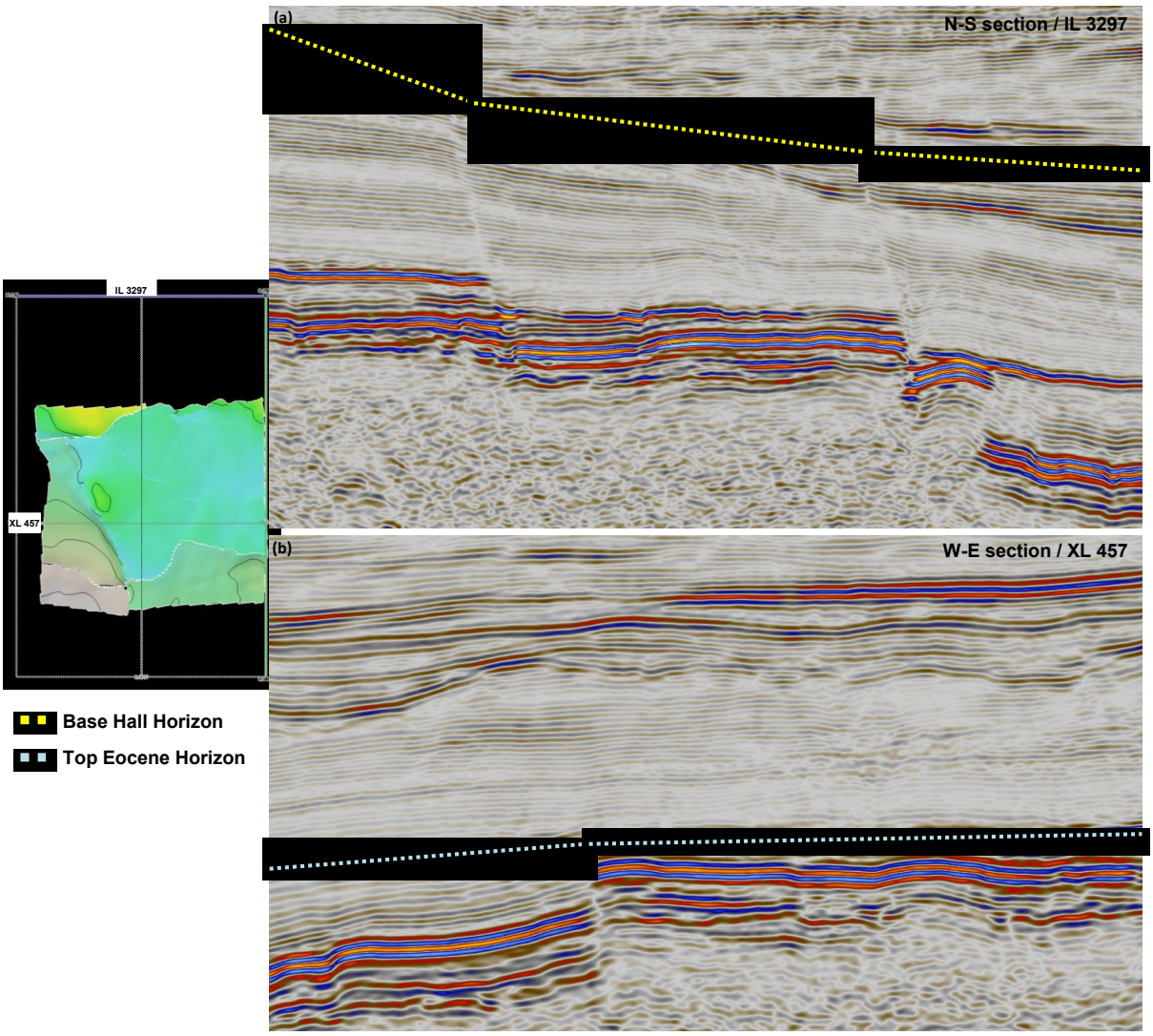

Fig. 4.2 **Seismic Sections of the study area.**
(a) N-S Profile, about 10 km long; dotted line indicates the termination of E-W oriented faults at base Hall Formation;
(b) E-W Profile, approximately 7 km long; dotted line indicates end of N-S (NE-SE) oriented faults at Base Eocene

4.2.2 Zonation

The faults and horizons form the basic framework. The next steps are the zonation and layering of the model, with the premise of representing the stratigraphic successions of the basin. The zonation concept, seen in Fig. 4.3, is based on the stratigraphic chart (from Gross et al., 2015). The JUBSS horizon forms the base of the model, an absence of significant well tops within the Jurassic carbonate succession makes a further zonation impossible. The overlying Cenomanian succession is represented by four horizons making a further detailed zonation unnecessary. The space between CET1_Top and Eocene_Top represents from base to top, the Turonian Zone, comprising marls and sandstone, followed by the marly Coniacian zone and the Eocene sandstones on top. The thick succession between Top_Eocene and Base_Hall is divided into

the Fish shale or Schöneck Formation, on top of the Eocene, followed by the Rupelian zone, including the source rocks of the Dynow and Eggerding. Further on top is the Puchkirchen Group, which is separated into a Lower and Upper Puchkirchen Formation. The uppermost interval consists of the Hall Formation at the base and the Innviertel Group on top. The top is formed by the earth's surface, an erosional horizon. The combination of horizons and zones represents the lithostratigraphy of the basin.

4.3 LAYERING

The last step of the setup of the static reservoir model is layering, where a characteristic pattern, representing the prevailing sequence stratigraphic type, is assigned to each zone, or horizon interval. There are four different styles of layering available: proportional, follow top or base and fractions. Due to restrictions for the Cenomanian interval, to keep the changes as minimal as possible, the layering is an identical adaption of RAG's reservoir layering. Zone CET_1 has a fractioning of 1-1-1, resulting in a zone trisection with equally big grid cells, zone CET_2 shows an asymmetric trisection of 1-2-2, with a smaller upper layer and two bigger bottom layers and CET_3 is divided into two thinner upper layers and one thicker bottom layers 1-1-2. This layering fits the lithostratigraphy perfectly. CET1 comprises of calcareous sandstones and conglomerates with an up to 2 m thick red marker bed at the bottom. CET2 and CET3 are lithologically relatively similar, consisting of glauconite rich fine-grained sandstone, some silt layers and medium grained sandstone. The boundary between CET2 and CET3 is formed by a thin well cemented coarse-grained sandstone, showing high resistivity and low DT readings. According to the seismic section presented in Fig. 4.3 the layering of the Innviertel Zone is proportional, the layering of the Hall Formation follows the top horizon with onlaps on the base, the same applies for the Upper Puchkirchen Formation. The lower Puchkirchen Formation has toplaps, accordingly a follow base layering was chosen. The remaining JUBSS, Turon, Coniacian, Rupelian and Eocene zones have a proportional layering.

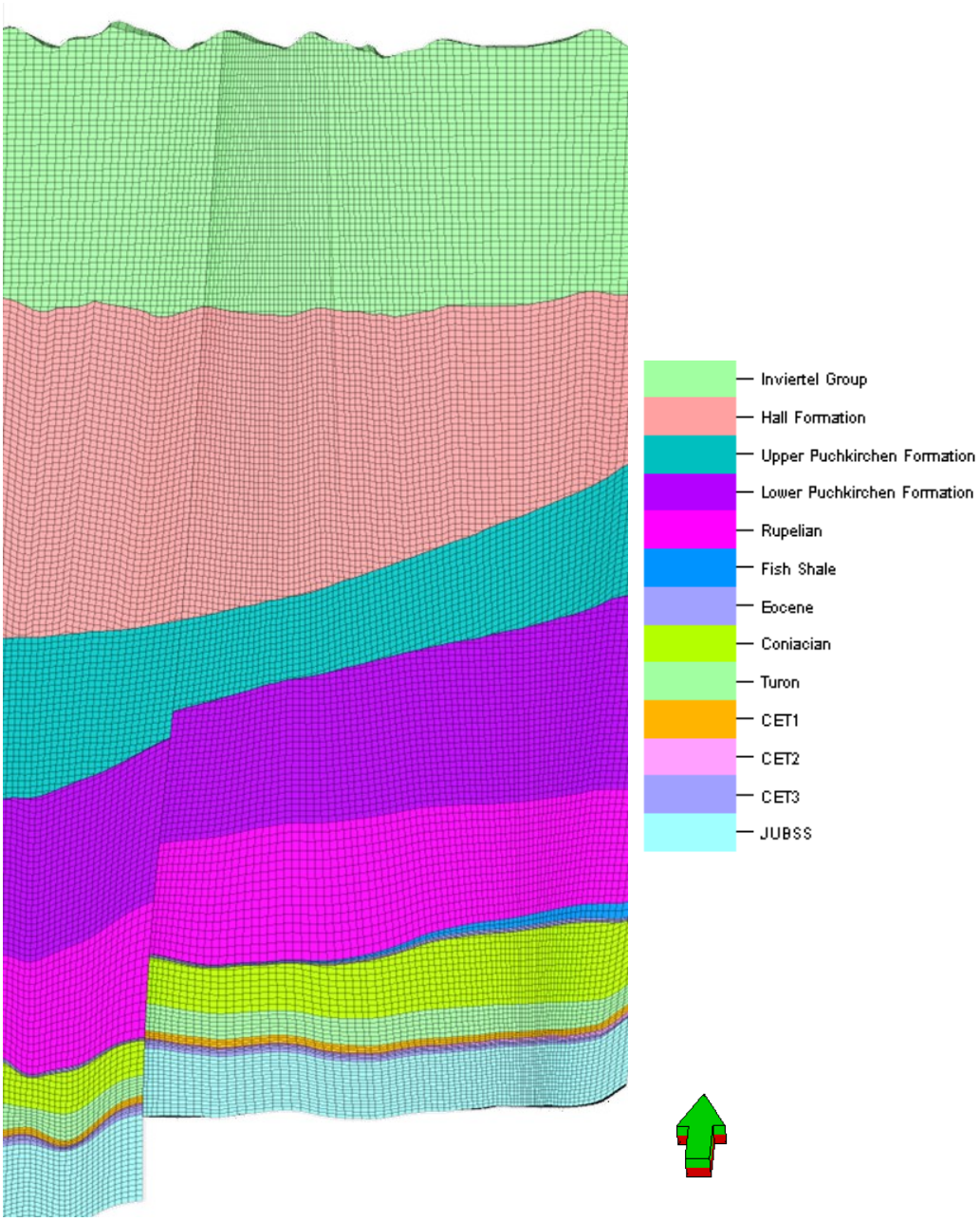

Fig. 4.3 **Grid Slice, final zonation and layering.**
The zones show the most prominent stratigraphic sections according to Fig. 2.16 and 2.18. The layering reflects seismic patterns of each zone.

5 GEOMECHANICAL MODEL

5.1 CREATING A GEOMECHANICAL GRID

The main function of geomechanical gridding is the embedding of the reservoir model with side-, over- and underburden grid cells to enable a smooth geomechanical simulation.

5.1.1 Settings

Depending on the vertical and horizontal extent of the reservoir model several considerations must be taken into account. Most important is a model aspect ratio of 3:1, which implies 1 km depth for every 3 km of horizontal extent (Schlumberger, 2015). Adjustment to fulfil this requirement is done through sideburden and underburden settings. Mostly because the underburden has no depth limits, all additional unrealistic underburden is considered as stiff bedrock. In contrast the overburden is limited by the earth's surface which forms the uppermost boundary. Depending on the reservoir model extent, two embedding methods are available:

1 Models which already reach earth's surface need no additional overburden and the embedding process is reduced to side- and underburden modeling. An advantage of this embedding process is the possibility to make a more realistic replication of the present basin geology. A possible disadvantage is that these models can have a complex grid and need a further simplification in some areas to fulfil the requirements of a geomechanical grid. The model described in chapter 2.2 is such a model and the simplification and editing process is described in chapter 5.1.2.

2 Models which cover just the most important parts of the reservoir model, like the reservoir section and adjacent zones. These models can then be embedded with an over-, under- and sideburden.

Sideburden

When building a sideburden, the number of grid cells and the way the sideburden cells should be created must be chosen. Two options are available, either the cells are created by *extend by*, for example 1000 m to the left and right hand side of the reservoir model or by *multiply by*, for example the sideburden should be 3 times the reservoir grid on both sides (Schlumberger, 2015).

For this study, the geomechanic grid sideburden is created by multiplication with 0.5, including 5 grid divisions with a geometric factor of 1.5.

$$1: f: f^2: \ldots . f^{n-1} \quad \textbf{Eq. 19}$$

The geometric factor defines how the grid cells become larger with increasing distance from the reservoir grid (see Eq. 19). The n stands for the number of sideburden cells which are created. Another option would be proportional, where all grid cells have the same size (Schlumberger, 2015).

Overburden

Generating overburden cells can be done through *extend by* and *multiply by*. The third option is *extend to*, where a specific depth can be entered, for example -200 m, and the number of cells dividing these additional 200 m must be defined. Furthermore the map horizon control option can be chosen (Schlumberger, 2015). Using the map horizon control option, a specific input surface, like Eocene_Top or Base_Hall surfaces can be inserted, these act as guide horizons during the overburden generation. When using the map horizon control, a number of cells between each horizon must be defined.
The geomechanic grid in this study has no overburden, because the original grid extends up to the earth's surface.

Underburden

Underburden cells are created like overburden cells, with the difference that there is no depth limit (Schlumberger, 2015). For this geomechanic grid two additional underburden horizons are created. One at a depth of -2500 m and a second at -5000 m, both have 5 divisions and proportional grid spacing. The depth of -5000 m was sufficiently large to maintain the aspect ratio of 3:1.

5.1.2 Gridding

The first gridding process resulted in a geomechanic grid including more than 30000 bad cells (see below in Fig. 5.1). The aim was to keep all changes as small as possible to get a result which is as close as possible to the grid built by RAG. The amount of bad cells shows that a geomechanical grid requires a simpler grid cell geometry. All grid cells must have a convex geometry and volumes greater or equal to zero, otherwise they are considered as bad cells. As seen in Fig. 5.1 the bad cells concentrate along the lower section of the northernmost fault and

the upper parts of the sideburden. The elimination of these bad cells includes editing of faults, zones and a simplification of the fault model in some areas.

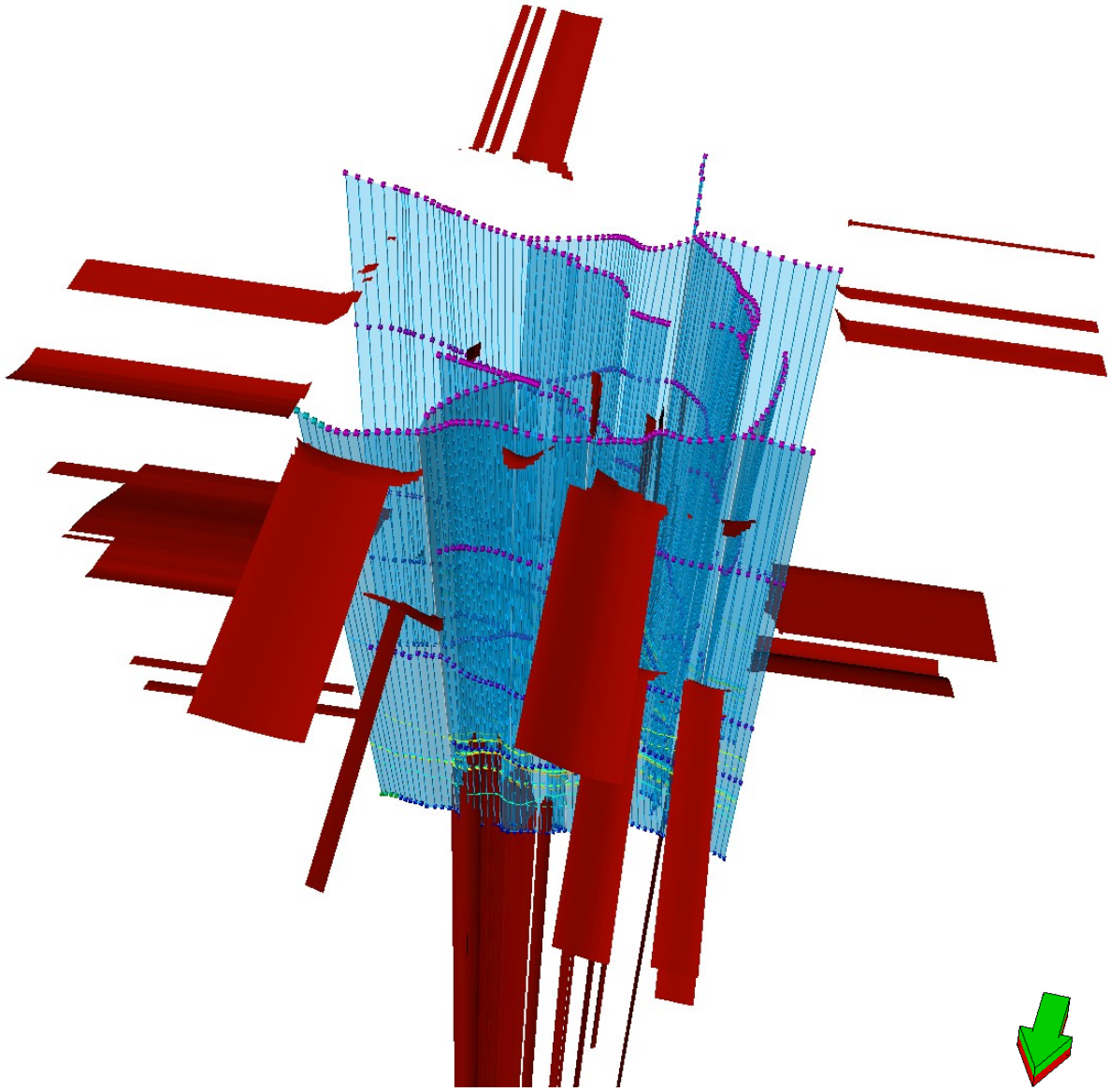

Fig. 5.1 **Quality Control of the geomechanical gridding process.**
All bad cells filtered by cell volume equal or below zero are highlighted in red. Also visible is the original fault model.

Editing of the fault model

The simplification of the fault model involves the elimination of three faults. Faults number 2 and 64 are two small faults far away from the reservoir section (Fig. 5.2). Assuming a minor importance concerning the reservoir model, those two are neglected. The same applies for fault number 31, a branch from fault number 30. Comparing the two fault models it can be seen than all faults are much smoother and the fault pillars are almost at equal distance. Extending the two main faults in the south beyond the gridding boundary leads to a smoother grid and eliminates the bad cells in the south. Fault number 1 forms now the northern grid boundary,

combined with a general smoothing of fault pillars and geometry, all bad cells along that fault are removed.

Fig. 5.2 **2D View of fault models.**
Left: original fault model; right: edited fault model to fulfil the requirements of the geomechanical gridding process.

Some editing applies to all faults, like additional pillars at fault junctions and at curvy sections, minimizing the distances leads to smaller and more orthogonal grid cells.
Trends assigned to faults help to align the grid cells along faults. The geomechanic grid cannot cope with small gaps between similar trends, therefore the trends are either deleted of combined to minimize the number of bad cells.
After the editing process, all faults are steeper and less convex, especially in the area close to the surface. The fault model is a structure of individual faults, which are defined by their pillars. Five different pillar types can be chosen to define the geometry. Using different kinds of pillar types along one fault generates bad cells. During the editing of the fault model the pillars are unified, so that the faults have either a listric or a curved pillar type. Listric pillars have three shape points and curved pillar types consist of five shape points, where all points can be edited separately.

Editing of zones and layering

All bad cells located in the sideburden can be removed with three modifications. The first modification is the merging of the Turonian and Coniacian zone, because the Coniacian zone pinches out in southwestern direction (Fig. 5.3). The zero thickness of the zones produced a big set of bad cells around that area, now the Turonian and Coniacian form one zone, neglecting

the Turonian sandstone at the border to the Coniacian, for further calculations the whole zone is considered as marl.

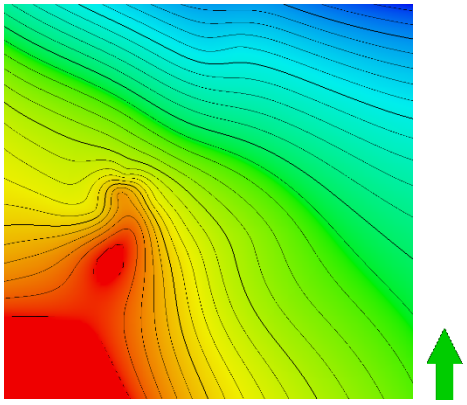

Fig. 5.3 Thickness map Coniacian.

The second modification involves the change of layering, as seen and described in chapter 4.3, the layering of the Innviertel Group is “follow surface”, Hall Formation and Upper Puchkirchen Formation have a “follow top” layering and the Lower Puchkirchen Formation “follow base”. All of these layering options lead to onlaps or offlaps on the border to the adjacent zone. Reservoir Geomechanics does not support that kind of layering, because the resulting grid cells do not fulfil the requirements of volume greater than zero and convex geometry. Therefore the layering of those four zones is changed to a proportion layering. The last modification is the adjustment of the gridding boundary, resulting in more orthogonal grid cells.

Fig. 5.4 and Fig. 5.5 show the final geomechanic grid including the detailed reservoir grid at the centre and the embedded area, formed by side- and underburden. The original grid has a horizontal extent of approximately 6 x 6 km and it is extended by 3 km of sideburden in each direction. The vertical extent of the model (see yellow section in Fig. 5.5) reaches up to 680 m above sea level and ends at the JUBSS horizon at a maximum depth of -1800m. The underburden starts at the JUBSS horizon and ends at a depth of -5000 m. The geomechanic grid has no overburden, because the original grid extends up to the earth’s surface. It can be seen that the grid cell size increases with distance to the original grid, this reduces the needed computer power for further simulations.

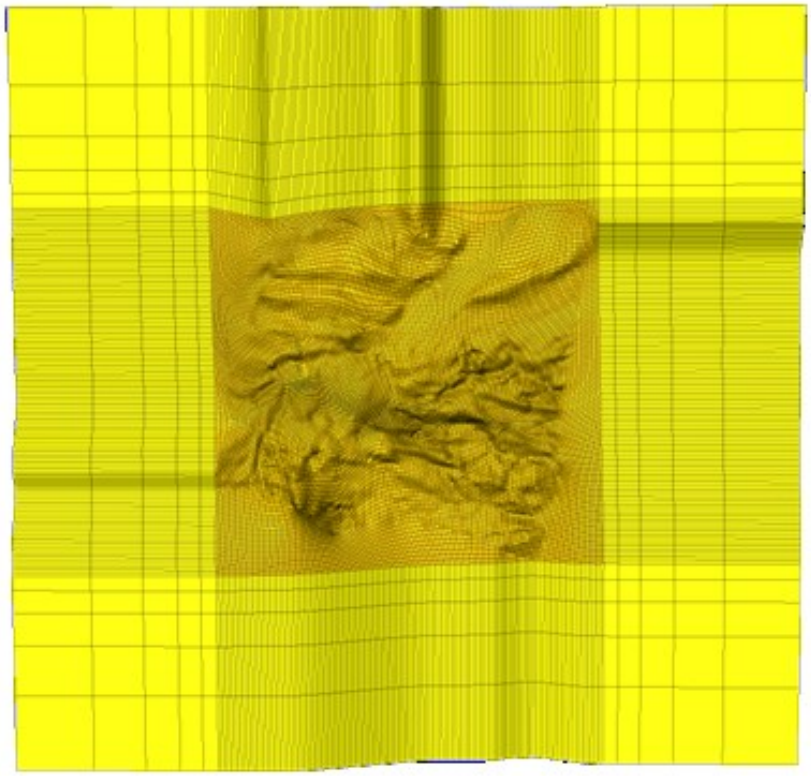

Fig. 5.4 **Topview of the geomechanical grid.**
The orange section in the middle is the original model, which is embedded by the yellow sideburden

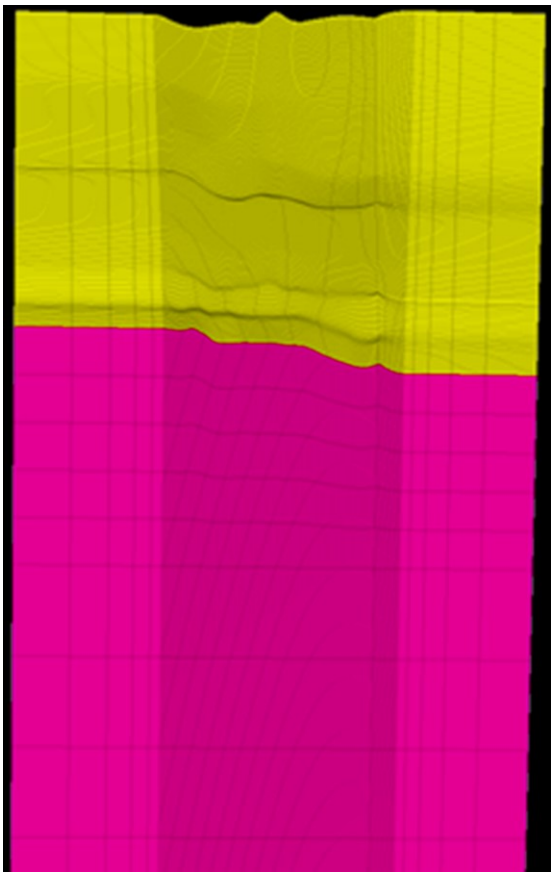

Fig. 5.5 **Side view of the geomechanical grid.**
The yellow section on the top is the original grid, below is the pink underburden

5.2 PROPERTY MODELING

The geomechanical gridding process is followed by material modeling. During this process one can either choose materials from the material library included in the software or define characteristic materials based on the basin´s lithology and its different elastic moduli and strength properties. Calculating the elastic properties requires density, porosity and velocity information for all available lithologies or zones. The dataset included density logs for two wells and no shear sonic logs. Porosity data is available for the reservoir sections including NPHI logs and core measurements. Therefore a property modeling of all missing data is performed, to allow the calculation of elastic properties and the setup of rock specific materials for the entire extent of the model.

The property modeling includes calculation of density data based on Gardner's equation (Gardner et al., 1974), the computation of porosity logs with Wyllie's time average equation (Wyllie et al., 1956) and the calculation of shear sonic logs using Castagna's and Han's empirical $v_p - v_s$ relationships (Castagna et al., 1985; Castagna, 1993; Han et al., 1986).

5.2.1 Density Data

The fact that the elastic modulus of a rock is calculated by multiplying the velocity and density, makes density logs inevitable for the calculation of elastic moduli. Unfortunately, only the TRAT 11 and TRAT 12 wells have density logs and even those do not cover the entire drilled depth.

The missing density logs were calculated through Gardner´s empirical relationship published in 1974 (Gardner et al., 1974).

$$\rho = a * v_p^b \qquad \text{Eq. 20}$$

A zone log, which represents the final zonation during the pillar gridding process (Fig. 4.3) is created and the velocity and density data for each zone extracted. To gain the linear v_p-RHOB function, the extracted v_p and RHOB data is plotted for each zone separately. Data for the Hall and Upper Puchkirchen Formation is taken from well TRAT 11, plotted in Fig. 5.6, all other available data is taken from well TRAT 12 (see Fig. 5.7). Before plotting the velocities versus densities, a log conditioning was performed. It included removal of spikes and smoothing of certain areas with inconsistent data. These smoother density and velocity logs are used to determine the linear relationship.

The empirical constants a and b are delogarithmized for each zone (see Table 5.1 for results). Knowing a and b, the density logs for all other wells are calculated using Gardner´s equation.

Due to gaps in the density logs the construction of an empirical relationship was not possible for the Innviertel Group, Lower Puchkirchen Formation and the Rupelian. Based on similarities in lithology the following assumptions have been made: Innviertel Group is comparable to Hall Formation, therefore the empirical relationship of the Hall Formation is applied for the Innviertel Group. The Upper Puchkirchen Formation is a good fit for the Lower Puchkirchen Formation and the Eocene function is applied to calculate the density of the Rupelian.

Equation	Linear Relationship	a	b
Hall Formation	log(Y) = 0.170032 * log(X) - 0.218061	2.02	0.14
Upper Puchkirchen	log(Y) = 0.27461 * log(X) - 0.572581	1.78	0.27
Fish Shale	log(Y) = 0.123935 * log(X) + 0.326994	2.12	0.12
Eocene	log(Y) = 0.409155 * log(X) + 0.135206	1.37	0.41
Coniacian	log(Y) = 0.0919171 * log(X) + 0.356692	2.27	0.09
Turon	log(Y) = 0.257638 * log(X) + 0.267475	1.85	0.26
CET1	log(Y) = 0.0997267 * log(X) + 0.347347	2.23	0.10
CET2	log(Y) = 0.440732 * log(X) + 0.134828	1.36	0.44
CET3	log(Y) = 0.198046 * log(X) + 0.272713	1.87	0.20
JUBSS	log(Y) = 0.661397 * log(X) - 0.0201822	0.63	0.66

Table 5.1 Gardner's empirical v_p – density Relationship.

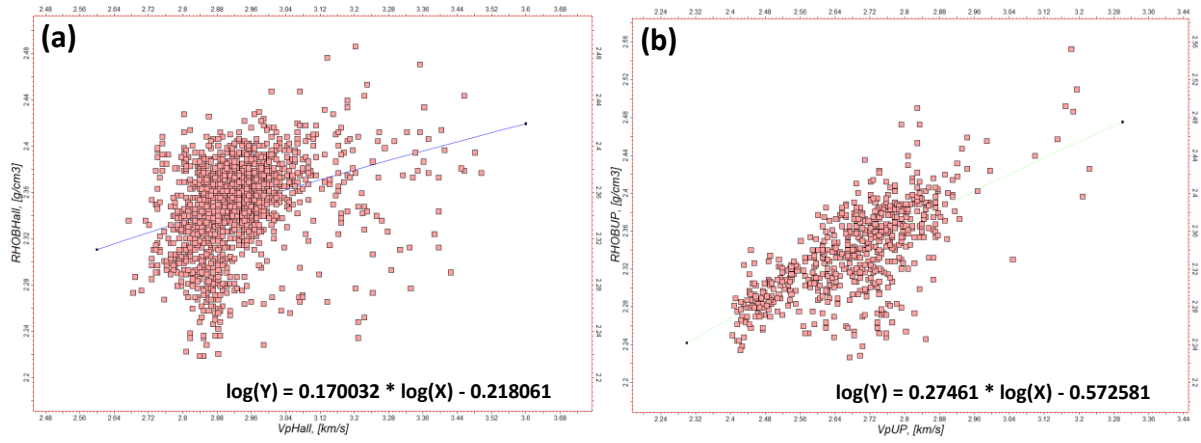

Fig. 5.6 Empirical Relationship between v_p and RHOB from TRAT11.
Linear relationship and function for the (a) Hall Formation and the (b) Upper Puchkirchen Formation

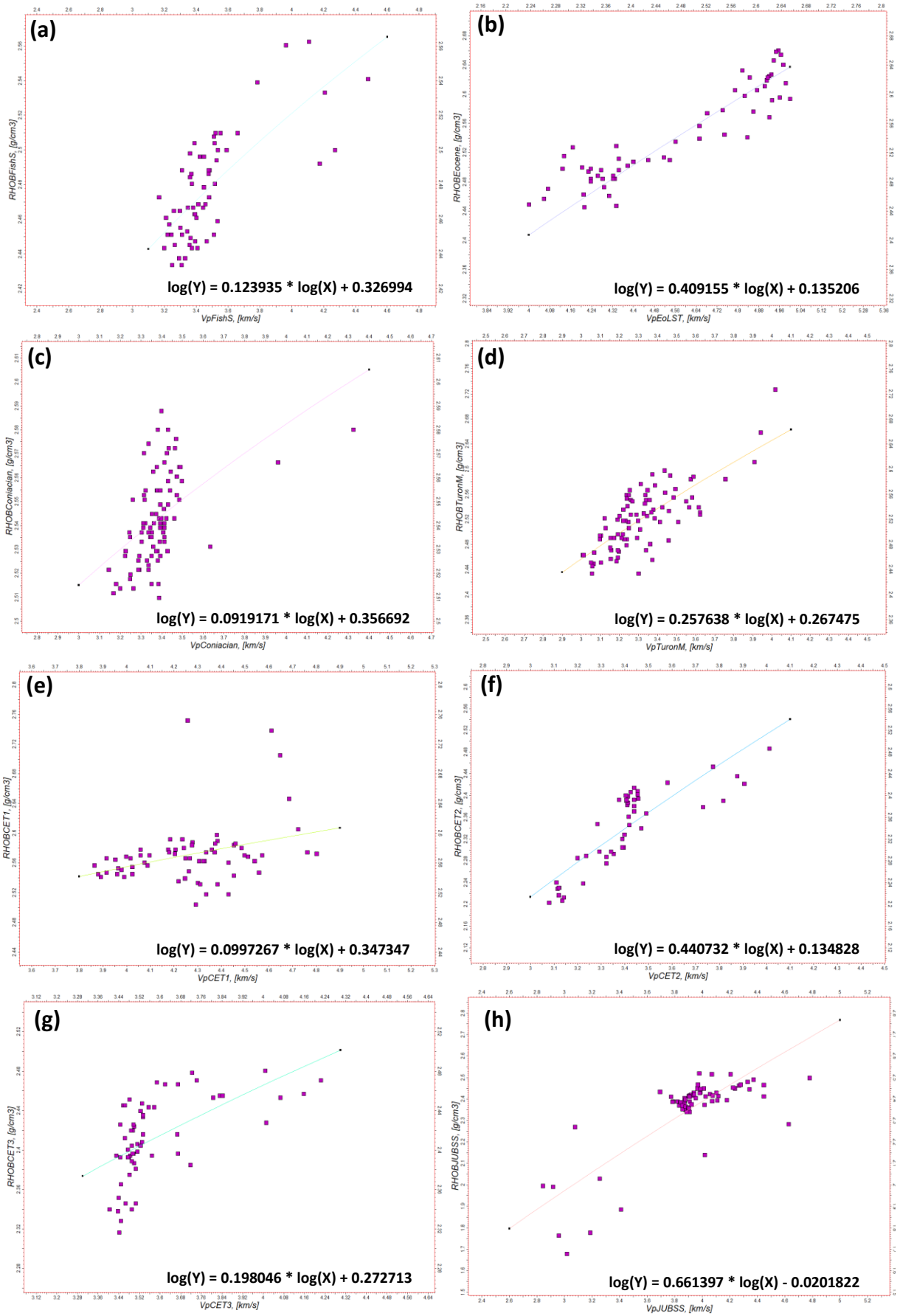

Fig. 5.7 **Empirical Relationship between v_p and RHOB from TRAT12. Linear relationship and function for the (a) Fish shale, (b) Eocene, (c) Coniacian, (d) Turonian, (e) CET1, (f) CET2, (g) CET3 and (h) JUBSS**

Gardner's equation, Eq. 20, is applied to each zone for all wells. The calculated density logs are shown in Fig. 5.8 and the equation for each zone is shown in appendix 10.1 "Density Calculation". The gaps in TRAT2, 3 and 4 are a result of missing sonic velocity measurements, because without velocity information Gardner's relationship cannot be applied. Nevertheless all other wells have continuous sonic logs and allow the calculation of density for the Upper and Lower Puchkirchen Formations, which is later interpolated over the area of TRAT2, TRAT3 and TRAT4.

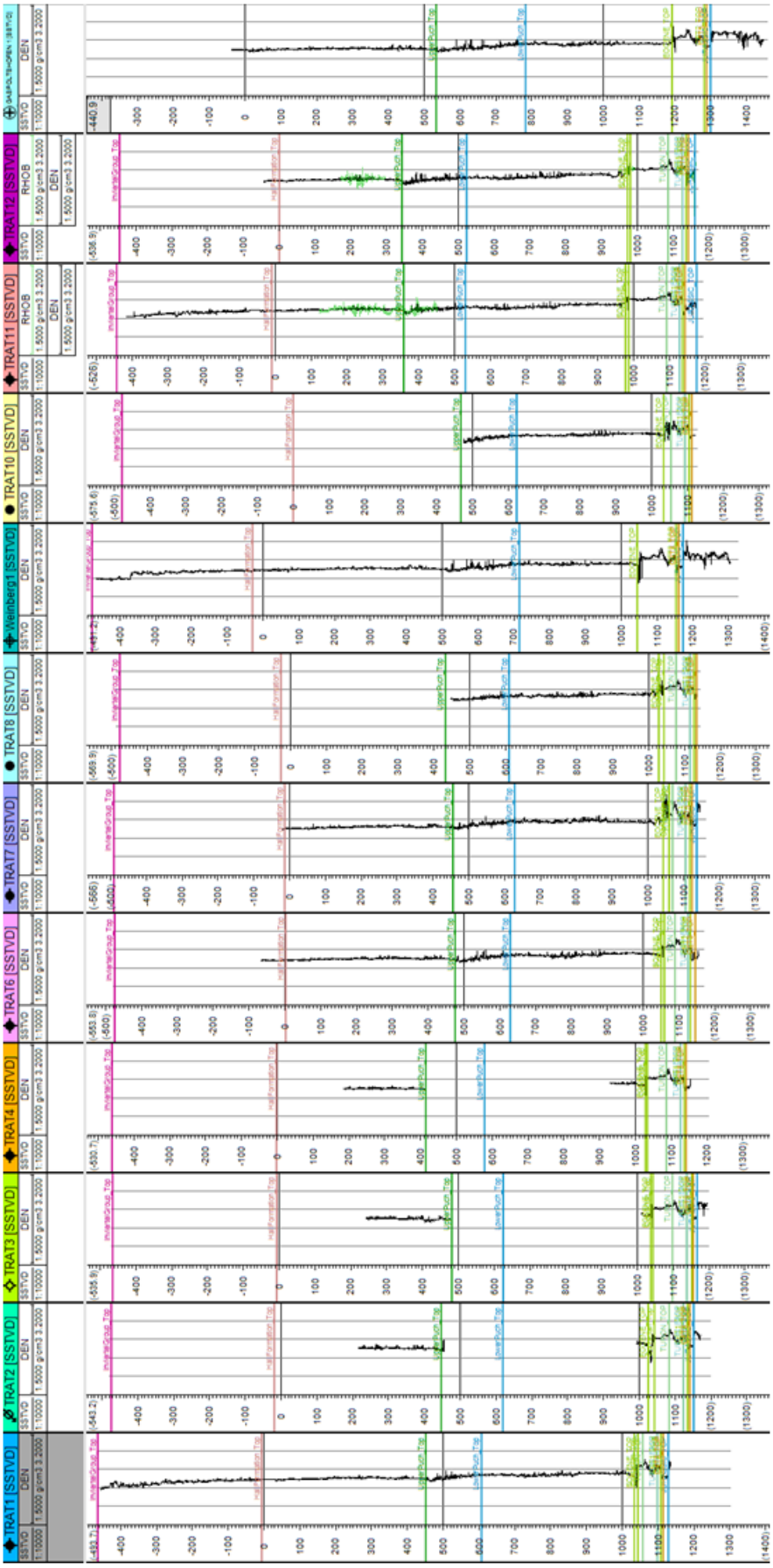

Fig. 5.8 **Calculated density logs based on Gardner´s Equation (Gardner et al., 1974). The black tracks are the calculated density logs, Green tracks in TRAT11 and TRAT 12 are the measured RHOB logs, which form the base for Gardner equation.**

The density logs are important for the calculation of lithostatic gradients. Multiplying the rock density (kg/m³) times the acceleration due to gravity (9.8 m/s²) over a depth interval gives the overburden pressure. The sampling interval of 0.15 m is used as depth interval. The resulting pressures for each depth interval are summed up to the lithostatic gradient (red curve in Fig. 5.9). The conversion factor from Pascal (Pa) to bar is 10^{-5}. The hydrostatic gradient (blue line) is calculated by multiplying the water density (kg/m³) times the acceleration due to gravity (9.8 m/s²) and depth. The hydrostatic gradient represents the pore pressure of interconnected pores up to the earth´s surface. The pressure data plotted for water, oil, gas and mixtures of oil and water are measurements from open hole tests.

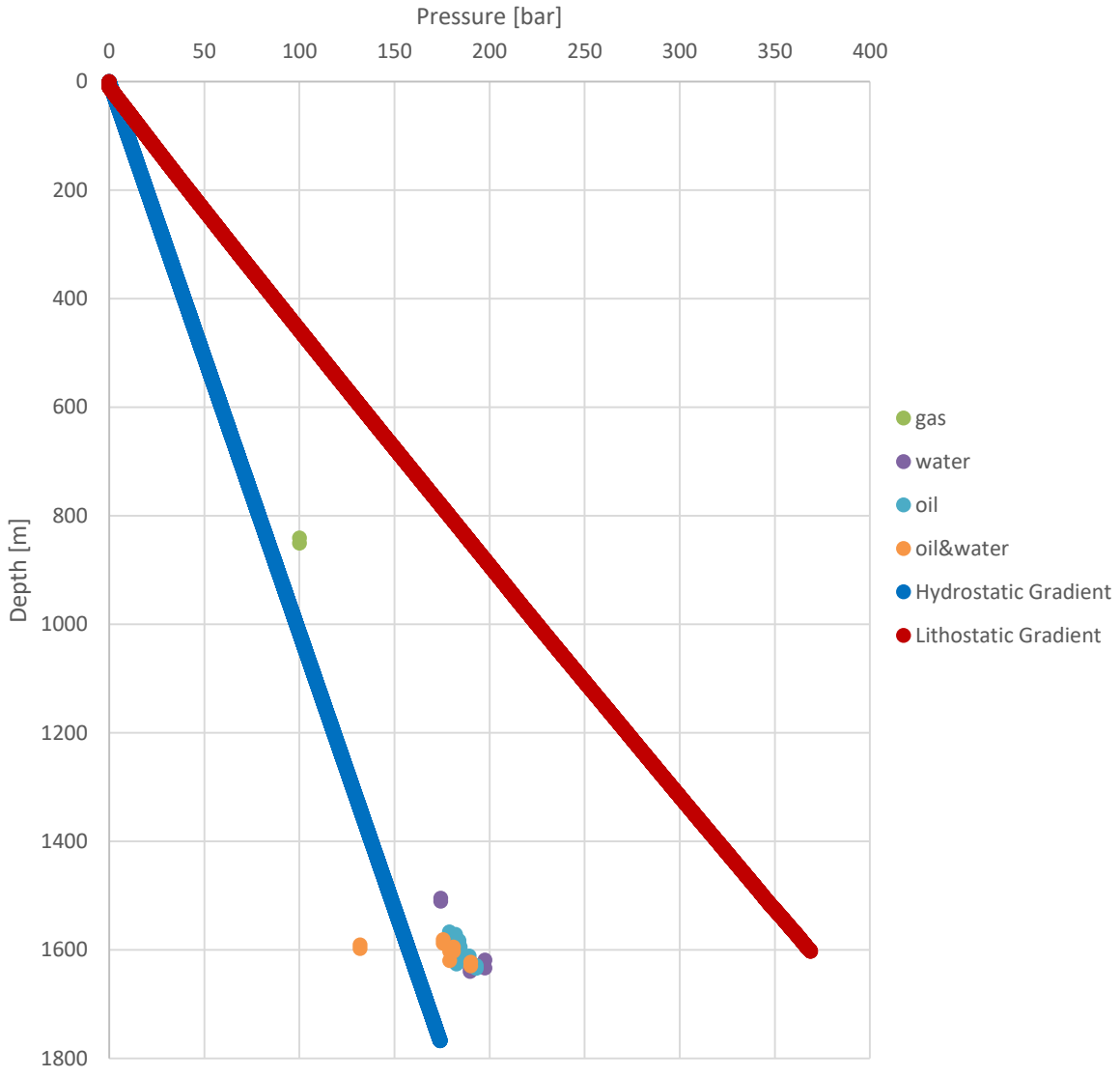

Fig. 5.9 **Pressure gradients for the Trattnach field.**
The red line is the lithostatic gradient, the blue line the hydrostatic gradient. The green data point is the pressure from an open hole test (OHT) of the gas bearing Hall Formation. The oil and water pressure data is also from OHTs in Eocene, Turonian, Cenomanian and Jurassic units.

5.2.2 Porosity

Core porosity measurements exist for the reservoir succession. The Cenomanian sandstones are a relatively thin lithologic unit, resulting in a relatively flat velocity – porosity trend. In Fig. 5.10 the measured core porosities from all wells are plotted against compressional velocities. The usual trend of decreasing velocity with increasing porosity is not visible, but looking at the different formation, CET2 and CET3 show a much clearer trend than CET1. An explanation is the higher clay content in CET1, which causes a scatter around the velocity – porosity trend (Avseth et al., 2005).

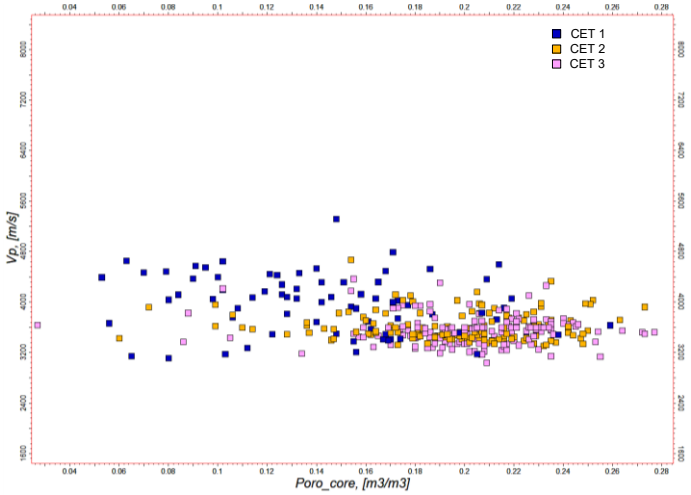

Fig. 5.10 **Velocity – porosity trend for Cenomanian reservoir sandstones. The data includes core porosity measurements from all wells. Nearly horizontal velocity – porosity trends are observed for all three Cenomanian sandstone units.**

Calculating the shear velocities of sandstones requires porosity data. The reservoir sections have core porosity measurements, whereas the other sections lack in porosity measurements. Wyllies time – average equation is used to calculate the porosity from sonic measurements (Wyllie et al., 1956). The apparent porosity (ϕ_w) is calculated by dividing the compressional wave slowness of the porous rock (Δt_p) and the matrix material ($\Delta t_{p,ma}$) by the slowness of the fluid (Δt_{fl}) present in the pore space and the matrix material. This is a heuristic equation and the best fit is achieved for water saturated and well compacted sandstones. When applied to unconsolidated sandstones, Wyllie's time average porosities are overestimated. To compensate for these optimistic porosities a lack of compaction correction factor (C_p) is applied (Eq. 22). This factor ranges between 1.0 and 1.8 for Δt values in µs/ft and is calculated by dividing the sonic transit time in shales (Δt_{shale}) by 100 (Raymer et al., 1980).

$$\phi_w = \frac{\Delta t_p - \Delta t_{p,ma}}{\Delta t_{fl} - \Delta t_{p,ma}} \quad \text{Eq. 21}$$

$$\phi_c = \phi_w * \frac{1}{C_p} \quad \text{Eq. 22}$$

$$C_p = \frac{\Delta t_{shale}}{100} \quad \text{Eq. 23}$$

The compressional wave slowness of the porous rock (Δt_p) is available as a logging measurement. Literature values (Table 5.2) are used for compressional slowness of the matrix material ($\Delta t_{p,ma}$) and of the pore fluid (Δt_{fl}). For all formations the fluid is treated as saltwater mud filtrate with Δt_{fl} = 607 µs/m (after Schoen, 2004).

Values from (Rider et al., 2011)		**Values from** (Schoen, 2004)	
Lithology	**Range for Δtp,ma [µs/m]**	**Lithology**	**Value for Δtp,ma [µs/m]**
Sandstone (ϕ 5-20%)	167 - 187	**Sandstone ϕ > 10 %**	182
Limestone (ϕ 5-20%)	155 - 173	**Sandstone ϕ < 10 %**	168
Shale	205 - 548		
Saltwater	541 - 656		

Table 5.2 Sonic matrix compressional slowness (after Rider et al., 2011; Schoen, 2004).

Sandstones with a porosity greater than 10 % have a $\Delta t_{p,ma}$ of 182 µs/m, those with a porosity smaller than 10 % have lower matrix slowness 168 µs/m. The Innviertel Group and the Hall Formation contain a mixture of shale and sand, the porosity is calculated with a matrix slowness of 200 µs/m. For the two Puchkirchen formations a matrix slowness of 210 µs/m is used, this reflects the increasing shale content compared to the two uppermost formations.
The Lithothamnium Limestone porosity is calculated with a matrix slowness of 173 µs/m and the porosity of the Coniacian and Turonian marls fitted the NPHI logs best with a matrix slowness of 155 µs/m. The applied time-average equations for each unit are shown in appendix 10.2 “Porosity Calculation”.

A quality control of the porosity data is performed by comparing the calculated porosities with the laboratory measurements. Porosity measurements on core plugs of the reservoir and seal rock (CET1, 2 and 3) were performed by RAG (see red dots in Fig. 5.11). The calculated porosity (black line in the first column) and the core porosities (red dots) show a good

correlation. Additionally the permeability (green dots in the second column) of the Cenomanian succession is displayed. These measurements were performed by RAG during the core analysis in the 1970s.

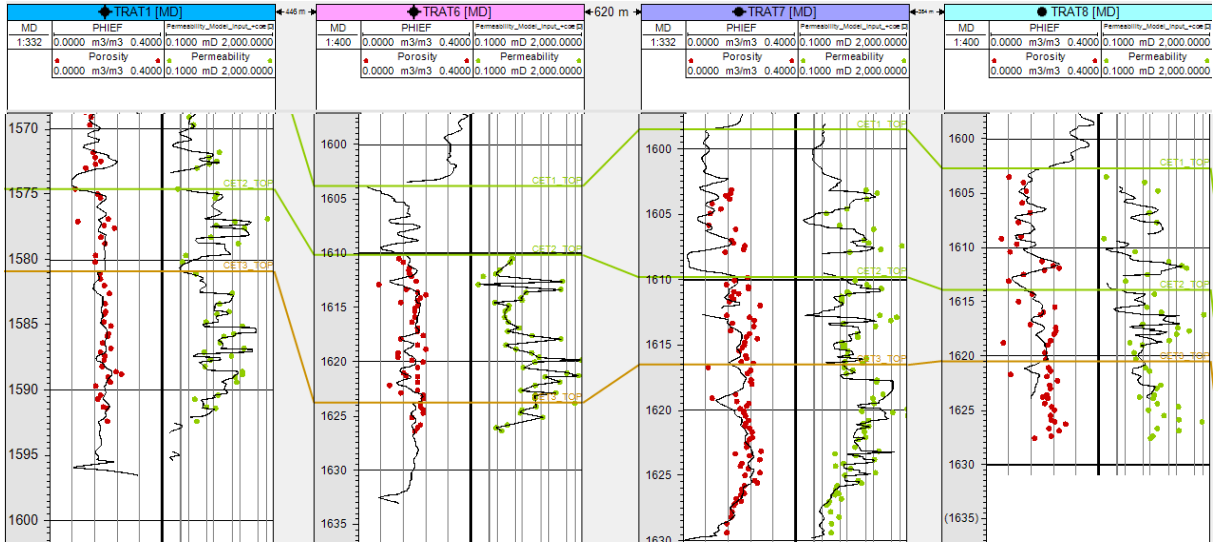

Fig. 5.11 Quality control of the calculated porosity logs.
Laboratory measurments (red dots) and the calculated porosity log (black line). Permeability measurements are displayed as green dots.

The resulting porosity logs for all wells are displayed in Fig. 5.12. The gaps in TRAT2, 3 and 4 are a result of missing sonic measurements. Without sonic logs a porosity calculation using Wyllies's time-average equation is not possible.

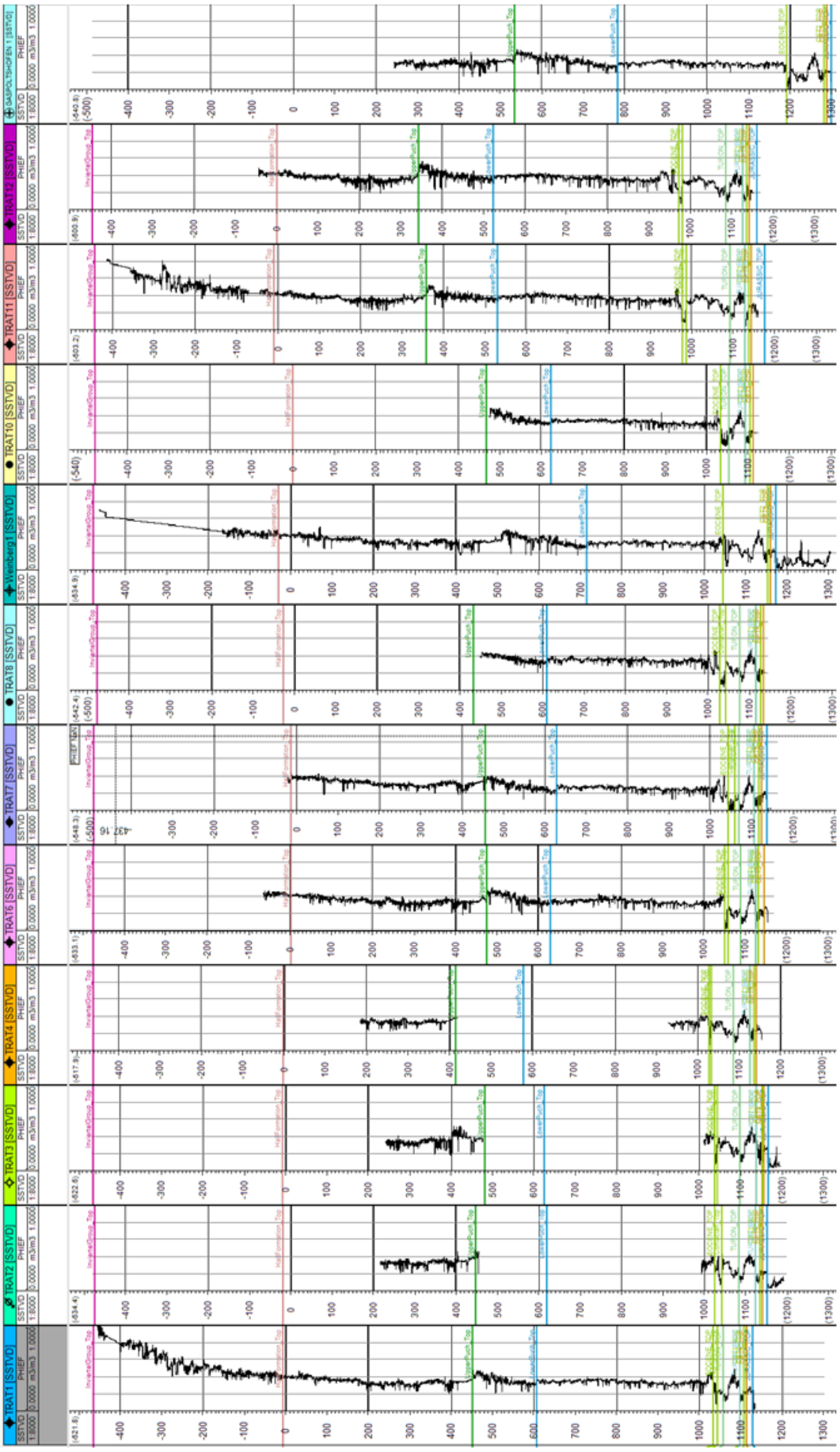

Fig. 5.12 Calculated porosity logs based on Wyllie's time-average equation (Wyllie et al., 1956).

Porosities of the Innviertel Group reach values up to 60 %, because of the highly porous structure of clay components. The porosity in sedimentary basins is strongly controlled by compaction and show a nonlinear porosity decrease with depth (Avseth et al., 2005). Meaning that porosity of sands and shales decreases at shallow depths more rapidly than at greater depths. This is due to packing changes and grain deformation (Avseth et al., 2005). To consider these porosity variations with depth, the clay- dependent exponential regression model from (Ramm et al., 1994) has been applied.

$$\boldsymbol{\phi = A * e^{-(\alpha+\beta*C1)Z}} \qquad \textbf{Eq. 24}$$

$$\boldsymbol{C_1 = \frac{V_{Cl}}{V_{qz}}} \qquad \textbf{Eq. 25}$$

Using Eq. 24 allows the calculation of fitted regression curves for sandstones, shales or mixtures of both lithologies. The porosity is dependent on an initial porosity (A) at zero depth, the clay index (C_1), depth and two regression coefficients α and β, which describe the grain frameworks compressibility. Sandstones have spherical grains this allows for a denser packing and makes the grain framework, compared to shales relatively stiff. Shales are very soft and easy to deform, the initially arbitrary aligned clay particles show a high initial porosity and will rearrange during compaction. This results in a higher porosity loss for shales during burial (Avseth et al., 2005). Fig. 5.13 shows the derived porosity depth trends for sandstones, shales and a mixture of sand and shale. All fits have been performed by the method of least squares with an iterative change of the parameters of α and β. A regression curve is calculated for a mixture of sand and shale to fit the uppermost interval of the Innviertel Group (red curve). A second sand-shale regression curve is fitted to the lower Innviertel Group and the Hall Formation (yellow curve). The blue curve is fitted to sandstones of the Puchkirchen Group, Rupelian, Eocene and Mesozoic rocks. The shale line (green) is fitted to the same depth interval as the sand line.

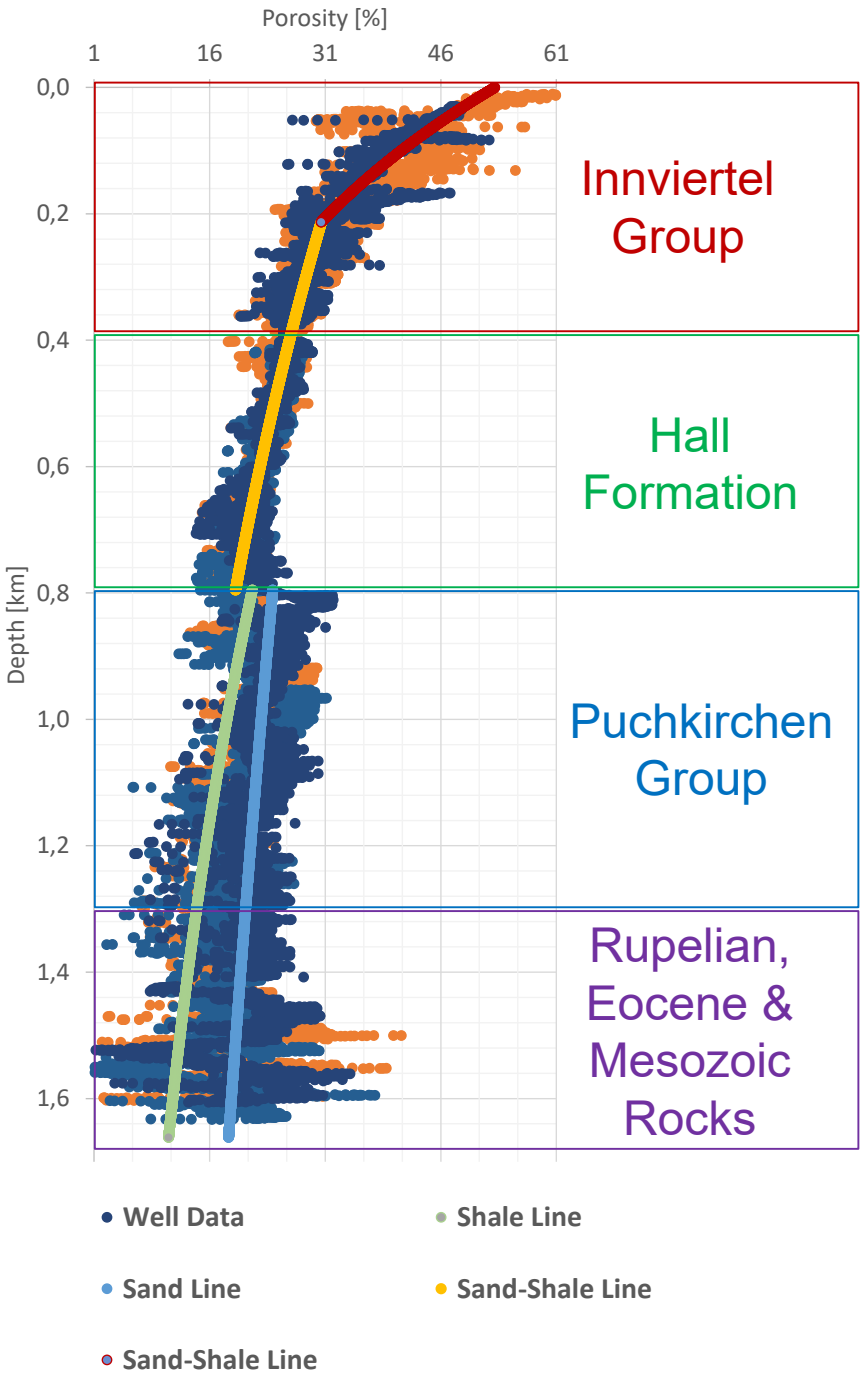

Fig. 5.13 **Porosity – depth trend for the Trattnach area.**
Sand line in blue, shale line in green and the sand-shale line in red. Well data shows porosity data, calculated during property modeling.

5.2.3 Shear velocity data

The dataset provided by RAG contained no shear slowness measurements, but a geomechanical model requires shear velocity input, otherwise, the calculation of elastic parameters is not possible. As a solution literature data was used to calculate the shear velocities for each zone. Table 5.3 shows $v_p - v_s$ relationships, it is a compilation of various empirical equations. They were derived by Castagna and Han and are based on Castagna's "mudrock-line" theory, developed in (Castagna et al., 1985; Castagna, 1993; Han et al., 1986).

Equation	Remarks	Reference
$vs = 0.8042 * v_p - 0.8559$	Sandstone	(Castagna et al., 1985)
$v_s = 0.7700 * v_p - 0.8674$	Shale	(Castagna, 1993)
$v_s = 0.7936 * v_p - 0.7868$	Shaly Sandstone	(Han et al., 1986)
$v_s = 0.8423 * v_p - 1.099$	Sandstone, Clay content > 0.25	(Han et al., 1986)
$v_s = 0.7535 * v_p - 0.6566$	Sandstone, Clay content < 0.25	(Han et al., 1986)
$v_s = 0.756 * v_p - 0.662$	Sandstone, porosity > 0.15	(Han et al., 1986)
$v_s = 0.853 * v_p - 1.137$	Sandstone, porosity < 0.15	(Han et al., 1986)
$v_s = -0.055 * v_p^2 + 1.017 * v_p - 1.031$	Limestone (watersaturated)	(Castagna, 1993)
$v_s = 0.5832 * v_p - 0.07776$	Dolomite (watersaturated)	(Castagna, 1993)

Table 5.3 Literature data: $v_p - v_s$ relationships derived by Han and Castagna (after Schoen, 2004)

Depending on the zone lithology the most suitable equation is applied, some zones contain various lithology types and these are further divided. The Eocene zone is separated into a lower sandstone and an upper limestone unit. The Rupelian consists of Fish shale, Dynow limestones and sandstones. The Turonian sequence is separated into a lower marl unit and an upper sandstone unit. Castagna's relationship for shales is applied to all marl lithologies. Table 5.4 shows which equation is applied to which zone and the resulting sonic logs are plotted in Fig. 5.14. For the entire input of the shear sonic calculation see appendix 10.3 "Shear sonic velocity calculation". When calculating shear sonic velocities for sandstones, clay content and porosity data is taken into account, as proposed by (Han et al., 1986), see Table 5.3.

Equation	Lithology	v_p - v_s Relationship
Innviertel Group	Sandstone, Gravel, Shale	$v_s = 0.8423 * v_p - 1.099$ or $v_s = 0.7535 * v_p - 0.6566$
Hall Formation	Shale, Turbidites	$v_s = 0.7936 * v_p - 0.7868$
Upper Puchkirchen	Sandstone, Gravel, Shale	$v_s = 0.8423 * v_p - 1.099$ or $v_s = 0.7535 * v_p - 0.6566$
Lower Puchkirchen	Sandstone, Gravel, Shale	$v_s = 0.8423 * v_p - 1.099$ or $v_s = 0.7535 * v_p - 0.6566$
Rupelian	Marls	$v_s = 0.7700 * v_p - 0.8674$
Dynow	Limestone	$v_s = -0.055 * v_p^2 + 1.017 * v_p - 1.031$
Fish Shale	Shale	$v_s = 0.7700 * v_p - 0.8674$
Eocene	Limestone	$v_s = -0.055 * v_p^2 + 1.017 * v_p - 1.031$
Eocene	Sandstone	$v_s = 0.756 * v_p - 0.662$ or $v_s = 0.853 * v_p - 1.137$
Coniacian	Marl	$v_s = 0.7700 * v_p - 0.8674$
Turon	Glauconitsandstone	$v_s = 0.756 * v_p - 0.662$ or $v_s = 0.853 * v_p - 1.137$
Turon	Marl	$v_s = 0.7700 * v_p - 0.8674$
Cet1	Shale	$v_s = 0.7700 * v_p - 0.8674$
Cet2	Glauconitsandstone	$v_s = 0.756 * v_p - 0.662$ or $v_s = 0.853 * v_p - 1.137$
Cet3	Glauconitsandstone	$v_s = 0.756 * v_p - 0.662$ or $v_s = 0.853 * v_p - 1.137$
JUBSS	Limestone	$v_s = -0.055 * v_p^2 + 1.017 * v_p - 1.031$

Table 5.4 Applied $v_p - v_s$ relationship for each zone (Schoen, 2004)

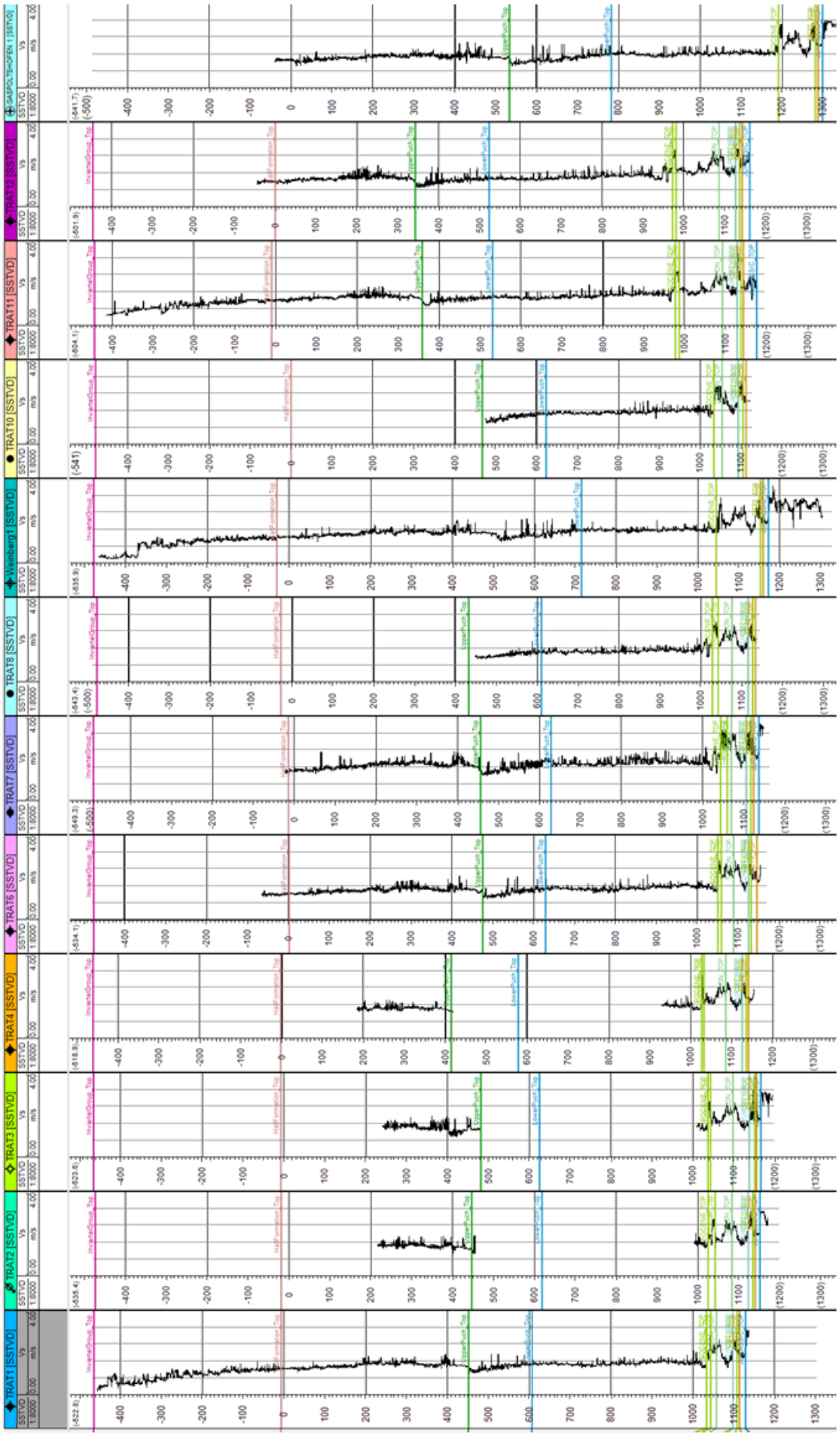

Fig. 5.14 Calculated shear sonic logs.

5.2.4 Elastic properties

The calculated shear sonic velocity and density logs enable the calculation of elastic moduli. Young's modulus (E), Poisson's ratio (υ), shear modulus (μ) and bulk modulus (k) are calculated using Eq. 26- Eq. 29 (Schoen, 2004).

$$\mathbf{E} = \boldsymbol{\rho} * \mathbf{v_s^2} * \frac{\mathbf{3v_p^2 - 4v_s^2}}{\mathbf{v_p^2 - v_s^2}} \quad \textbf{Eq. 26}$$

$$\boldsymbol{\upsilon} = \frac{\mathbf{1}}{\mathbf{2}} * \frac{\mathbf{v_p^2 - 2v_s^2}}{\mathbf{v_p^2 - v_s^2}} \quad \textbf{Eq. 27}$$

$$\boldsymbol{\mu} = \boldsymbol{\rho} * \mathbf{v_s^2} \quad \textbf{Eq. 28}$$

$$\mathbf{k} = \boldsymbol{\rho} * (\mathbf{v_p^2} - \frac{\mathbf{3}}{\mathbf{4}} * \mathbf{v_s^2}) \quad \textbf{Eq. 29}$$

The results for Young's modulus (E), in GPa, are plotted in Fig. 5.15. All wells show comparable log patterns, an increasing Young's modulus with depth for the Innviertel Group and the Hall Formation. A small decrease of stiffness beginning with the turbiditic sequence of the Puchkirchen Group. Maximum stiffness is reached for Eocene sand- and limestones. The CET1 show a higher Young's modulus than the sandy CET2 and CET3 formations. This can be explained by a higher cementation rate for CET1, compared to the reservoir rocks in CET2 and CET3. The Jurassic limestones have a strongly varying stiffness.

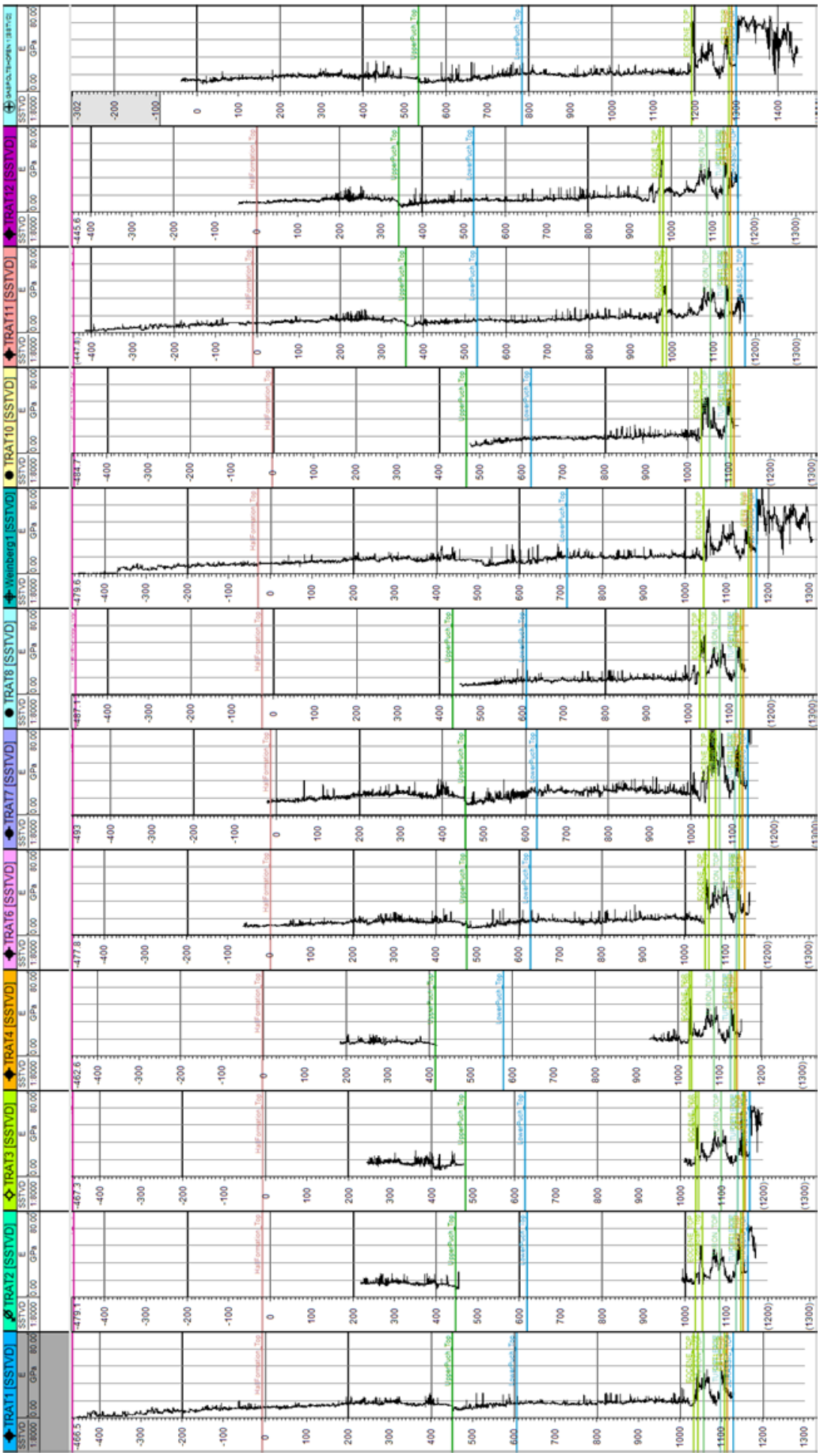

Fig. 5.15 Calculated Young's modulus.

Boundary conditions for elastic moduli are a useful tool for estimating the elastic properties of a material, they describe the upper and lower limit on the moduli, given for a characteristic mixture of constituents. This implies knowing the elastic modulus of each material, for example sand and water, and their volume fractions (Mavko et al., 1998).

One pair of bounds describing the ratio of average stress and strain within the rock was introduced by Voigt and Reuss (Voigt, 1910; Reuss, 1929) (Fig. 5.16). The upper bound assumes an iso-strain state and marks the uppermost limit of possible elastic moduli for a mixture of two materials. It is calculated using Eq. 32. Reus introduced the lower bound model Eq. 31, an iso-stress state which forms the lowest possible elastic moduli for a mixture (Mavko et al., 1998).

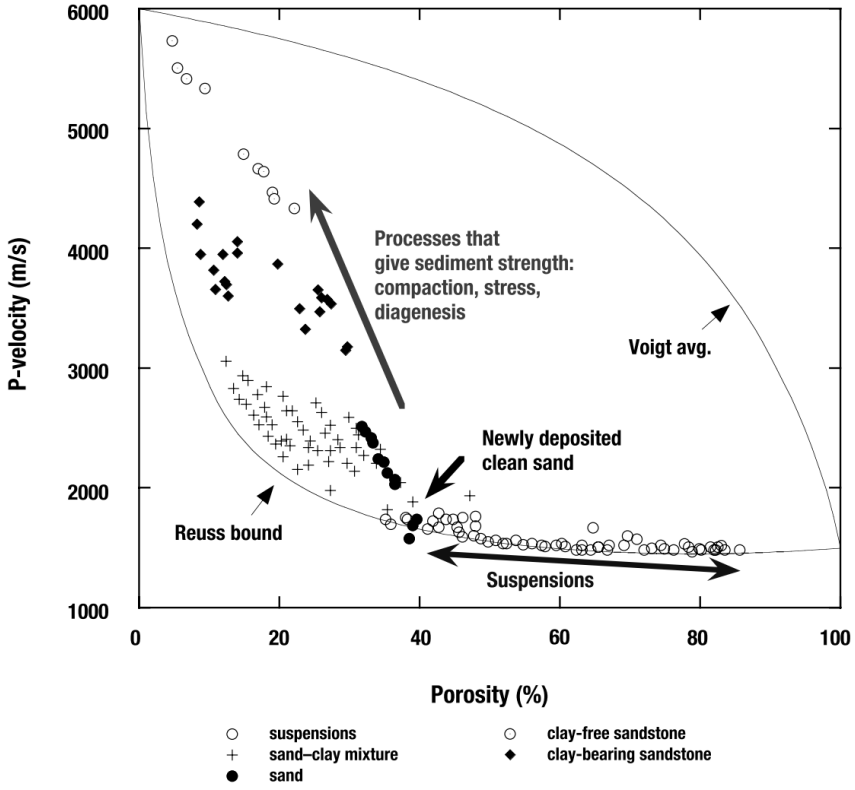

Fig. 5.16 **V_p versus porosity plot with a lower Reuss and an upper Voigt bound. The plotted data describes a water-saturated sediment (Avseth et al., 2005)**

This diagram can be used to interpret diagenetic processes of sediments. Relatively freshly deposited sediments will plot along the lower Reuss boundary, which describe the elastic behavior of a suspension. Freshly deposited clays will plot at porosities of 60 % and sandstones will deposit around 40 % depending on their sorting and grain geometry. Increasing burial and prevailing diagenetic processes like mechanical and chemical compaction will reduce the porosity and increase the velocity of sands and clays (Avseth et al., 2005).

$$K_v = \phi * K_{fl} + (1 - \phi) * K_{ma} \quad \text{Eq. 30}$$

$$K_R = \phi * K_{fl}^{-1} + (1 - \phi) * K_{ma}^{-1} \quad \text{Eq. 31}$$

$$K_{VRH} = \frac{K_v + K_R}{2} \quad \text{Eq. 32}$$

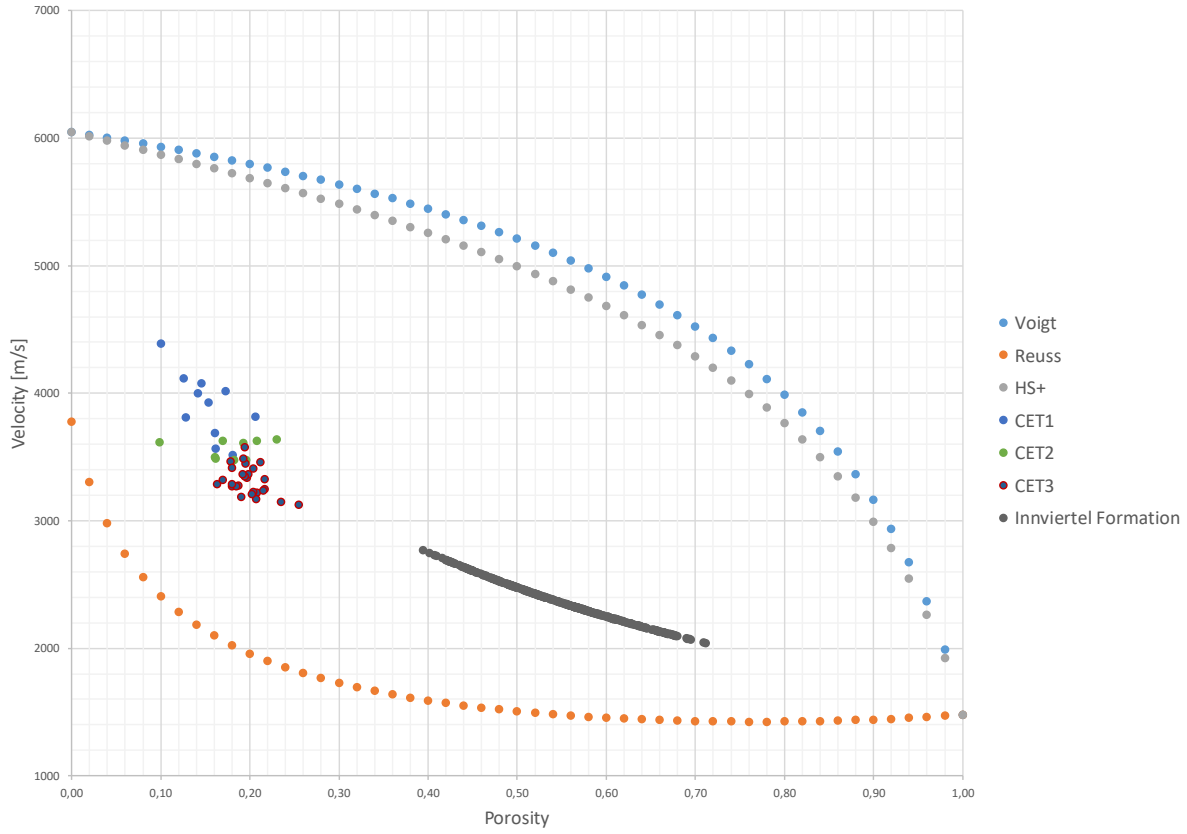

Fig. 5.17 **Velocity versus porosity plot for the Cenoman and the Hall Formation. The upper Voigt bound in blue, lower Reuss bound in orange. The plotted data shows the Cenomanian sandstones CET1-3 and the relatively uncompacted Hall formation in grey.**

The two bounds are calculated for a mixture of clean quartz sandstone and water. Quartz forms the stiff and water the soft material. Two materials with smaller differences in elastic behavior would form narrower boundaries (Avseth et al., 2005). A characteristic bulk modulus for quartz is 36 GPa, whereas that of water is 2.2 GPa (Schoen, 2004).

The Cenoman sandstones plot at porosities between 10 and 25 % with a compressional velocity of 3100 m/s down to 450 m/s. It can be seen that the strongly cemented sandstones from CET1 plot at higher velocities and lower porosities than CET2 and CET3 sandstones. The plotted data from the Innviertel Group (grey dots) have not undergone any major diagenetic processes which increased their strength and plot near the recently deposited sediments.

Another set of boundary conditions is introduced by Hashin – Shtrikmann (Hashin et al., 1963), these are the narrowest possible bounds for estimating an elastic modulus by plotting porosity versus velocity. Alternatively the calculated bulk moduli can be evaluated by plotting them in an effective bulk modulus versus porosity diagram.

$$\mathbf{K_{+}^{HS}} = \mathbf{K_{ma}} + \frac{\boldsymbol{\phi}}{(\mathbf{K_{fl}} - \mathbf{K_{ma}})^{-1} + (\mathbf{1} - \boldsymbol{\phi}) * (\mathbf{K_{ma}} + * \frac{\mathbf{4}}{\mathbf{3}} \boldsymbol{\mu}_{\mathbf{ma}})^{-1}} \quad \textbf{Eq. 33}$$

$$\mathbf{K_{-}^{HS}} = \mathbf{K_{fl}} + \frac{(\mathbf{1} - \boldsymbol{\phi})}{(\mathbf{K_{ma}} - \mathbf{K_{fl}})^{-1} + \boldsymbol{\phi} * \mathbf{K_{fl}^{-1}}} \quad \textbf{Eq. 34}$$

Hashin and Shtrikman define the bounds by interchanging the moduli of the two materials (Hashin et al., 1963). The upper bound is defined by a core of soft material surrounded by a stiff material forming a shell around the core. The lower bound is calculated by switching the two materials, now the softer material defines the shell and stiffer material the core. Eq. 33 is used for the upper bound calculation and Eq. 34 for calculating the lower bound (Mavko et al., 1998).

Fig. 5.18 shows the calculated bulk moduli for the TRAT1 borehole plotted against the porosity. The upper boundaries Voigt (orange) and Hashin-Shtrikman (yellow) mark the uppermost limit of elastic moduli for a mixture of materials. The lower boundaries of Reuss and Hashin-Shtrikman are exactly the same, because the shear modulus of water is zero. When using water as soft material the modulus of grains in a pore fluid is described by the lower bounds (Avseth et al., 2005).
The calculated bulk modulus is not correct for the high porosity area between 70 and 90 %, this data is from the uppermost logging interval where high sonic velocity measurements lead to unrealistic values for the bulk modulus. The same applies to the overestimated bulk modulus (>32 GPa) for a porosity lower than 10 %. This data is from the JUBSS and was measured at the end of the logging period. All other data fits between the boundaries and show a similar trend to the average bulk modulus introduced by Hill (grey dotted line) (Hill, 1952).

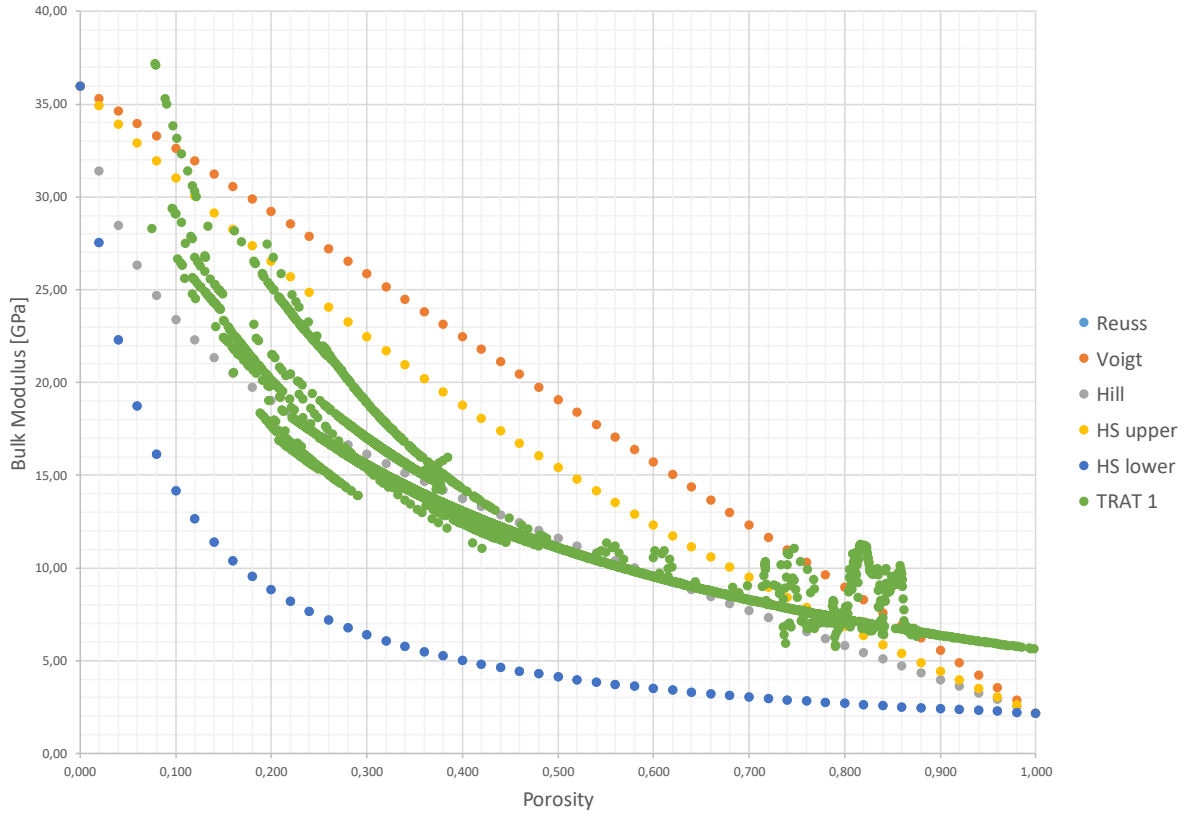

Fig. 5.18 **Calculated bulk modulus.**
The upper bounds are Voigt (orange) and Hashin-Shtrikman (yellow). The dotted grey line is the calculated Hill average. The two lower bounds are identical (blue). The calculated bulk modulus for the entire TRAT1 section is plotted in green.

5.2.5 Uniaxial compressive strength

An additional input during geomechanical material modeling is the uniaxial compressive strength. A series of unconfined compression tests are performed in this section to determine the uniaxial compression strength (UCS) of core plug samples from the reservoir section of the wells Trattnach 6 and Trattnach 7. When performing an unconfined compression test an axial load is applied and gradually increased till failure occurs. This test is a simplification of the triaxial compression test, where an additional confining pressure allows even higher axial loading (Fjar et al., 2008). A triaxial compression or shear test could not be performed, because these tests require a minimum specimen diameter of 50 mm and the core plugs from the Trattnach wells have a median diameter of 29 mm. Ideally the samples should have a height to length ratio of 2 up to 2.5 and a reduction factor should be applied to those samples which have a height to length ratio in the rage between one and two (Witt, 2008). As no sample from the investigated wells has a height to length ratio larger than two, all measured unconfined compressive strength values are reduced by the factor calculated with Eq. 35.

$$\textbf{reduction factor} = \frac{8}{7 + 2 * \frac{h}{d}} \qquad \text{Eq. 35}$$

Sample Preparation

A uniaxial compression test requires plane parallel surfaces, thus both ends of all seventeen core plugs were cut using a water cooled stone cutting saw at the Chair of Subsurface Engineering of the Montanunivesitaet Leoben. All samples have different heights with the goal to maintain as much height as possible during the preparation of plane parallel surfaces.

Measurement

The uniaxial compressive strength has been determined using the testing facility at the Chair of Subsurface Engineering. This facility is designed to determine the Young's modulus via a fully automated testing procedure which evaluates the Young's modulus using force controlled loading and unloading cycles. Due to the small height of the samples the extensometers could not be mounted. Therefore the fully automated testing procedure could not be performed. Instead a displacement controlled program is used to determine the uniaxial compressive strength, using an axial loading of 1.2 mm per minute.

The plane parallel cylindrical samples were embedded between to plane parallel pressure plates, whereby the upper one is a "kugelkalotte" fixed with springs to ensure a better force transmission.

The studied core of the Trattnach 6 well contains four core plugs. Only one of these qualified for the UCS test. The other three samples were smaller than 20 mm with a height to length ratio of 0.71 and were therefore neglected.

Eleven core plugs are available from the Trattnach 7 well and eight of those were used for the compression test. The remaining core plugs were too small and a measurement seemed redundant.

Results

TRAT701B

The TRAT701B is a core plug from well Trattnach 7, obtained at a core depth of 1617 m. It is a glauconitic sandstone sample with a diameter of 29.30 mm and a length of 26.30 mm from the CET3 horizon, see uppermost picture in Fig. 5.19. The force-time history diagram shows that failure occurred at an applied force of 11.33 kN. The corresponding uniaxial compressive strength is 16.80 MPa, a reduction factor of 0.910 is applied, resulting in a uniaxial compressive strength of 15.28 MPa for the glauconitic sandstone sample. Fig. 5.19 shows the stress-strain curve, its slope results in a tangential modulus of 2.16 GPa.

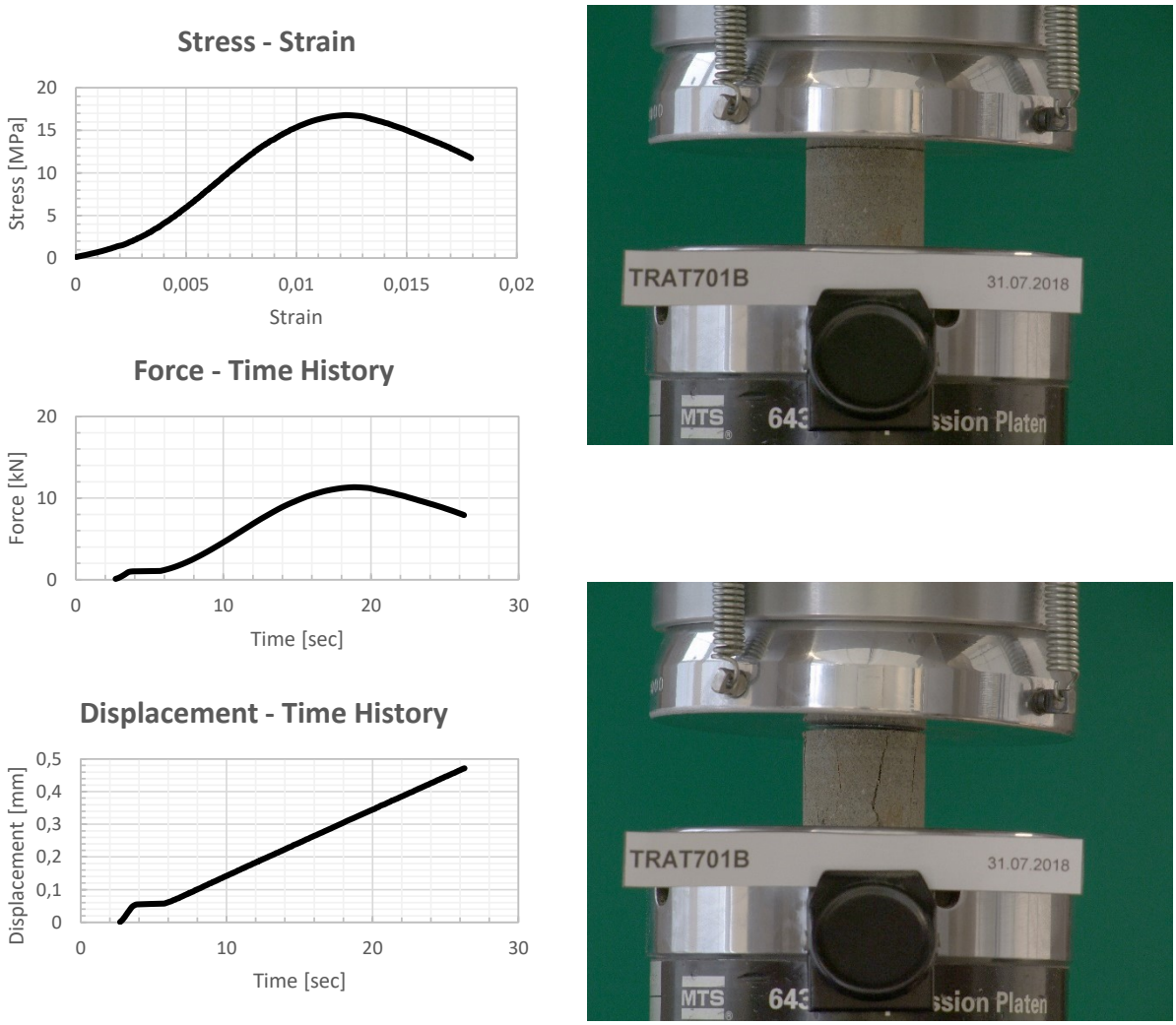

Fig. 5.19 Test Results TRAT701B.

TRAT704A

The TRAT704A is a core plug from well Trattnach 7, obtained at a depth of 1614 m. It is a glauconitic sandstone sample with a diameter of 29.60 mm and a length of 49.40 mm from the CET2 horizon, see uppermost picture in Fig. 5.20. The force-time history diagram shows that failure occurred at an applied force of 7.96 kN. The corresponding uniaxial compressive strength is 8.84 MPa, a reduction factor of 0.774 is applied, resulting in a uniaxial compressive strength of 7.70 MPa for the glauconitic sandstone sample. Fig. 5.20 shows the stress-strain curve, its slope results in a tangential modulus of 1.43 GPa.

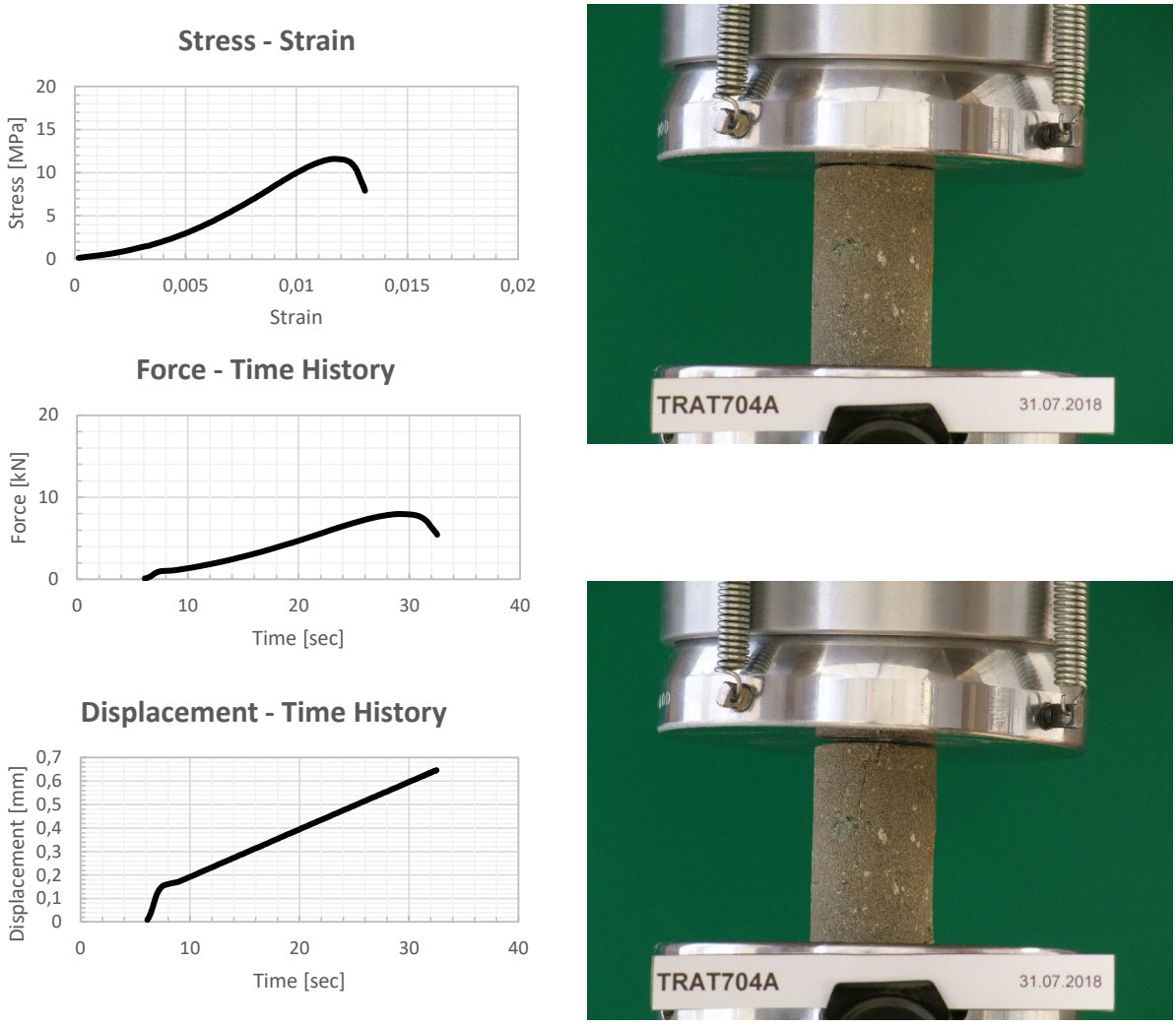

Fig. 5.20 Test Results TRAT704A.

TRAT705

The TRAT705 is a core plug from well Trattnach 7, obtained at a depth of 1613.35 m. It is a glauconitic sandstone sample with a diameter of 29.60 mm and a length of 33.20 mm from the CET2 horizon, see uppermost picture in Fig. 5.21 The force-time history diagram shows that failure occurred at an applied force of 8.07 kN. The corresponding uniaxial compressive strength is 11.74 MPa, a reduction factor of 0.865 is applied, resulting in a uniaxial compressive strength of 10.16 MPa for the glauconitic sandstone sample. Fig. 5.21 shows the stress-strain curve, its slope results in a tangential modulus of 1.36 GPa.

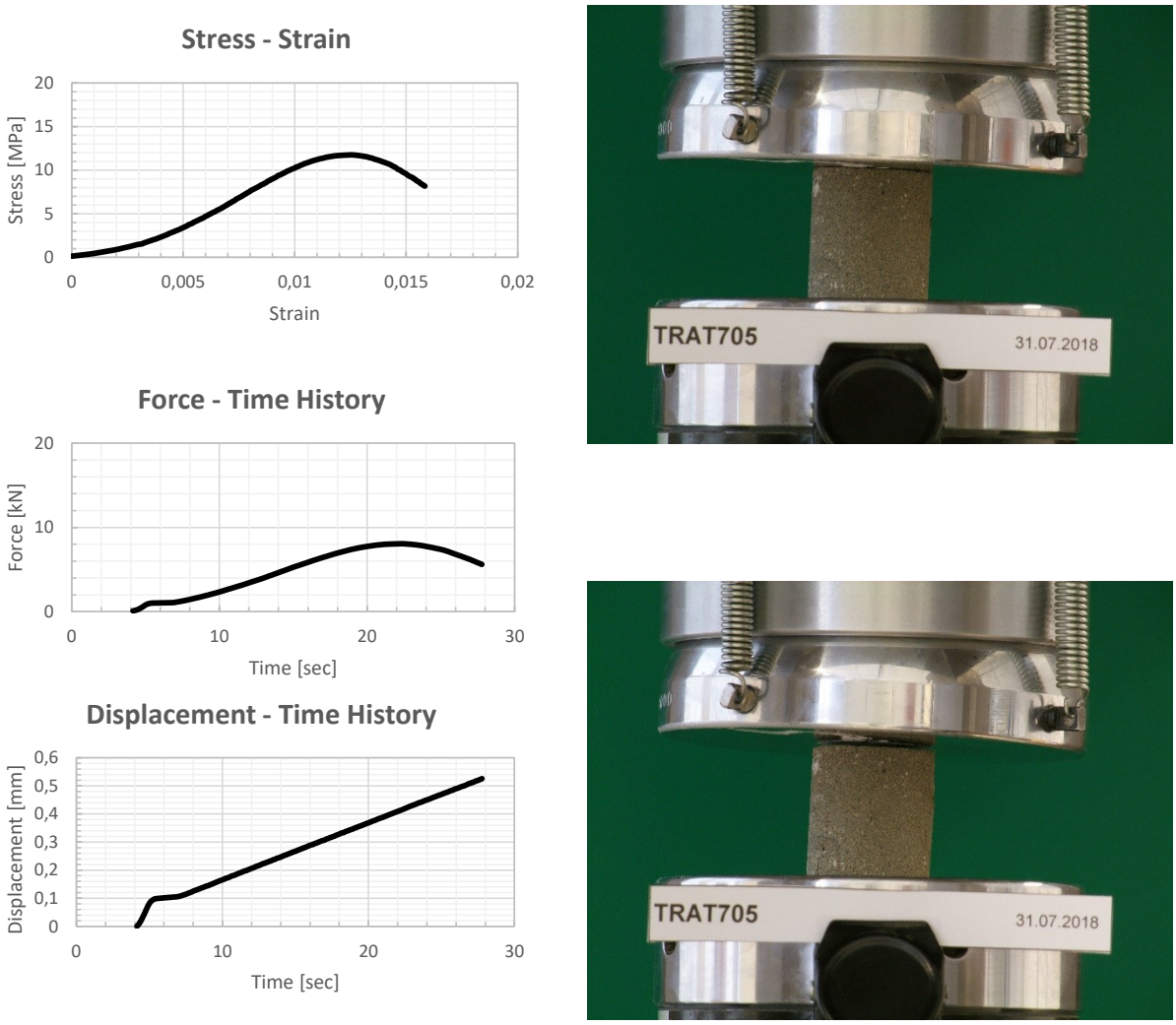

Fig. 5.21 Test Results TRAT705.

TRAT709

The TRAT709 is a core plug from well Trattnach 7, obtained at a depth of 1609.10 m. It is a white-yellow sandstone sample with a diameter of 29.40 mm and a length of 27.60 mm from the CET1 horizon, see uppermost picture in Fig. 5.22. The force-time history diagram shows that failure occurred at an applied force of 21.60 kN. The corresponding uniaxial compressive strength is 31.83 MPa, a reduction factor of 0.901 is applied, resulting in a uniaxial compressive strength of 28.68 MPa for the sandstone sample. Fig. 5.22 shows the stress-strain curve, its slope results in a tangential modulus of 3.97 GPa.

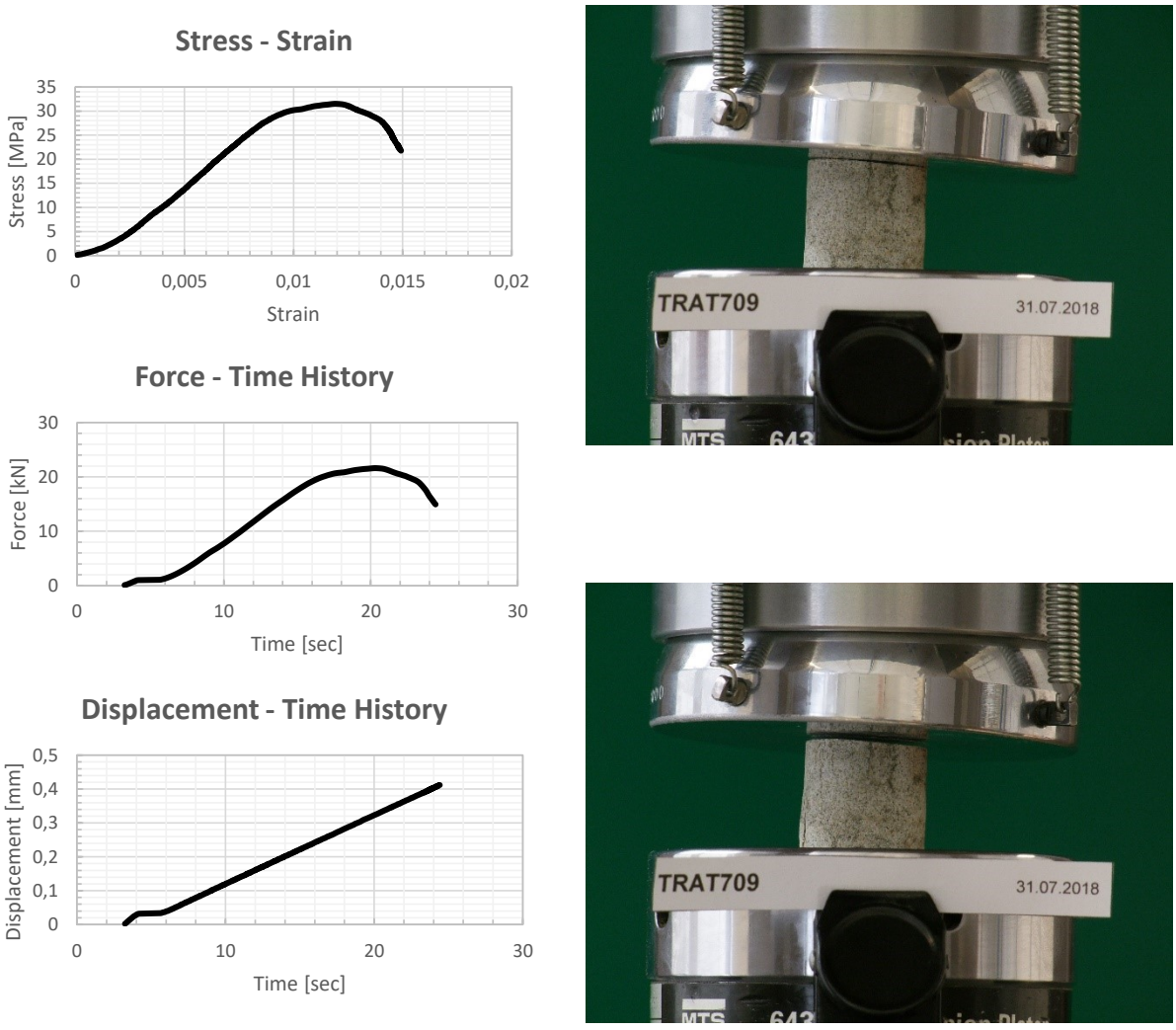

Fig. 5.22 Test Results TRAT709.

TRAT712A

The TRAT12A is a core plug from well Trattnach 7, obtained at a depth of 1606.85 m. It is a strongly weathered glauconitic sandstone sample with a diameter of 28.80 mm and a length of 37.90 mm from the CET1 horizon, see uppermost picture in Fig. 5.23. The force-time history diagram shows that failure occurred at an applied force of 2.58 kN. The corresponding uniaxial compressive strength is 3.97 MPa, a reduction factor of 0.831 is applied, resulting in a uniaxial compressive strength of 3.30 MPa for the glauconitic sandstone sample. Fig. 5.23 shows the stress-strain curve, its slope results in a tangential modulus of 0.32 GPa.

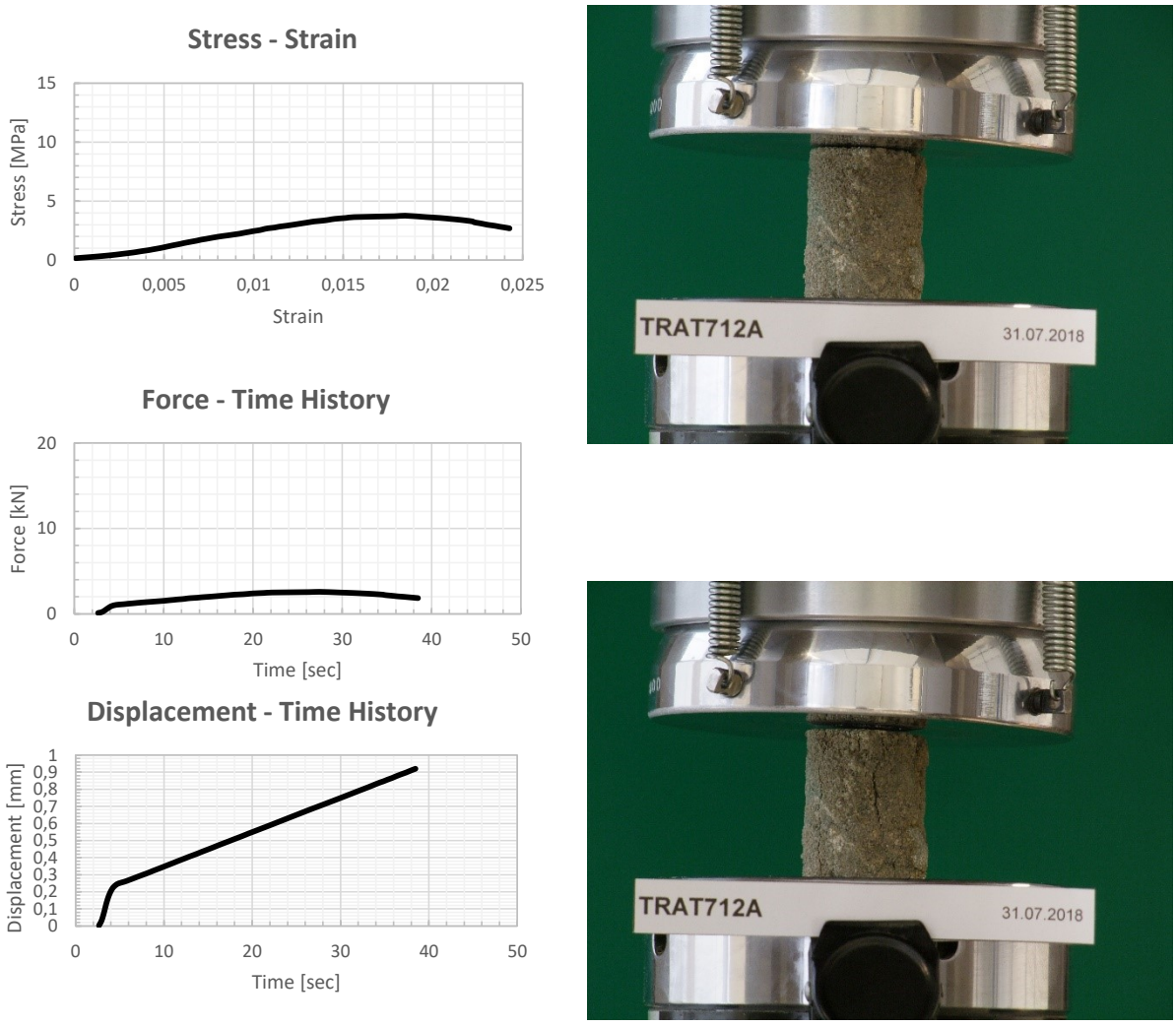

Fig. 5.23 Test Results TRAT712A.

TRAT714A

The TRAT714A is a core plug from well Trattnach 7, obtained at a depth of 1621.90 m. It is a glauconitic sandstone sample with a diameter of 29.70 mm and a length of 36.50 mm from the CET3 horizon, see uppermost picture in Fig. 5.24. The force-time history diagram shows that failure occurred at an applied force of 13.86 kN. The corresponding uniaxial compressive strength is 19.95 MPa, a reduction factor of 0.846 is applied, resulting in a uniaxial compressive strength of 16.87 MPa for the glauconitic sandstone sample. Fig. 5.24 shows the stress-strain curve, its slope results in a tangential modulus of 2.86 GPa.

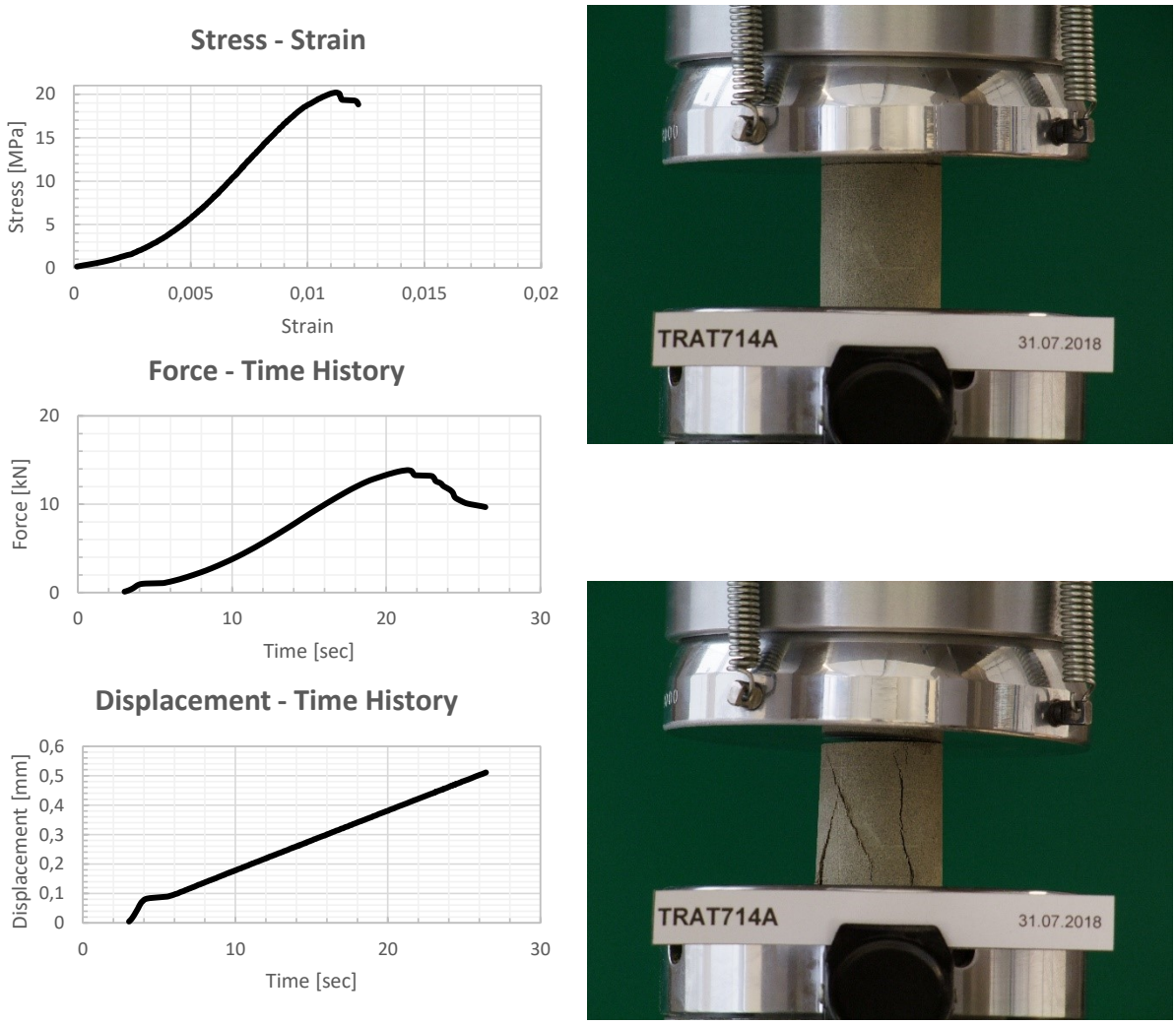

Fig. 5.24 Test Results TRAT714A.

TRAT714B

The TRAT714B is a core plug from well Trattnach 7, obtained at a depth of 1621.90 m. It is a glauconitic sandstone sample with a diameter of 29.70 mm and a length of 37.30 mm from the CET3 horizon, see uppermost picture in Fig. 5.25. The force-time history diagram shows that failure occurred at an applied force of 13.67 kN. The corresponding uniaxial compressive strength is 19.72 MPa, a reduction factor of 0.841 is applied, resulting in a uniaxial compressive strength of 16.59 MPa for the glauconitic sandstone sample. Fig. 5.25 shows the stress-strain curve, its slope results in a tangential modulus of 2.80 GPa.

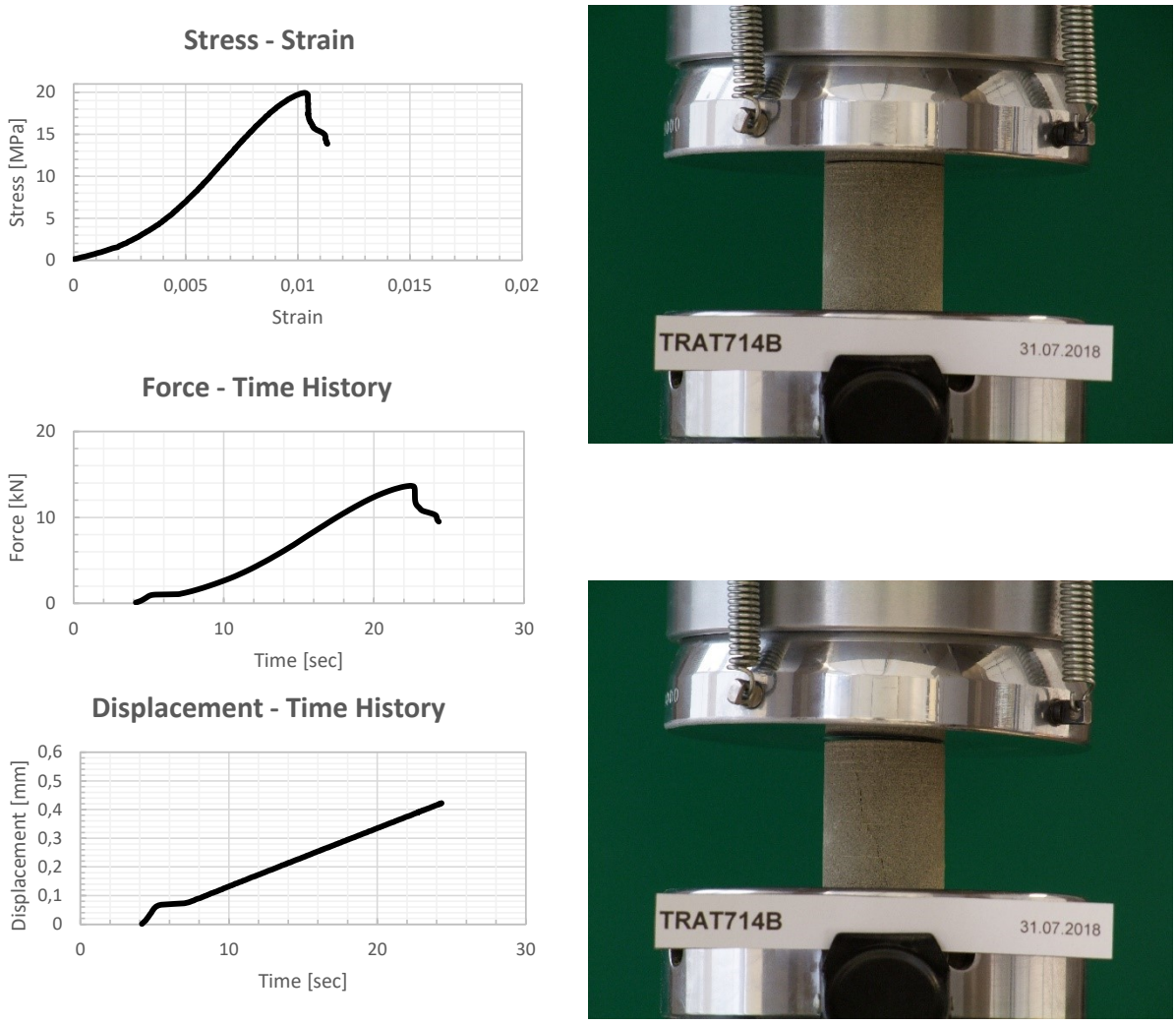

Fig. 5.25 Test Results TRAT714B.

TRAT718

The TRAT718 is a core plug from well Trattnach 7, obtained at a depth of 1619.50 m. It is a glauconitic sandstone sample with a diameter of 29.60mm and a length of 39.50 mm from the CET3 horizon, see uppermost picture in Fig. 5.26. The force-time history diagram shows that failure occurred at an applied force of 11.71 kN. The corresponding uniaxial compressive strength is 17.03 MPa, a reduction factor of 0.827 is applied, resulting in a uniaxial compressive strength of 14.09 MPa for the glauconitic sandstone sample. Fig. 5.26 shows the stress-strain curve, its slope results in a tangential modulus of 1.55 GPa.

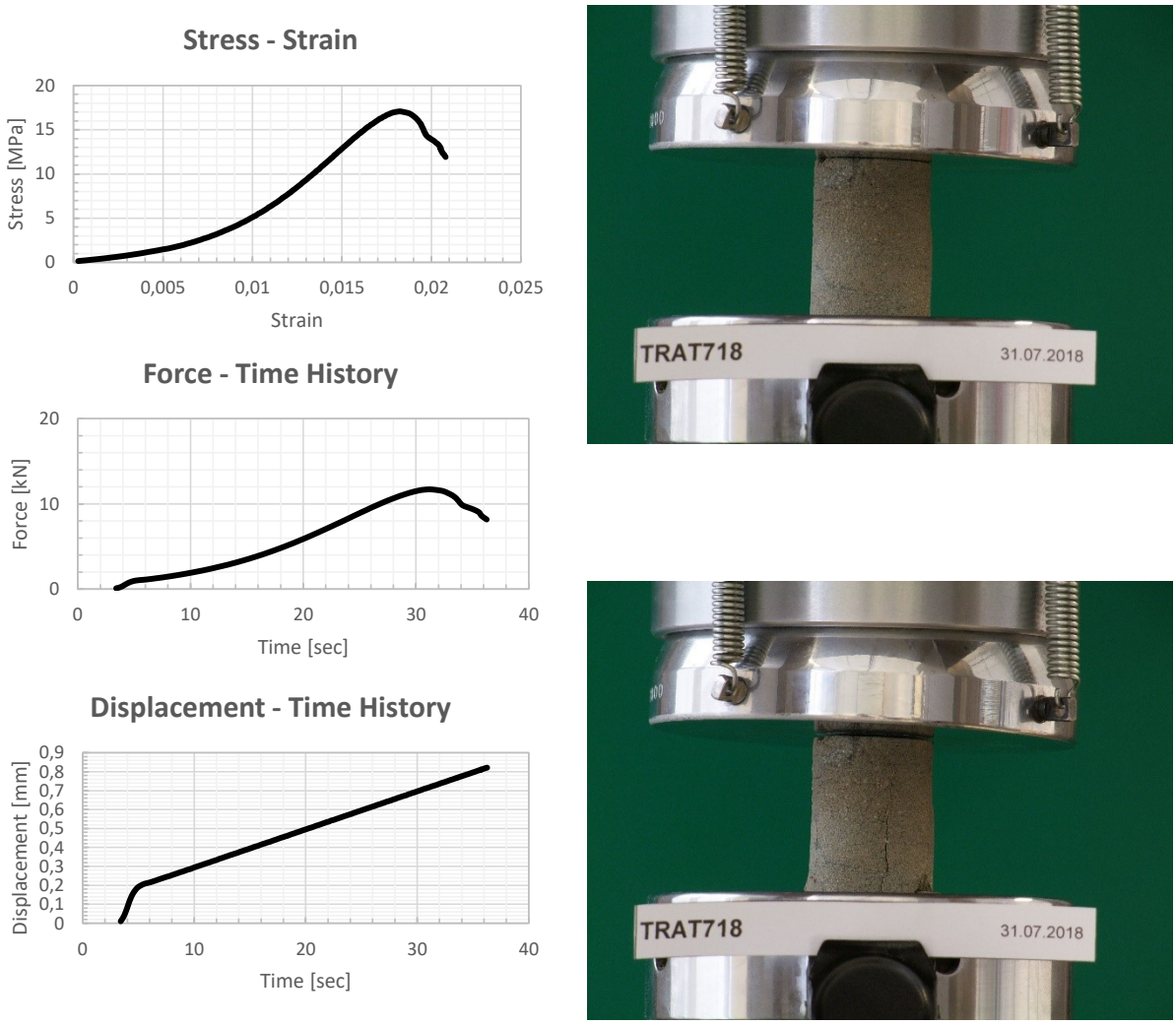

Fig. 5.26 Test Results TRAT718.

TRAT615

The TRAT615 is a core plug from well Trattnach 6, obtained at a depth of 1628 m. It is a glauconitic sandstone sample with a diameter of 29.70 mm and a length of 31.40 m from the CET3 horizon, see uppermost picture in Fig. 5.27. The force-time history diagram shows that failure occurred at an applied force of 17.22 kN. The corresponding uniaxial compressive strength is 24.87 MPa, a reduction factor of 0.878 is applied, resulting in a uniaxial compressive strength of 21.83 MPa for the glauconitic sandstone sample. Fig. 5.27 shows the stress-strain curve, its slope results in a tangential modulus of 2.54 GPa.

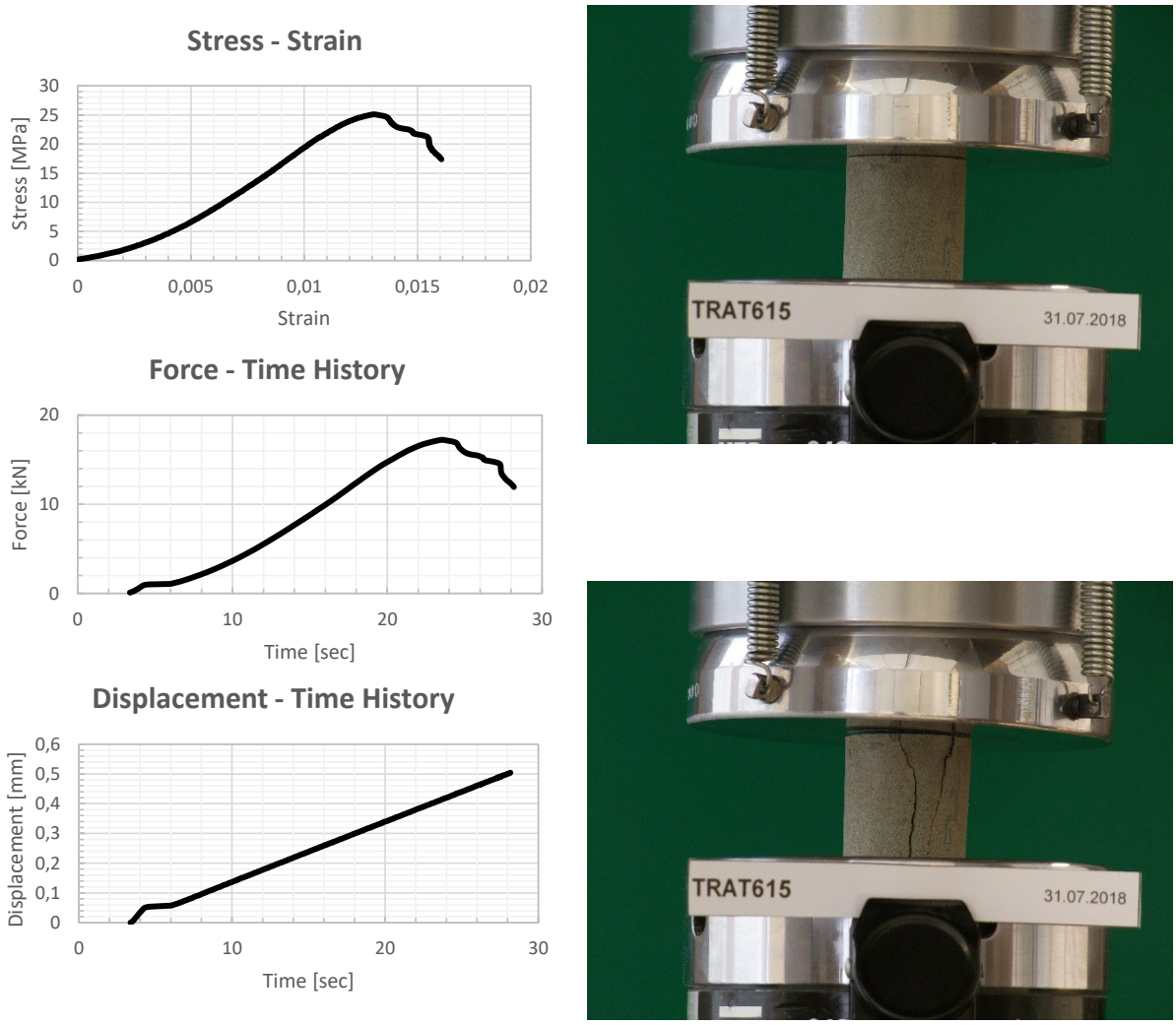

Fig. 5.27 Test Results TRAT615.

The table 5.5 summarizes all measured and calculated data required for the determination of the uniaxial compressive strength. The original data of the measured probe geometries is in the appendix 10.4 "Core plug data". Diameter and length are measured three times and the average of the three measurements is the input for table 5.5. The mass is measured in the laboratory and the density is calculated. Maximum force applied (F,max) is determined by the testing apparatus. The uniaxial compressive strength (UCS) is calculated by dividing the maximum force applied by the counter square area (CS-area) for each sample.

The height to diameter ratio (h/d) is calculated and the calculated reduction factor is applied to all core samples. The new uniaxial compressive strength includes the reduction factor (UCS-RF) and is used for further analysis of rock strength. The porosity, matrix density and permeability measurements were performed by RAG.

Property	Core Samples									
	701B	704A	704B	705	709	712A	714A	714B	718	615
Diameter [mm]	29,30	29,60	29,60	29,60	29,40	28,80	29,70	29,70	29,60	29,70
Length [mm]	26,30	49,40	32,40	33,20	27,60	37,90	36,50	37,30	39,50	31,40
Mass [g]	35,88	69,60	45,06	46,31	45,59	50,74	51,80	52,82	56,06	46,73
Density [g/cm³]	2,10	2,05	2,02	2,03	2,43	2,06	2,04	2,04	2,06	2,15
F,max [kN]	11,33	7,96	6,07	8,07	21,60	2,58	13,86	13,67	11,71	17,22
CS-area [cm²]	6,74	6,86	6,87	6,87	6,79	6,50	6,95	6,93	6,88	6,92
UCS [MPa]	16,80	11,61	8,84	11,74	31,83	3,97	19,95	19,72	17,03	24,87
h/d	0,90	1,67	1,09	1,12	0,94	1,32	1,23	1,26	1,33	1,06
RF	0,91	0,77	0,87	0,87	0,90	0,83	0,85	0,84	0,83	0,88
UCS-RF [MPa]	15,28	8,98	7,70	10,16	28,68	3,30	16,87	16,59	14,09	21,83
Depth [m]	1617,00	1614,00	1614,00	1613,35	1609,10	1606,85	1621,90	1621,90	1619,25	1628,00
Zone	CET3	CET2	CET2	CET2	CET1	CET1	CET3	CET3	CET3	CET3
Porosity [%]	24,00	23,50	23,50	17,50	22,80	18,60	24,50	24,50	10,2/19	
$Density_{ma}$ [g/cm³]	2,7	2,72	2,72	2,71	2,69	2,67	2,69	2,69	2,67	
Permeability	15,6	23,1	23,1	6,8		225	44	44	92/2000	

Table 5.5 Applied $v_p - v_s$ relationship for each zone (Schoen, 2004)

The values of uniaxial compressive strength for the CET1 horizon are 21.60 MPa and 2.58 MPa. The low value of 2.58 MPa is due to the strong inhomogeneity of the sample TRAT12A, therefore the 21.60 MPa measured at the TRAT709 sample is assigned to the CET1 horizon, see chapter 5.4.1

Three samples are from the CET2 horizon, with a uniaxial compressive strength of 7.96 MPa (TRAT704A), 6.07 MPa (TRAT704B) and 8.07 MPa (TRAT705). The average value of 7.37 MPa is assigned to the CET2 horizon, see chapter 5.4.1

Five samples represent the CET3 horizon, with values for the uniaxial compressive strength of 11.33 MPa (TRAT701B), 13.86 MPa (TRAT714A), 13.67 MPa (TRAT714B), 11.71 MPa (TRAT718) and 17.22 MPa (TRAT615). The average value of 13.56 MPa is assigned to the CET3 horizon, see chapter 5.4.1

The uniaxial compressive strength could not be determined for all other lithologies, average literature values (Schoen, 2004; Fig. 5.27) are assigned to each rock material, see chapter 5.4.1. The assigned values are given in bar, the conversion factor from Megapascal to bar is 10.

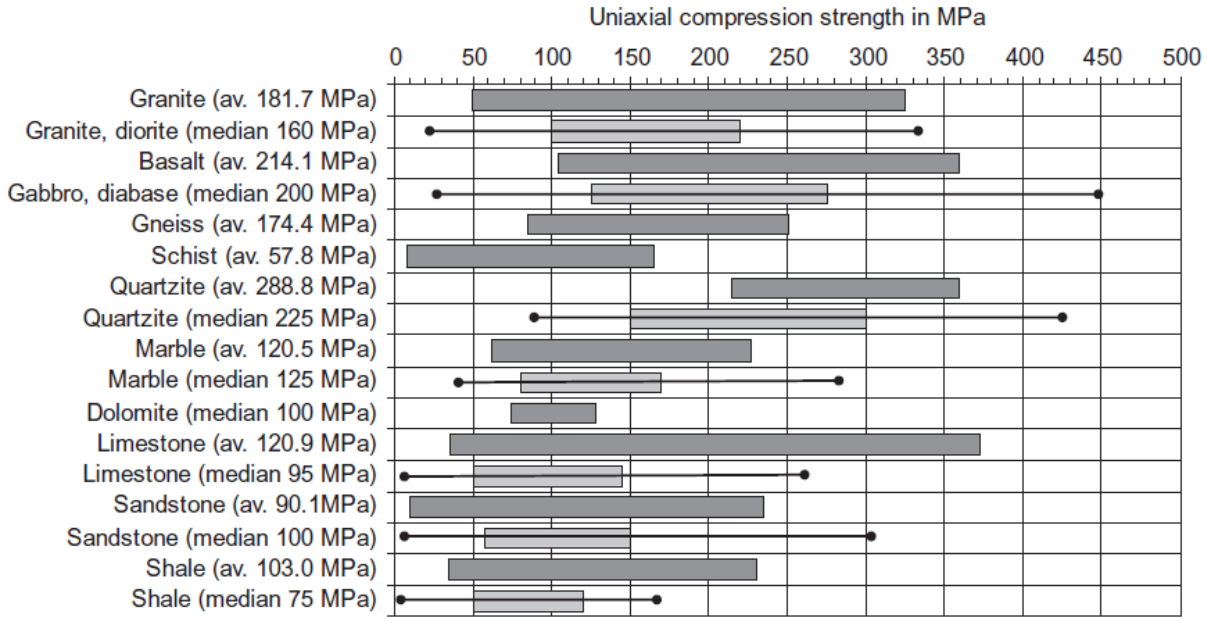

Fig. 5.28 Lithology specific values of uniaxial compressive strength (Schoen, 2004).

The core sample TRAT615 represents the strength of the CET3 zone. The uniaxial compressive strength is defined by a vertical stress without the application of a confining pressure. Therefore σ_3=0 and the Mohr Circle representing the σ_{UCS} starts at the coordinate origin zero. Additionally, the Mohr Circles of the seal and reservoir rock zones are plotted. The horizontal stress is calculated using Eq. 36, were v is the Poisson ratio and σ_v is the vertical stress, overburden pressure or lithostatic pressure (Bjørlykke, 2015).

$$\boldsymbol{\sigma_H = \frac{v}{1-v} * \sigma_v} \qquad \textbf{Eq. 36}$$

The equation assumes that the compaction process in a sedimentary basin can interpreted as a uniaxial strain compaction. This can be assumed because the sediment basin is wide compared to its thickness and the compaction due to additional overburden is interpreted as a one-dimensional deformation. The second assumption is the linear elastic behavior of the grain framework and isotropic behavior of the horizontal stress (Bjørlykke, 2015).

The vertical stress and the Poisson ratio are averaged over the three zone intervals (CET1, 2 and CET3) and inserted into Eq.36. A characteristic horizontal stress is calculated for each zone.

Fig.5.29 shows the Mohr circles of the uniaxial compressive stress and the three Cenomanian zones for the TRAT6 well. The seal rock (CET1) is characterized by a vertical stress (σ_1) of 28.02 MPa and a horizontal stress component(σ_3) of 8.44 MPa. The uppermost reservoir rock (CET2) has a vertical stress (σ_1) of 28.62 MPa and a horizontal stress component(σ_3) of 10.00 MPa. The lower CET3 horizon has a vertical stress (σ_1) of 28.53 MPa and a horizontal stress component(σ_3) of 10.80 MPa

The three zones of the CET1,2 and 3 exhibit a vertical stress which is higher than the measured uniaxial compressive stress. Plotting the Mohr circles, shows that the present horizontal stress allows a higher vertical stress.

The measured uniaxial compressive stresses and the calculated vertical and horizontal stresses of the TRAT7 well are displayed in Fig.5.30. A uniaxial compressive stress of 28.68 MPa is measured and averaged for the CET3. The CET2 has a uniaxial compressive stress of 8.95 and the CET3 has 15.7 MPa. The seal rock (CET1) is characterized by a vertical stress (σ_1) of 27.20 MPa and a horizontal stress component(σ_3) of 9.10 MPa. The uppermost reservoir rock (CET2) has a vertical stress (σ_1) of 27.40 MPa and a horizontal stress component(σ_3) of 9.60 MPa. The lower CET3 horizon has a vertical stress (σ_1) of 27.70 MPa and a horizontal stress component(σ_3) of 10.23 MPa

The measured uniaxial compressive stress of the CET1 is higher than the present vertical stress inside the reservoir section. The UCS values of the CET2 and 3 are lower than the insitu vertical stress.

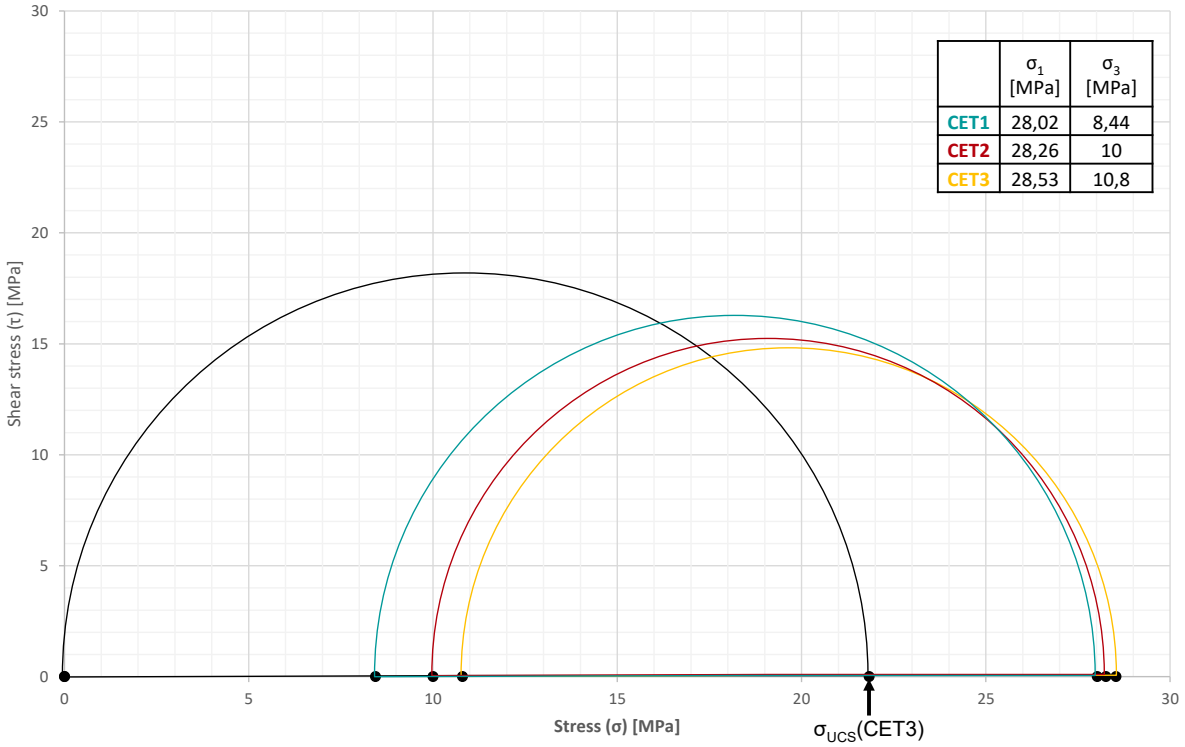

Fig. 5.29 Mohr circle construction for the well TRAT6

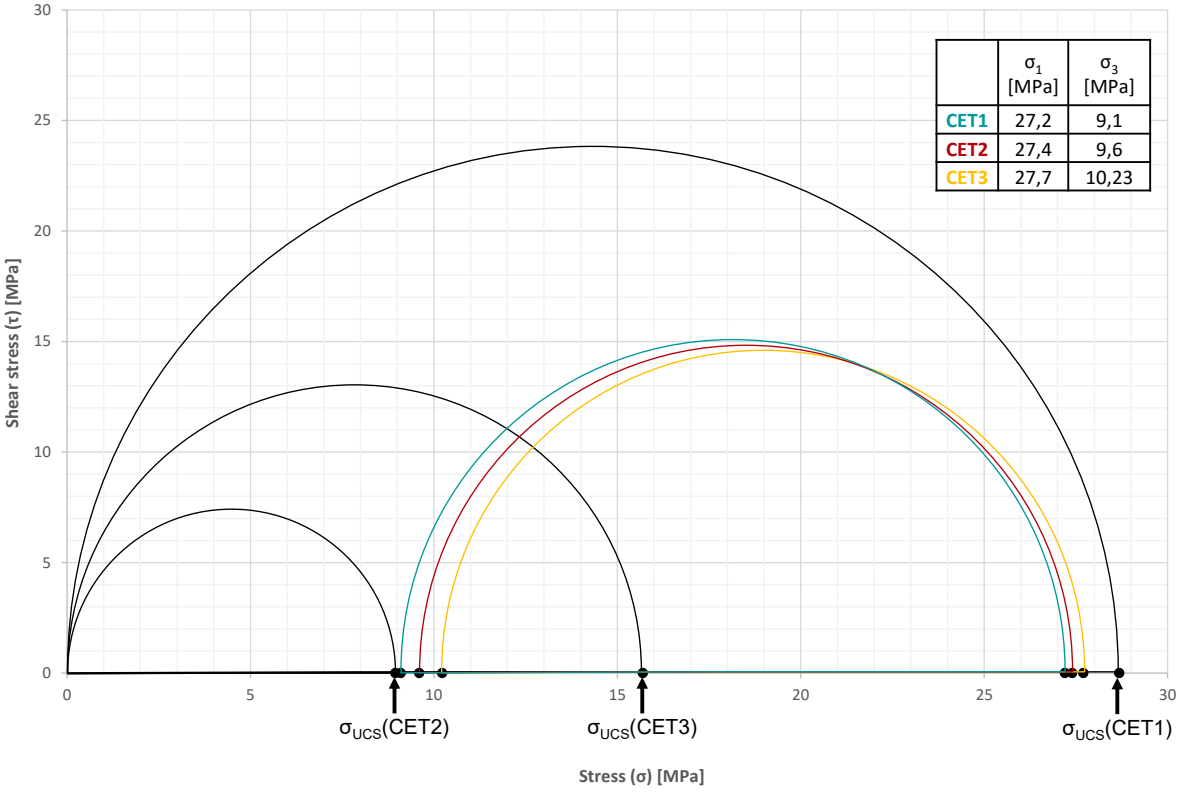

Fig. 5.30 Mohr circle construction for the well TRAT7

5.3 GRID POPULATION

The density, velocity and porosity data are available on a log basis. Upscaling transforms the well log data into a grid property. The upscaling of the well logs assigns the upscaled property values to all grid cells penetrated by the well. The rest of the grid remains empty until it is filled through petrophysical modeling, an interpolation of the upscaled data across the entire study area.

5.3.1 Upscaling

Usually the grid cells are much coarser than the sampling intervals of well logs and it is important to choose an adequate setting for the averaging of well data. This depends mostly on the type of log upscaled. All sonic logs are upscaled using the RMS (Root Mean Squared) averaging, whereas additive properties like porosity and saturation data is upscaled using arithmetic mean. All upscaled logs are treated as lines, meaning that log data values are weighted by the distance between inter-sample mid-points for continuous logs (Schlumberger, 2015).

The following well log measurements are upscaled:

- Compressional velocity (v_p) using RMS
- Shear Velocity (v_s) using RMS
- Density (DEN) using Arithmetic averaging

The result is displayed in Fig. 5.31. The first three columns show the upscaled properties of v_p, v_s and DEN. The coloured data are the upscaled properties, with horizontal lines, marking the grid cells. The original well logs are also plotted, indicating a good fit between original and upscaled data.

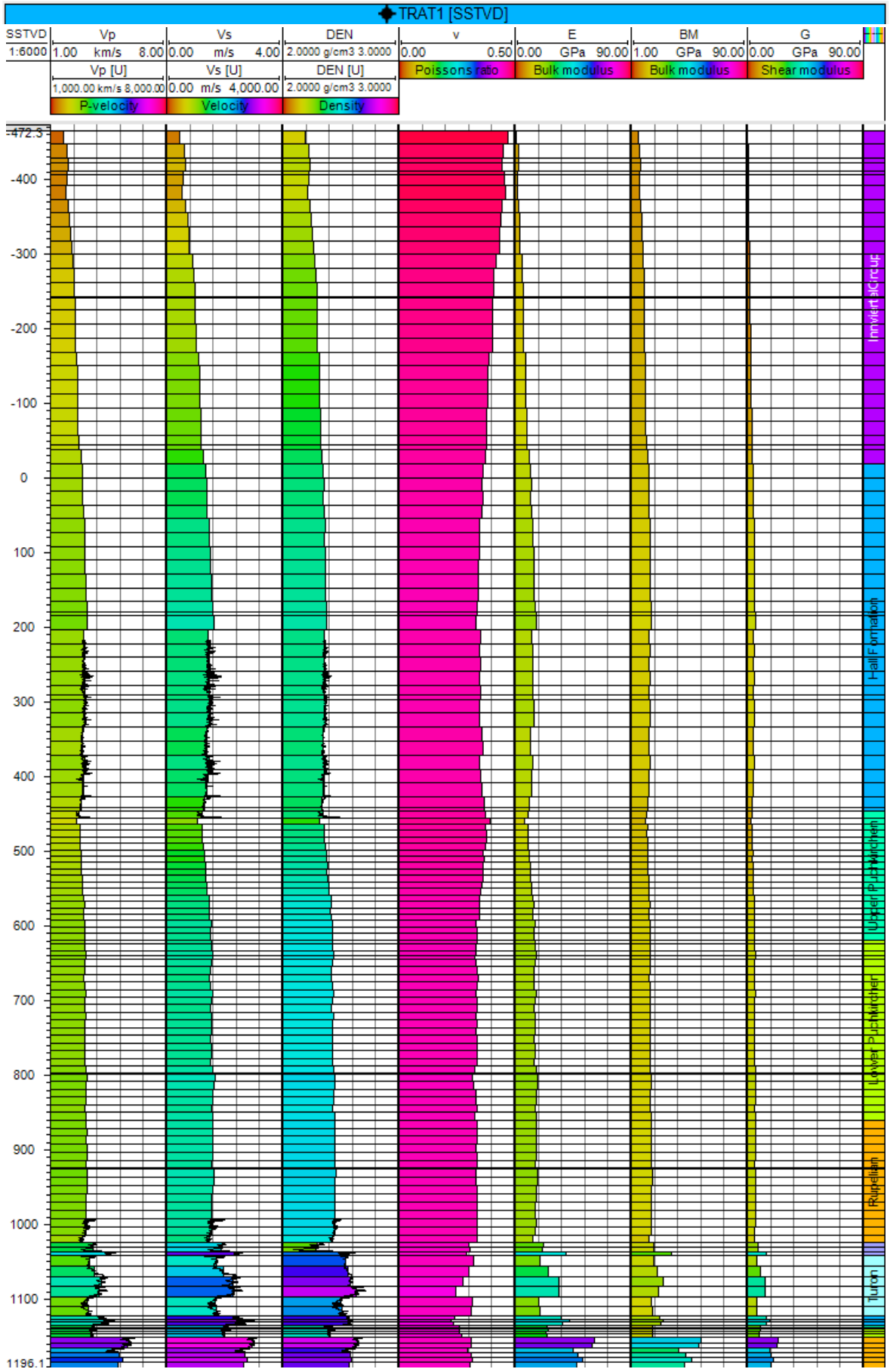

Fig. 5.31 **Upscaled Properties for the well TRAT1.**
From left to right: Young's Modulus E, Poisson's Ratio, Shear Modulus (G) and Bulk Modulus (BM)

5.3.2 Data Analysis

Before filling the rest of the grid by interpolating the upscaled well data, a data analysis is performed. It involves quality control and a spatial trend analysis. Every property needs a fitted variogram for each zone, this ensures a proper spatial variation of the reservoir property when interpolation the data along the wells to the rest of the grid. Fig. 5.32 shows the variogram fitting of compressional wave velocity for the Lower Puchkirchen Formation. The Lower Puchkirchen Formation with a thickness of approximately 250 m allows for a good variogram fitting, because the 250 m are divided into several grid cells and provide a sufficiently large amount of upscaled data points, to perform a good data analysis. Very thin zones, like the Schöneck Formation (Fish Shale) or the three Cenomanian units do not have the required data density to perform a satisfying analysis.

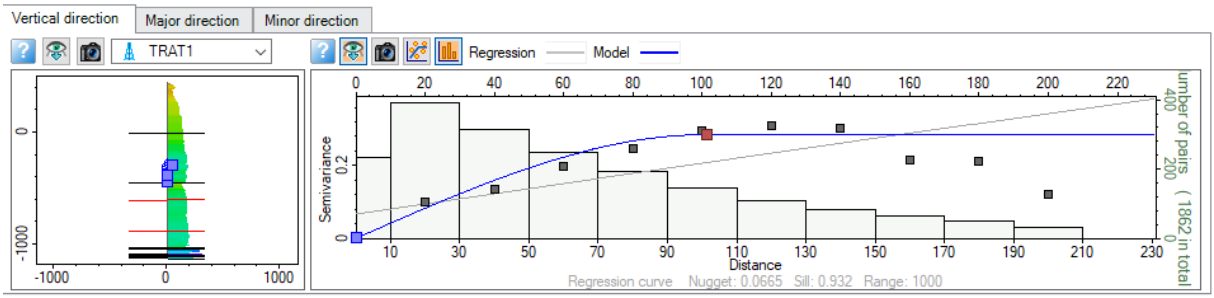

Fig. 5.32 Compressional wave velocity variogram of the Lower Puchkirchen Formation.

5.3.3 Petrophysical Modeling

Petrophysical modeling interpolates the upscaled continuous data along the well paths through the entire grid. All upscaled data is interpolated using Kriging, which results in a smoother interpolation than using Gaussian random function.

Kriging interpolation uses a variogram to calculate the spatial variations (Schlumberger, 2015). Every zone is interpolated separately using the variogram designed during data analysis. Fig. 5.33 shows the interpolated result for the CET2 reservoir zone. The compressional shear velocities (v_p) have an average velocity of 3500 m/s, the mean shear wave velocity (v_s) is 2000 m/s and the average density (DEN) is 2.35 g/m³.

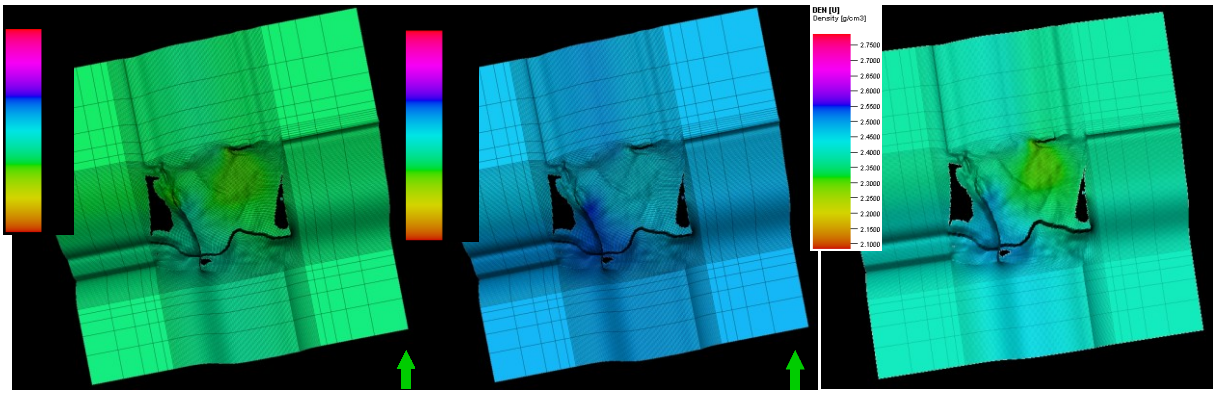

Fig. 5.33 Interpolated data of the CET 2 Zone.
Compressional wave velocity (v_p) with an average velocity of 3500 m/s; Shear wave velocity (v_s) with an average Velocity of 2000 m/s and the modeled density with an average value of 2.35 g/cm³;

After performing the upscaling and petrophysical modeling the grid is filled with the calculated sonic velocity, permeability and density data. This enables the calculation of elastic moduli on a grid property basis, so the upscaling and petrophysical modeling must not be performed for the geomechanical parameters. The Young's modulus (E), Poisson's ratio (υ), shear modulus (μ) and bulk modulus (k) are calculated directly in the grid using Eq. 26- Eq. 29 and the available grid properties of sonic velocities (v_p and v_s) and the density.

Fig. 5.31 shows the calculated grid properties of the elastic parameters along the well of the TRAT1, G stands for the shear modulus and BM for bulk modulus. The distribution of the elastic parameters from the entire geomechanical model is discussed in chapter 5.5.

5.4 GEOMECHANICAL MATERIAL MODELING

The Petrel plug-in "Reservoir Geomechanics" (Schlumberger, 2014) distinguishes between intact rock materials and discontinuity materials, all horizons and zones form intact rock materials, whereas faults are discontinuity materials. Depending on the type of material different properties are required for the material modeling process. See Table 5.6 for all required properties to define an intact rock material and Table 5.7 for discontinuity materials.

5.4.1 Creating intact rock materials

These materials represent the different rock types and consist of a collection of parameters, like Young's modulus, Poisson ratio, bulk and shear modulus etc. which represent the various lithology types. "Reservoir Geomechanics" provides a materials library including sandstone, limestone shale, chalk, siltstone, salt, as well as dense or loose uniform sands and stiff or soft clays (Schlumberger, 2015). After adding a material from the library to the current project all default parameters from Table 5.6, can be adjusted according to the model's needs. To describe the different lithology zones of the model, eight materials are created. Their properties are adjusted according to the calculated parameters during property modeling. The statistic average of Young's, shear and bulk modulus is calculated for each zone and assigned. The same applies for the porosity and density data. The values of the uniaxial compressive strength are either an average of the measured data or literature values (see chapter 5.2.5). The uniaxial compressive strength is determined in MPa, but the software requires bar as an input. The literature and measured data is multiplied with a factor of ten, to convert the unit from MPa to bar.

1. **Limestone (LST), representing the Jurassic zone.**
   It forms the stiffest material with a Young's modulus of 48 GPa, a shear modulus of 18 GPa and a bulk modulus of 42 GPa. The porosity is quite low with 9 % and the density is 2.75 g/cm³. According to literature data 1200 bar is a characteristic uniaxial compressive strength for limestones (see chapter 5.2.5).
2. **Marlstone (MARL), representing the Turonian and Coniancian succession.**
   The material has an average stiffness of 24 GPa, a very low shear modulus of 9.9 GPa and a moderate bulk modulus of 21 GPa. The porosity is quite high with 20 % and the density is the same as for the limestones with 2.52 g/cm³. A uniaxial compressive strength of 1000 bar is assigned, this is a literature value for marlstones (see chapter 5.2.5).

3. **Glauconitic sandstone (GSST), representing the lower Cenomanian zones CET 2 and CET 3.**

   The material is characterized by a Young's modulus of 24 GPa, the shear modulus is almost the same as for marlstone with 10 GPa, but the bulk modulus is lower (17 GPa). The average porosity is 22 % and the density 2.34 g/cm³. The uniaxial compressive strength of the glauconit sandstone was measured in laboratory and a value of 105 bar is assigned to this rock material.

4. **Cemented glauconitic sandstone (CGSST), representing the upper Cenomanian zone CET 1.**

   The high amount of cement makes this material much stiffer compared to the glauconitic sandstone. A Young's modulus of 36 GPa, a bulk modulus of 23.3 GPa and the shear modulus is 14.4 GPa are assigned. Only the limestone will deform less. The cement reduced the porosity to 12 % and increased the density to 2.56 %. The uniaxial compressive strength for the cemented glauconitic sandstone is 216 bar, the rock strength was measured in laboratory.

5. **Sandy Limestone (Sandy LST), representing the Eocene zone;**

   The Eocene sandstone is not present in all wells, zero thickness is no option in geomechanical gridding, and therefore the Lithothamnium Limestone and Eocene sandstone are summarized as sandy limestone. The third most stable material with a Young's modulus of 30 GPa, bulk modulus of 25 GPa and a shear modulus of 12 GPa. The porosity and density are varying, but form an average of 35 % and 2.63 g/cm³. A uniaxial compressive strength of 1000 bar is assigned, according to literature data this is a suitable value for sandy limestones (see chapter 5.2.5).

6. **Shale, representing the Rupelian zone and Hall Formation;**

   Shale is a very soft material, which deforms easily. It is characterized by a Young's modulus of 16 GPa, a bulk modulus of 16.5 and a shear modulus of 6.4 GPa. The density is 2.35 g/cm³ and the porosity 20 %. According to literature data, shales have an approximate uniaxial compressive strength of 750 bar (see chapter 5.2.5).

7. **Gravity Flow, characteristic for the Puchkirchen series;**

   Its properties result in a slightly softer material than shale. With a Young's modulus of 15 GPa, bulk modulus of 15 GPa and a shear modulus of 5.5 GPa. Density is with 2.42 g/cm³ the same as for shale, but the average porosity is higher with 30 %. This rock material represents a mixture of sandstone and shales, as both of these rock materials have a uniaxial compressive strength of 750 bar, the same value is assigned to gravity flows.

8. **Sandstone (SST), for the Innviertel Group.**
   The softest material due to small burial depth. An average Young's modulus of 6 GPa, bulk modulus of 11 GPa and the lowest shear modulus of 2.2 GPa. Characterized by a density of 2.28 g/cm³ and a high porosity of 45 %. A uniaxial compressive strength of 750 bar is assigned, this is an averaged literature value (see chapter 5.2.5).

The predefined isotropic elasticity model and a deformation according through Mohr-Coulombs yield criteria is chosen from the material library for all materials. The definition of yield criteria is optional, whereas the selection of an elasticity model is mandatory (Schlumberger, 2015). These materials represent characteristic regions or entire zones, to which they are assigned during the population process. Later the properties can be overwritten by the petrophysical modelled properties.

An overview of all relevant material parameters is given in Table 5.6. The data is a combination of calculated averages for the individual zones, literature values and predefines default values by the software (Schlumberger, 2014).

- The calculated data includes Youngs modulus [GPa], Poisson's ratio [-], bulk density [g/cm³], shear modulus [-], bulk modulus k [GPa], porosity [m³/m³] and the unconfined compressive strength [bar] for the GSST and CGSST;
- The literature data includes the unconfined compressive strength [bar] for the LST, MARL, sandy LST, SHALE, SST and gravity flow materials
- The software's default values include the Biot's elastic constant [GPa], the linear thermal coefficient [1/k], the friction angle [deg], the dilatation angle [deg], the tensile stress cut off [bar] and the hardening/softening coefficient [-].

Property		Intact Rock Materials							
		LST	MARL	GSST	CGSST	Sandy LST	SHALE	SST	Gravity Flow
		Jurassic zone	Turon Coniacian	CET2&3	CET1	Eocene zone	Rupelian Hall Form.	Innviertel Group	Puchkirchen Series
Youngs Modulus E	[GPa]	48.00	25.00	24.00	36.00	30.00	16.00	6.00	15.00
Poisson's Ratio v	[-]	0.31	0.27	0.26	0.24	0.30	0.33	0.41	0.34
Bulk Density RHOB	[g/cm³]	2.75	2.52	2.34	2.56	2.63	2.35	2.28	2.42
Shear Modulus μ	[-]	18.00	9.90	10.00	14.40	12.00	6.40	2.00	5.50
Bulk Modulus k	[GPa]	42.00	21.00	17.00	23.30	25.00	16.50	11.00	15.00
Biot's Elastic Const. α	[GPa]	1.00	1.00	1.00	1.00	1.00	1.00	1.00	1.00
Porosity	[m³/m³]	0.09	0.20	0.22	0.12	0.35	0.20	0.45	0.30
Linear Thermal Coefficient	[1/k]	1.3^-5	1.3^-5	1.3^-5	1.3^-5	1.3^-5	1.3^-5	1.3^-5	1.3^-5
Unconfined Compression Strength	[bar]	1200	1000	105	216	1000	750	750	750
Friction angle	[deg]	38.50	38.50	34.90	20.00	38.50	14.40	14.40	14.40
Dilatation angle	[deg]	19.25	19.25	17.45	10.00	19.25	7.20	7.20	7.20
Tensile Stress Cut off	[bar]	140	140	75	60	140	60	60	60
Hardening / Softening Coefficient	[-]	0.00	0.00	0.00	0.00	0.00	0.00	0.00	0.00

Table 5.6 Properties for creating intact rock materials.

5.4.2 Creating discontinuity materials

Discontinuity materials describe faults and fractures. Properties include parameters which define stiffness, strength and spacing. Due to the lack of laboratory data and strength measurements, default values from the material library are assigned to faults during the "populate properties" process. The material library contains two different discontinuity materials, one defines a default fault and the other a default fracture, the parameters describing those two materials are shown in Table 5.7.

Property	Unit	Discontinuity Material	
		Fault	Fractures
Fault normal stiffness	**[bar/m]**	40000	800000
Fault shear stiffness	**[bar/m]**	15000	400000
Cohesion	**[bar]**	0.01	0.01
Friction angle	**[deg]**	20	20
Dilatation angle	**[deg]**	10	10
Tensile strength	**[bar]**	0.01	0.01
Fracture Spacing	**[m]**	-	5
Initial Opening	**[-]**	0	0

Table 5.7 Properties for creating discontinuity materials.

5.5 POPULATE PROPERTIES

The geomechanic grid is populated with predefined materials, created during material modeling. Populating the properties can be done in three different ways. Either by assigning a material to an embedded area, like sideburden, overburden or underburden. The second option is by defining an area based on a specific coordinate system the I-J-K index and the last option is by assigning materials to specific zones (Schlumberger, 2015).

The geomechanical grid is populated by assigning the defined intact rock materials, like Glauconitic sandstone, Sandstone, Marl, Limestone and Shale, to the different zones created during pillar gridding.

After assigning the material to a zone the material parameters can be changed using "*override material properties"* (Schlumberger, 2015). Using this allows to replace the single value defined during intact rock material modeling, by assigning a model property, like the upscaled and petrophysically modelled Young's modulus. This results in a more detailed population, including the vertical a horizontal variations of geomechanical parameters within a zone (see Fig.5.34 – 5.39).

Nine regions including their sideburdens are created

1. Sandstone / Innviertel Group
2. Shale / Hall Formation
3. Gravity Flow / Puchkirchen Series
4. Shale / Rupelian and Fish Shale
5. Shaly Limestone / Eocene
6. Marl / Coniacian and Turonian
7. Cemented glauconitic sandstone / CET1
8. Glauconitic sandstone / CET 2 and CET 3
9. Limestone / Jurassic and underburden

These regions are populated with the defined materials created during material modeling (chapter 5.4.1). To replace the single values of the material properties, like the a Young's modulus of 24 GPa for the entire zone of the Glauconitic sandstone, a *override material properties* is performed. This is done for the Young's modulus, Poisson's ratio, porosity and bulk density. All the single values defined during material modeling are replaced by the calculated grid properties for all regions.

Fig. 5.34 shows the elastic moduli along a north-south profile. The Aistersheim and Gaspoldshofen faults are visible, as well as the anticlinal dome. The molasse sediments of the Innviertel Group, Hall Formation and Puchkirchen Formation have a relative uniform distribution of elastic moduli. The stiffest zone, the pink layer above the anticlinal dome, is the Eocene limestone with a Young's modulus up to 80 GPa.

A detailed section of the anticlinal dome, next to the Aistersheim fault and the reservoir zone is displayed in Fig.5.35. The bulk modulus is highest on top of the Jurassic zone with a bulk modulus of approximately 80 GPa.

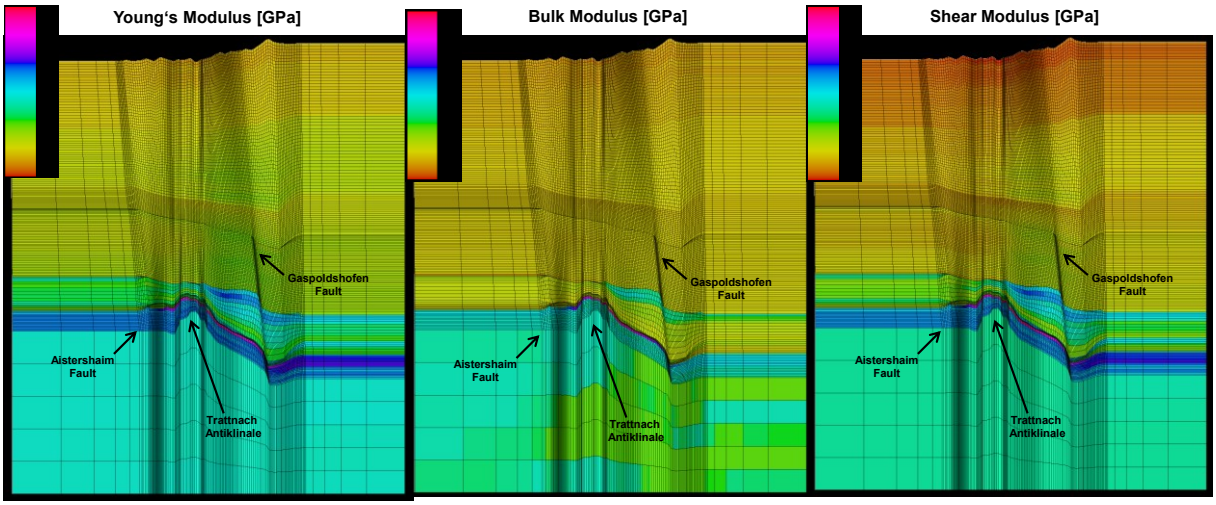

Fig. 5.34 N-S profile of the Geomechanical model.

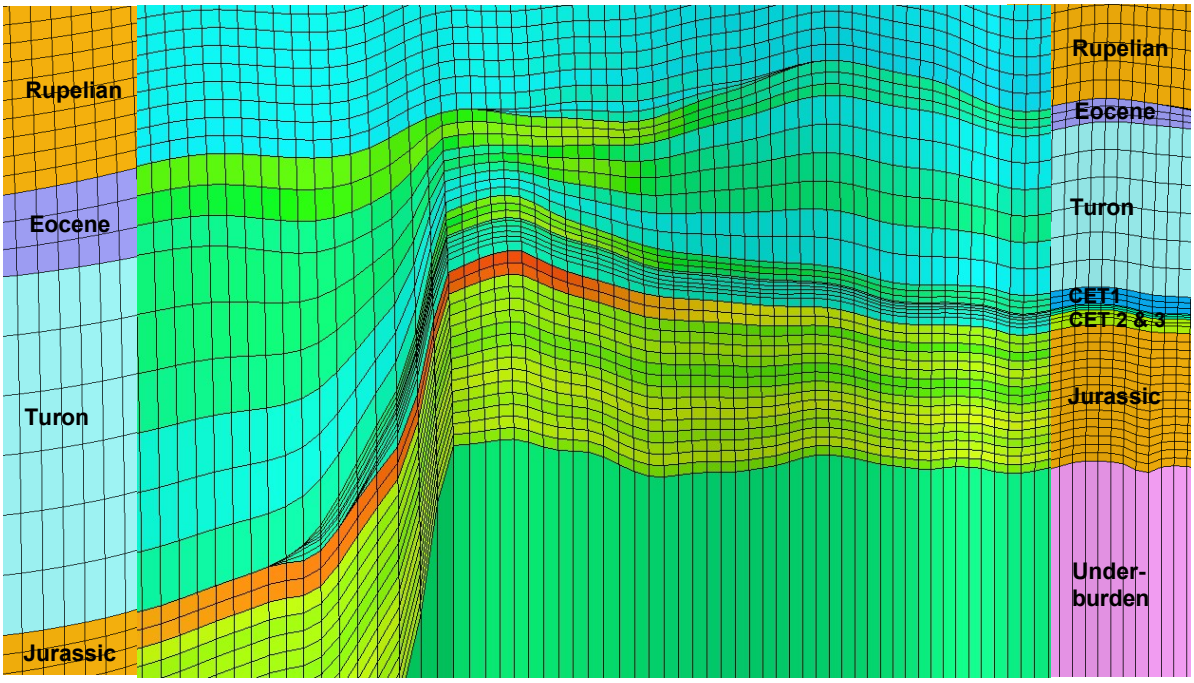

Fig. 5.35 Detailed reservoirs section of the N-S profile

Fig. 5.36 shows the distribution of Young's, bulk and shear modulus along a west – east profile. The Schwanenstadt fault marks the western boundary of the reservoir zone. Horizontal and vertical variations within a region are not very prominent.

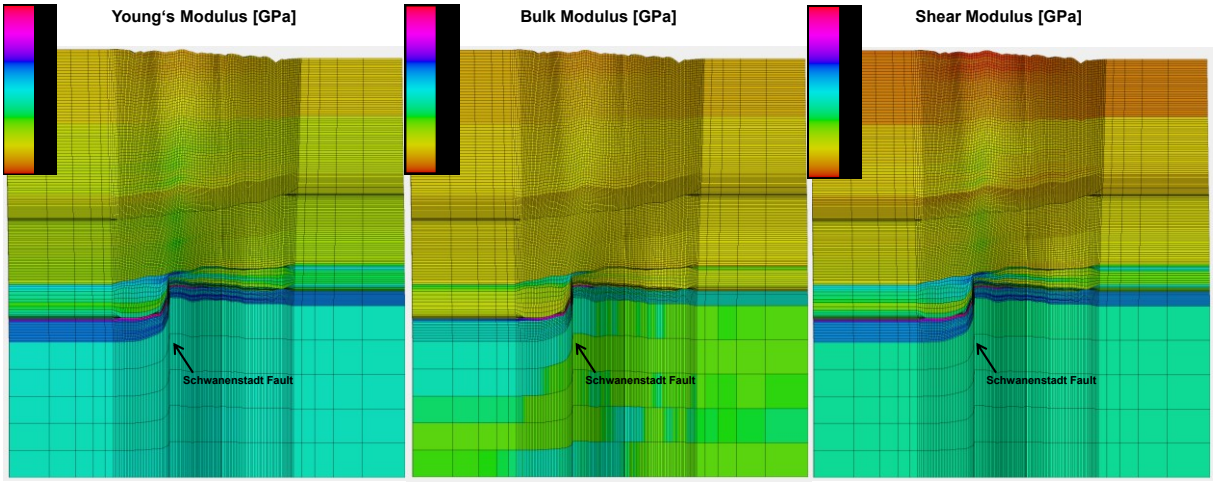

Fig. 5.36 W-E profile of the Geomechanical model.

The horizontal variation of the bulk modulus along the Top of the Jurassic zone is displayed in Fig.5.37. The highest values, up to 80 GPa, occur below the anticlinal dome, were the oil reservoirs are located. A zone of lower values for the bulk modulus is present at the northern part of the model. The variation of the bulk modulus correlates with variations of bulk densities.

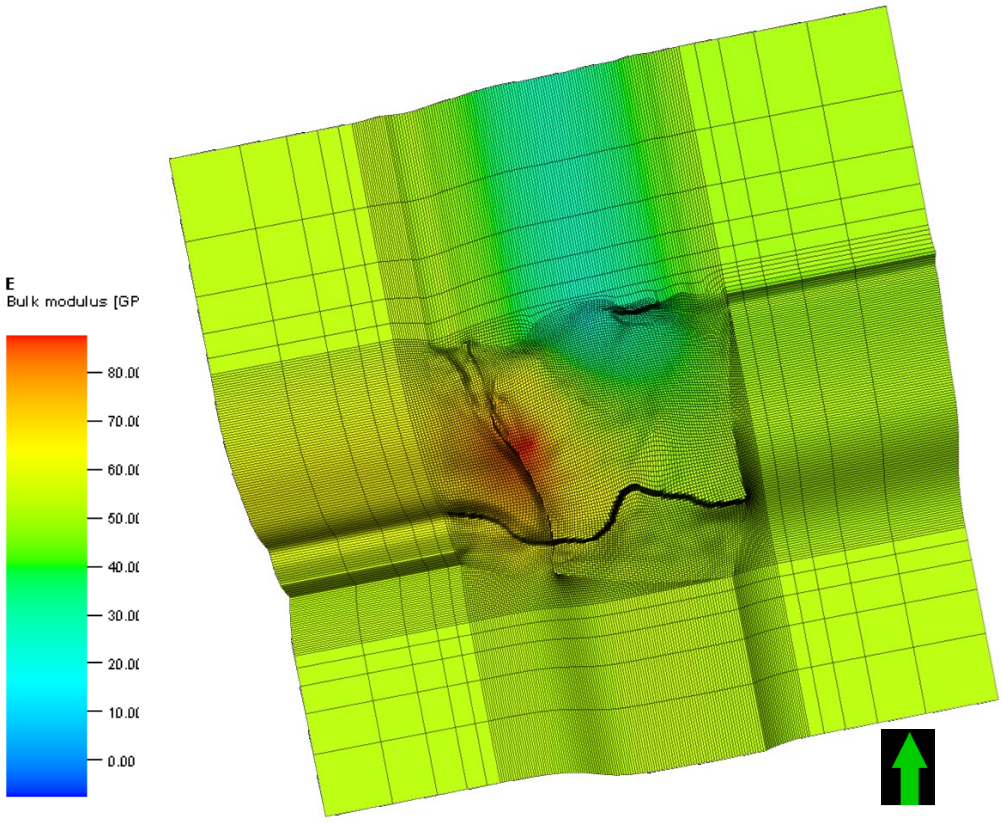

Fig. 5.37 Horizontal variation of Young's modulus along the Top Jurassic.

The horizon slice along the top of the reservoir horizon CET2 shows a more uniform bulk modulus distribution than along the Jurassic horizon. The bulk modulus is in general very low with an average value of 21 GPa. A slight increase of the bulk modulus is noticeable close to the major Schwanenstadt and Gaspoldshofen fault.

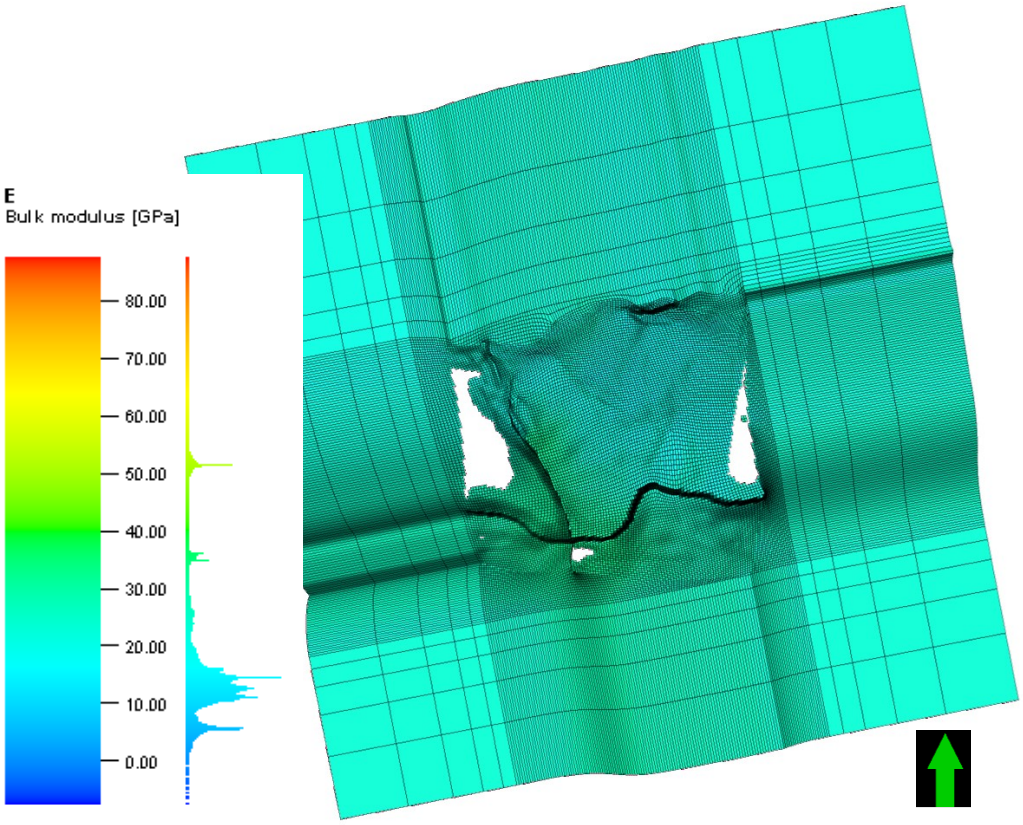

Fig. 5.38 Horizontal variation of Young's modulus along the Top CET2 horizon.

The variation of the bulk modulus along the top of the sealing CET1 formation is displayed in Fig.5.39. The bulk modulus is slightly more varying than on top of the CET2 horizon and the average bulk modulus is in between the Jurassic an CET2 values, with approximately 36 GPa.

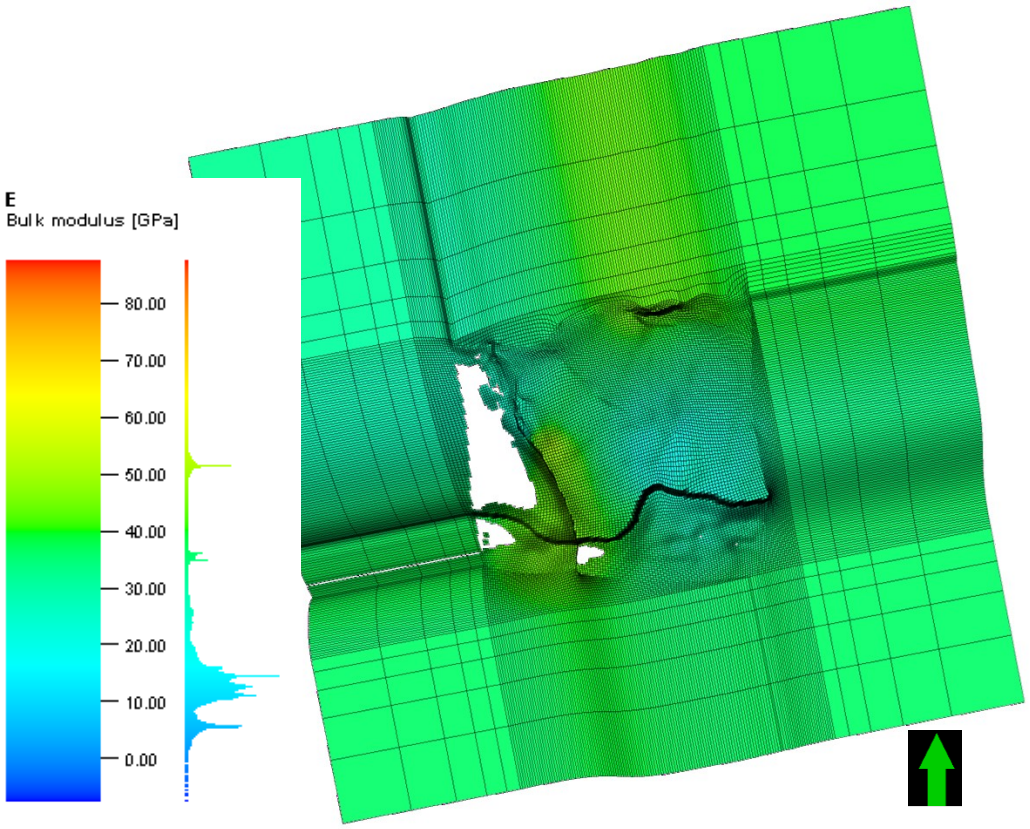

Fig. 5.39 Horizontal variation of Young's modulus along the Top CET1 horizon.

6 CONCLUSION

This study aims to model and calculate all properties for the interpretation of the geomechanical behaviour of the Trattnach area. The thesis can be divided into three main tasks:

- The calculation of all relevant petrophysical data. Density, porosity and shear sonic velocity calculations based on petrophysical relationships have been performed. The density, porosity and sonic velocities form the foundation for the calculation of all geomechanical parameters including Young's modulus, Bulk modulus and Poisson's ratio. A series of uniaxial compressive test were performed to determine the uniaxial compressive strength of rock samples from the reservoir section.
- The setup of a geological model in Petrel. An existing reservoir model, covering the area of the Cenomanian sandstones has been extended up to earth's surface. The new model now covers an area of 26 km² and includes the entire basin evolution from Jurassic sandstones up to the Innviertel Group.
- The conversion of the geological model into a geomechanical model has been undergone. This includes the creation of a geomechanical grid which has been filled with all relevant elastic properties and intact rock materials.

With these tasks performed the property model is complete. The model shows that the Jurassic limestone is the most stable formation with a averaged Young's modulus of 48 GPa. These are followed by the sealing CET1 formation, with 36 GPa. Another stable zone is built by the Eocene lime- and sandstones with a averaged Young's modulus of 30 GPa. The reservoir rocks formed by the CET2 and CET3 zone have a Young's modulus of 30 GPa. The Young's modulus of the zones from the Innviertel Group down to the Rupelian shales increases steadily with increasing overburden.

This model can now act as the foundation for a geomechanical simulation. When a complete reservoir simulation is available, a geomechanical simulation, using the in Petrel implemented VISAGE simulator, can be performed. Unfortunately the provided reservoir simulation existing, is not sufficient and a geomechanical simulation cannot be performed at this point. Nevertheless the foundation for starting such a simulation including a working grid and all properties necessary have been made.

7 LIST OF FIGURES

Fig. 2.1 Schematic Stress Tensor in 2D and 3D. 10

Fig. 2.2 Types of strain. 11

Fig. 2.3 Elastic deformation caused by shear waves (after Kearey et al., 2002). 14

Fig. 2.4 Elastic deformation caused by compressional waves (after Kearey et al., 2002). 14

Fig. 2.5 Principal Coordinate System. 15

Fig. 2.6 Schematic Normal Fault. 16

Fig. 2.7 Schematic Strike Slip Fault. 17

Fig. 2.8 Schematic Reverse Fault. 17

Fig. 2.9 Triaxial Test and Mohr Circle Construction. 18

Fig. 2.10 Triaxial Test / Stress – Strain Diagram (Zoback, 2014). 19

Fig. 2.11 Mohr Failure criteria for different faulting regimes (after Zoback, 2014). 20

Fig. 2.12 Three ways to calculate elastic moduli from an axial strain-stress curve (black). 21

Fig. 2.13 Pore Pressure Measurements (Zoback, 2014). 23

Fig. 2.14 Digital Elevation Model of central Europe. 24

Fig. 2.15 Generalized Cross Section through the Austrian Molasse basin. 25

Fig. 2.16 The Mesozoic evolution of the Austrian Molasse Basin (Gross et al., 2015). 27

Fig. 2.17 Cenozoic Evolution of the Austrian Molasse Basin (Gross et al., 2015). 28

Fig. 2.18 Production History of the Trattnach oil field. 30

Fig. 2.19 Fault Systems in Upper Austria. 31

Fig. 2.20 Depth map of the CET2 horizon. 32

Fig. 2.21 Core Measurements of the Cenomanian Sandstone. 33

Fig. 2.22 Well log measurements of the Cenomanian Sandstone. 34

Fig. 3.1 Differences of RAG's fault models. 37

Fig. 4.1 Study area of the Trattnach Oil Field. 38

Fig. 4.2 Seismic Sections of the study area. 41

Fig. 4.3 Grid Slice, final zonation and layering. 43

Fig. 5.1 Quality Control of the geomechanical gridding process. 46

Fig. 5.2 2D View of fault models. 47

Fig. 5.3 Thickness map Coniacian. 48
Fig. 5.4 Topview of the geomechanical grid. 49
Fig. 5.5 Side view of the geomechanical grid. 49
Fig. 5.6 Empirical Relationship between v_p and RHOB from TRAT11. 51
Fig. 5.7 Empirical Relationship between v_p and RHOB from TRAT12. 52
Fig. 5.8 Calculated density logs based on Gardner´s Equation (Gardner et al., 1974). 54
Fig. 5.9 Pressure gradients for the Trattnach field. 55
Fig. 5.10 Velocity – porosity trend for Cenomanian reservoir sandstones. 56
Fig. 5.11 Quality control of the calculated porosity logs. 58
Fig. 5.12 Calculated porosity logs based on Wyllie's time-average equation. 59
Fig. 5.13 Porosity – depth trend for the Trattnach area. 61
Fig. 5.14 Calculated shear sonic logs. 64
Fig. 5.15 Calculated Young's modulus. 66
Fig. 5.16 V_p versus porosity plot with a lower Reuss and an upper Voigt bound. 67
Fig. 5.17 Velocity versus porosity plot for the Cenoman and the Hall Formation. 68
Fig. 5.18 Calculated bulk modulus. 70
Fig. 5.19 Test Results TRAT701B. 73
Fig. 5.20 Test Results TRAT704A. 74
Fig. 5.21 Test Results TRAT705. 75
Fig. 5.22 Test Results TRAT709. 76
Fig. 5.23 Test Results TRAT712A. 77
Fig. 5.24 Test Results TRAT714A. 78
Fig. 5.25 Test Results TRAT714B. 79
Fig. 5.26 Test Results TRAT718. 80
Fig. 5.27 Test Results TRAT615. 81
Fig. 5.28 Lithology specific values of uniaxial compressive strength (Schoen, 2004). 83
Fig. 5.29 Mohr circle construction for the well TRAT6 85
Fig. 5.30 Mohr circle construction for the well TRAT7 85
Fig. 5.31 Upscaled Properties for the well TRAT1. 87
Fig. 5.32 Compressional wave velocity variogram of the Lower Puchkirchen Formation. 88

Fig. 5.33 Interpolated data of the CET 2 Zone. 89

Fig. 5.34 N-S profile of the Geomechanical model. 96

Fig. 5.35 Detailed reservoirs section of the N-S profile 96

Fig. 5.36 W-E profile of the Geomechanical model. 97

Fig. 5.37 Horizontal variation of Young's modulus along the Top Jurassic. 97

Fig. 5.38 Horizontal variation of Young's modulus along the Top CET2 horizon. 98

Fig. 5.39 Horizontal variation of Young's modulus along the Top CET1 horizon. 99

8 LIST OF ACRONYMS AND ABBREVIATIONS

K	Bulk modulus
K_{ma}	Bulk modulus of the matrix
K_{fl}	Bulk modulus of the fluid
K_v	Bulk modulus Voigt
K_R	Bulk modulus Reuss
K_{VRH}	Bulk modulus Voigt Reuss Hill
K_+^{HS}	Upper bulk modulus Hashin-Shtrikman
K_-^{HS}	Lower bulk modulus Hashin-Shtrikman
C_l	Clay Index
C_p	Lack of compaction correction factor
$\Delta t_{p,ma}$	Compressional slowness of the matrix material
Δt_{fl}	Compressional slowness of the pore fluid
Δt_p	Compressional wave slowness of the porous rock
Δt_{shale}	Transit slowness of shale
v_p	Compressional wave velocity
v_s	Shear wave velocity
v_s	Shear wave velocity
V_{cl}	Volume clay
V_{qz}	Volume quartz
ρ	Density
z	Depth
c_{ij}	Elasticity tensor
α	Framework grain stability factor for clean sandstones
A	Initial porosity at zero depth
λ	Lame's Constant; axial modulus
g	Acceleration due to gravity
S_{Hmax}	Maximum principal horizontal stress
τ_f	Maximum shear stress
S_{hmin}	Minimum principal horizontal stress
σ_N	Normal stress

S_v	Overburden Stress; vertical Stress
ν	Poisson's Ratio
P_p	Pore Pressure
ϕ	Porosity
ϕ_w	Time-average porosity
ϕ_c	Corrected porosity
σ_1	Vertical stress
σ_v	Vertical stress
σ_v'	Effective vertical stress
σ_3	Horizontal stress
β	Sensitivity factor towards increasing clay index
μ	Shear modulus; Modulus of rigidity
μ_{ma}	Shear modulus of the fluid
τ	Shear Stress
ε	Strain
σ	Stress
E	Young's Modulus
E_T	Tangent modulus
E_S	Secant modulus
E_I	Initial modulus
a	Empirical constant
b	Empirical constant
Δl	Change of length
l_0	Original length
F	Force
h	Height
d	Diameter

9 REFERENCES

Anderson, E. M. (1951). *The Dynamics of Faulting and Dyke Formation with Applications to Britain.* Edinburgh: Oliver and Boyd.

Andeweg, B., & Cloetingh, S. (1998). Flexure and 'unflexure' of the North Alpine German-Austrian Molasse Basin: constraints from forward tectonic modelling. In A. Mascle, C. Puigdefabregas, H. P. Luterbacher, & M. Fernandez, *Cenozoic Foreland Basins of Western Europe*, pp. 403-422. Geological Society Special Publications 134.

Avseth, P. T., & Mavko, M. G. (2005). *Quantitative Seismic Interpretation, Applying Rock Physics Tools to Reduce Interpretation Risk.* New York: Cambridge University Press.

Bjørlykke, K. (2015). *Petroleum Geoscience: From Sedimentary Environments ro Rock Physics.* Heidelberg: Springer-Verlag Berlin.

Brady, B., & Brown, E. T. (1999). *Rock Mechanics for Underground Mining.* Dordrecht, The Netherlands: Kluwer Academic Publishers.

Castagna, J. P. (1993). Amplitude-versus-offset analysis; tutorial and review. In J. P. Castagna, & M. M. Backus, *Offset-Dependent Reflectivity—Theory and Practice of AVO Analysis.* Tulsa Oklahoma, USA: Society of Exploration Geophysicists.

Castagna, J. P., Batzle, M. L., & Eastwood, R. L. (1985). Relationships between compressional-wave and shear-wave velocities in clastic silicate rocks. *Geophysics*, pp. 571-581.

De Ruig, M. (2003). Deep Marine Sedimentation and Gas Reservoir Distribution in Upper Austria. *OIL GAS European Magazine, 2*.

De Ruig, M. J., & Hubbard, S. M. (2006). Seismic facies and reservoir characteristics of a deep-marine channel belt in the Molasse foreland basin, Puchkirchen Formation, Austria. *AAPG Bulletin, 90*(5), pp. 735-752.

Dusseault, M B. (2011). Geomechanic Challenges in Petroleum Exploitation. KSCE *Journal of Civil Engineering* 15(4), pp. 669-678.

Fjar, E., Holt, R. M., Raaen, A. M., Risnes, R., & Horsrud, P. (2008). *Petroleum Related Rock Mechanics* (Vol. Volume 53). Elsevier Science.

Gardner, G. H., Gardner, L. W., & Gregory, A. R. (1974). Formation velocity and density - The diagnostic basics for stratigraphy traps. *Geophysics, 6*, pp. 770-780.

Gratzer, R., Bechtel, A., Sachsenhofer, R. F., Linzer, H.-G., Reischenbacher, D., & Schulz, H.-M. (2011). Oil-oil and oil-source rock correlations in the Alpine Foreland Basin of Austria: Insights from biomarker and stable carbon isotope studies. *Marine and Petroleum Geology*, pp. 1171-1186.

Gross, D., Sachsenhofer , R., Rech, A., Sageder, S., Geissler, M., Schnitzer, S., & Troiss, W. (2015). The Trattnach Oil Field in the North Alpine Foreland Basin (Austria). *Austrian Journal of Earth Sciences*(108/2), pp. 151-171.

Gross, D., Sachsenhofer, R. F., Bechtel, A., Gratzer, R., Grundtner, M.-L., Linzer, H.-G., Scheucher, L. (2018). Petroleum Systems in the austrian sector of the North Alpine Foreland Basin: An Overview. *Journal of Petroleum Geology*, pp. 299-318.

Gusterhuber, J., Dunkl, I., Hinsch, R., Linzer, H., & Sachsenhofer, R. (2012). Neogene uplift and erosion in the Alpine Foreland Basin (Upper Austria and Salzburg). *Geologica Carpatica, 63*(4), pp. 298-305.

Gusterhuber, J., Hinsch, R., Linzer, H.-G., & Sachsenhofer, R. F. (2013). Hydrocarbon generation and migration from sub-thrust source rocks to foreland reservoirs: The Austrian Molasse Basin. *Austrian Journal of Earth Sciences*(106/2), pp. 115-136.

Han, D., Nur, A., & Morgan, D. (1986). Effects of porosity and clay content on wave velocities in sandstones. *Geophysics, 11*, pp. 2093-2107.

Hashin, Z., & Shtrikman, S. (1963). A variational approach to the theory of the elastic behaviour of multiphase materials. *Journal of the Mechanics and Physics of Solids*(Issue 2), pp. 127-140.

Hill, R. (1952). The elastic behaviour of a crystalline aggregate. *Proceedings of the Physical Society, Section A*(Issue 5), pp. 349-354.

Jaeger, J. C., & Cook, N. G. (1979). *Fundamentals of Rock mechanics* (2nd Edition ed.). New York: Chapman and Hall.

Kearey, P., Brooks, M., & Hill, I. (2002). *An Introduction to Geophysical Exploration.* Oxford: Blackwell Science Ltd.

Kuhlemann, J., & Kempf, O. (2002). Post-Eocene evolution of the North Alpine Foreland Basin and its response to Alpine tectonics. *Sedimantary Geology, 152*, pp. 45-78.

Mavko, G., Mukerji, T., & Dvorkin, J. (1998). *The Rock Physics Handbook.* New York: Cambridge University Press.

Nachtmann, W. (1995). Bruchstrukturen und ihre Bedeutung für die Bildung von Kohlenwasserstoff-fallen in der oberösterreichischen Molasse. *Geologische Paläontologische Mitteilungen, 20*, pp. 221-230.

Nachtmann, W., & Wagner, L. (1987). Mesozoic and Early Tertiary evolution of the Alpine foreland in Upper Austria and Salzburg, Austria. *Tectoniphysics, 137*, pp. 61-76.

Ramm, M., & Bjorlykke, K. (1994). Porosity/depth trends in reservoir sandstones: assessing the quantitative effects of varying pore-pressure, temperature history and mineralogy, Norwegian Shelf data. *Clay Mineralogy, 29*, pp. 475-490.

Raymer, L. L., Hunt, E. R., & Gardner, J. S. (1980). An improved sonic transit time-to-porosity transform. (S. P. (SPWLA), Ed.) *Soc. Professional Well Log Analysis (SPWLA) 21st Annual Logging Symposium*.

Reuss, A. (1929). Berechnung der Fließgrenze von Mischkristallen auf Grund der Plastizitätsbedingung für Einkristalle. *Zeitschrift für Angewandte Mathematik und Mechanik, 9*.

Rider, M., & Kennedy, M. (2011). *The Geological Interpretation of Well Logs.* Scotland: Rider-French Consulting Ltd.

Sachsenhofer, R. F., Leitner, B., Linzer, H., Bechtel, A., Coric, S., Gratzer, R., . . . Soliman, A. (2010). Deposition, Erosion and Hydrocarbon Source Potential of the Oligocene Eggerding Formation (Molasse Basin, Austria). *Austrian Journal of Earth Science, 103/1*, pp. 76-99.

Schlumberger. (2014). Petrel Reservoir Geomechanics - An integrated environment for 3D and 4D geomechanics modeling and simulations. software.slb.com/Petrel.

Schlumberger. (2015). Software Manual of the Petrel E&P Software Platform 2015.3. 2015.

Schoen, J. (2004). Physical Properties of Rocks: Fundamentals and Principles of Petrophysics. Elsevier.

Schulz, H., Sachsenhofer, R. F., Bechtel, A., Polesny, H., & Wagner, L. (2002). The origin of hydrocarbon source rocks in the Austrian Molasse Basin (Eocene–Oligocene transition). *Marine and Petroleum Geology, 19*, pp. 683-709.

Sissingh, W. (1997). Tectonostratigraphy of the North Alpine Foreland Basin: correlation of Tertiary depositional cycles and orogenic phases. *Tectonophysics, 282*, pp. 223-256.

Steininger, F. F., & Wessely, G. (1999). From the Tethyan Ocean to the Paratethys Sea: Oligocene to Neogene Stratigraphy, Paleogeography and Paleobiogeography of the circum-Mediterranean region and the Oligocene to Neogene Basin evolution in Austria . *Mitt. Österr. Geol. Ges.*, pp. 95-116.

Terzaghi, K. (1925). *Erdbaumechanik auf Bodenphysikalischer Grundlage.* Leipzig-Vienna: Franz Deuticke.

Tipler, P A. 1991. Physics for Scientists and Engineers. New York : Wortg Publishers Inc., 1991.

Voigt, W. (1910). *Lehrbuch der Kristallphysik.* Leipzig: Teubner-Verlag.

Wagner, L. R. (1996). Stratigraphy and hydrocarbons in the Upper Austrian Molasse Foredeep (active margin). *In: WESSELY, G. & LIEBL, W., (eds.): Oil and Gas in Alpidic Thrustbelts and Basins of Central and Eastern Europe. - EAGE Spec. Publ. No. 5*, pp. 217-235.

Wagner, L. R. (1998). Tectono-stratigraphy and hydrocarbons in the Molasse Foredeep of Salzburg, Upper and Lower Austria. In A. Mascle, C. Puigdefabregas, H. P. Luterbacher, & M. Fernandez , *Cenozoic Foreland Basins of Western Europe* (pp. 339-369). Geological Society Special Publications 134.

Witt, K. J. (2008). *Grundbau - Taschenbuch Teil1: Geotechnische Grundlagen.*

Wyllie, M. R., Gregory, A. R., & Gardner, L. W. (1956). Elastic wave velocities in heterogeneous and porous media. *Geophysics*, pp. 41-70.

Yilmaz, Ö. (2001). *Seismic Data Analysis: Processing, Inversion, and Interpretation of Seismic Data.* Society of Exploration Geophysicists.

Ziegler, P. A. (1982). *Geological Atlas of Western and Central Europe.* The Hague: Shell Internationale Petroleum Maatschappje.

Ziegler, P. A. (1987). Late Cretaceous and Cenozoic intra-plate compressional deformations in the Alpine foreland-a geodynamic model. *Tectonophysics, 137*, pp. 389-420.

Zoback , M. D. (2014). *Reservoir Geomechanics.* New York: Cambridge University Press.

10 APPENDIX

10.1 DENSITY CALCULATION

Density Equation	Zone
DenInn=2.01875214*Pow(VpInn,0.141327)	Innviertel Group
DenHall=2.01875214*Pow(VpHall,0.141327)	Hall Formation
DenUP=1.783400976*Pow(VpUP,0.27461)	Upper Puchkirchen Formation
DenLP=1.783400976*Pow(VpLP,0.27461)	Lower Puchkirchen Formation
DenRupelian=2.123215128*Pow(VpRupelian,0.123935)	Rupelian
DenDynow=2.123215128*Pow(VpDynow,0.123935)	Dynow Formation
DenFishS=2.123215128*Pow(VpFishS,0.123935)	Fish Shale
DenEO=1.365230556*Pow(VpEocene,0.409155)	Eocene
DenEoLST=1.365230556*Pow(VpEoLST,0.409155)	Litothamian Limestone
DenEoSST=1.365230556*Pow(VpEoSST,0.409155)	Eocene Sandstone
DenCon=2.273484512*Pow(VpConiacian,0.0919171)	Coniacian
DenTuronSST=1.851292322*Pow(VpTuronSST,0.257638)	Turonian Sandstone
DenTuronM=1.851292322*Pow(VpTuronM,0.257638)	Turonian Marl
DenCET1=2.225087019*Pow(VpCET1,0.0997267)	CET 1
DenCET2=1.364042808*Pow(VpCET2,0.440732)	CET 2
DenCET3=1.873755842*Pow(VpCET3,0.198046)	CET 3
DenJUBSS=1.873755842*Pow(VpJUBSS,0.198046)	JUBSS

10.2 POROSITY CALCULATION

Zone	Porosity Equation
Innviertel Group	PHIEF=If(Zone_log_linked_to_Zonation=0,(((DT_new-200)/(607-200))), U)
Hall Formation	PHIEF=If(Zone_log_linked_to_Zonation=2 ,(((DT_new-200)/(607-200))), PHIEF)
Upper Puchkirchen Formation	PHIEF=If(Zone_log_linked_to_Zonation=4,(((DT_new-210)/(607-210))), PHIEF)
Lower Puchkirchen Formation	PHIEF=If(Zone_log_linked_to_Zonation=6,(((DT_new-187)/(607-187))), PHIEF)
Rupelian	PHIEF=If(Zone_log_linked_to_Zonation=8 And Poro_Son>=0.1,((DT_new-187)/(607-187)), PHIEF)
Rupelian	PHIEF=If(Zone_log_linked_to_Zonation=9 And Poro_Son<=0.1,((DT_new-200)/(607-200)), PHIEF)
Rupelian	PHIEF=If(Zone_log_linked_to_Zonation=9 And Poro_Son>=0.1,((DT_new-200)/(607-200)), PHIEF)
Dynow Formation	PHIEF=If(Zone_log_linked_to_Zonation=10 And Poro_Son>=0.1,((DT_new-187)/(607-187)), PHIEF)
Fish Shale	PHIEF=If(Zone_log_linked_to_Zonation=11 And Poro_Son>=0.1,((DT_new-187)/(607-187)), PHIEF)
Litothamian Limestone	PHIEF=If(Zone_log_linked_to_Zonation=13,((DT_new-173)/(607-173)), PHIEF)
Eocene Sandstone	PHIEF=If(Zone_log_linked_to_Zonation=15,((DT_new-182)/(607-182)), PHIEF)
Turonian Sandstone	PHIEF=If(Zone_log_linked_to_Zonation=21 And Poro_Son>=0.1,((DT_new-187)/(607-187)), PHIEF)
Turonian Sandstone	PHIEF=If(Zone_log_linked_to_Zonation=21 And Poro_Son<=0.1,((DT_new-187)/(607-187)), PHIEF)
Coniacian	PHIEF=If(Zone_log_linked_to_Zonation=18 And Poro_Son>=0.1,((DT_new-155)/(607-155)), PHIEF)
Turonian Marl	PHIEF=If(Zone_log_linked_to_Zonation=23 And Poro_Son>=0.1,((DT_new-155)/(607-155)), PHIEF)
CET 1	PHIEF=If(Zone_log_linked_to_Zonation=26 And Poro_Son>=0.1,(((DT_new-182)/(607-182))), PHIEF)
CET 1	PHIEF=If(Zone_log_linked_to_Zonation=26 And Poro_Son<=0.1,(((DT_new-167)/(607-167))), PHIEF)
CET 2	PHIEF=If(Zone_log_linked_to_Zonation=28 And Poro_Son>=0.1,(((DT_new-182)/(607-182))*0.9), PHIEF)
CET 3	PHIEF=If(Zone_log_linked_to_Zonation=30 And Poro_Son>=0.1,(((DT_new-187)/(607-187))*0.9), PHIEF)
JUBSS	PHIEF=If(Zone_log_linked_to_Zonation=32,((DT_new-156)/(607-156)), PHIEF)

10.3 SHEAR SONIC VELOCITY CALCULATION

VsInn=If(Zone_log_linked_to_Zonation=0, 0.8423 *VpInn- 1.099, 0.7535 *VpInn - 0.6566)
Vs=If(Zone_log_linked_to_Zonation=0, VsInn, U)
VsHall=If(Zone_log_linked_to_Zonation=2 , 0.8423 *VpHall- 1.099, 0.7535 *VpHall - 0.6566)
Vs=If(Zone_log_linked_to_Zonation=2, VsHall, Vs)
VsUP=If(Zone_log_linked_to_Zonation=4 And PHIEF>=0.25, 0.8423 *VpUP- 1.099, 0.7535 *VpUP - 0.6566)
Vs=If(Zone_log_linked_to_Zonation=4, VsUP, Vs)
VsLP=If(Zone_log_linked_to_Zonation=6 And PHIEF>=0.25, 0.8423 *VpLP- 1.099, 0.7535 *VpLP - 0.6566)
Vs=If(Zone_log_linked_to_Zonation=6, VsLP, Vs)
VsRupelian=0.7700 * VpRupelian - 0.8674
Vs=If(Zone_log_linked_to_Zonation=8, VsRupelian, Vs)
Vs=If(Zone_log_linked_to_Zonation=10, VsRupelian, Vs)
VsDynow= -0.055 * Pow(VpDynow, 2) + 1.017 * VpDynow - 1.031
VsFishS= 0.7700 * VpFishS - 0.8674
Vs=If(Zone_log_linked_to_Zonation=11, VsFishS, Vs)
VsEoLST= -0.055 * Pow(VpEoLST ,2) + 1.017 * VpEoLST - 1.031
VsEoSST=If(Zone_log_linked_to_Zonation=15 And PHIEF>=0.15, 0.756 *VpEoSST- 0.662, 0.853 *VpEoSST- 1.137)
Vs=If(Zone_log_linked_to_Zonation=15, VsEoSST, Vs)
VsConiacian=0.7700 * VpConiacian - 0.8674
Vs=If(Zone_log_linked_to_Zonation=18, VsConiacian, Vs)
VsTuronSST=If(Zone_log_linked_to_Zonation=21 And PHIEF>=0.15, 0.756 *VpTuronSST- 0.662, 0.853 *VpTuronSST- 1.137)
Vs=If(Zone_log_linked_to_Zonation=21, VsTuronSST, Vs)
VsTuronM= -0.055 *Pow(VpTuronM,2) + 1.017 * VpTuronM - 1.031
Vs=If(Zone_log_linked_to_Zonation=23, VsTuronM, Vs)
VsCET1=If(Zone_log_linked_to_Zonation=26 And PHIEF>=0.15, 0.756 *VpCET1- 0.662, 0.853 *VpCET1 - 1.137)
Vs=If(Zone_log_linked_to_Zonation=26, VsCET1, Vs)
VsCET2=If(Zone_log_linked_to_Zonation=28 And PHIEF>=0.15, 0.756 *VpCET2- 0.662, 0.853 *VpCET2 - 1.137)
Vs=If(Zone_log_linked_to_Zonation=28, VsCET2, Vs)
VsCET3=If(Zone_log_linked_to_Zonation=30 And PHIEF>=0.15, 0.756 *VpCET3- 0.662, 0.853 *VpCET3 - 1.137)
Vs=If(Zone_log_linked_to_Zonation=30, VsCET3, Vs)
VsJUBSS=-0.055 * Pow(VpJUBSS, 2) + 1.017 * VpJUBSS - 1.031
Vs=If(Zone_log_linked_to_Zonation=32, VsJUBSS, Vs)
Vs=If(Zone_log_linked_to_Zonation=31, VsJUBSS, Vs)

10.4 CORE PLUG DATA

Probenbezeichnung	Durchmesser mm			Länge mm			Durchmesser Mittelw., mm	Länge Mittelw., mm	Volumen mm³	Volumen cm³	Masse (g)	Rohd. (g/cm³)
TRAT615	29,71	29,69	29,68	31,40	31,30	31,36	**29,7**	**31,4**	21711,6	21,71	**46,730**	**2,152**
TRAT604	24,83	24,96	24,78	17,84	18,72	18,21	**24,9**	**18,3**	8859,3	8,86	**18,290**	**2,065**
TRAT609	25,09	25,17	25,13	17,85	17,88	17,72	**25,1**	**17,8**	8836,9	8,84	**18,970**	**2,147**
TRAT801	25,13	25,09	25,09	19,98	20,20	20,38	**25,1**	**20,2**	9991,2	9,99	**18,970**	**1,899**
TRAT709	29,38	29,43	29,38	27,58	27,65	27,70	**29,4**	**27,6**	18761,9	18,76	**45,590**	**2,430**
TRAT712A	28,77	28,73	28,81	37,96	37,92	37,90	**28,8**	**37,9**	24655,5	24,66	**50,740**	**2,058**
TRAT712B	28,25	28,27	28,36	16,37	16,41	16,48	**28,3**	**16,4**	10323,6	10,32	**20,230**	**1,960**
TRAT701A	29,30	29,36	29,25	30,01	29,80	30,09	**29,3**	**30,0**	20209,8	20,21	**42,250**	**2,091**
TRAT701B	29,30	29,28	29,32	25,29	25,30	25,32	**29,3**	**25,3**	17060,9	17,06	**35,880**	**2,103**
TRAT704A	29,50	29,60	29,56	49,33	49,43	49,49	**29,6**	**49,4**	33898,2	33,90	**69,600**	**2,053**
TRAT704B	29,57	29,60	29,55	32,86	32,23	32,21	**29,6**	**32,4**	22278,3	22,28	**45,060**	**2,023**
TRAT705	29,55	29,56	29,61	33,14	33,21	33,28	**29,6**	**33,2**	22811,8	22,81	**46,310**	**2,030**
TRAT718	29,58	29,59	29,61	39,46	39,52	39,49	**29,6**	**39,5**	27162,2	27,16	**56,060**	**2,064**
TRAT714A	29,72	29,77	29,74	36,50	36,52	36,49	**29,7**	**36,5**	25363,1	25,36	**51,800**	**2,042**
TRAT714B	29,71	29,71	29,71	37,30	37,32	37,36	**29,7**	**37,3**	25877,0	25,88	**52,820**	**2,041**
TRAT714C	29,71	29,74	29,80	17,29	17,50	17,19	**29,8**	**17,3**	12044,2	12,04	**24,340**	**2,021**
TRAT714D	29,54	29,61	29,50	12,29	12,25	12,29	**29,6**	**12,3**	8419,5	8,42	**17,040**	**2,024**

10.5 WELL LOG PLOT TRAT1

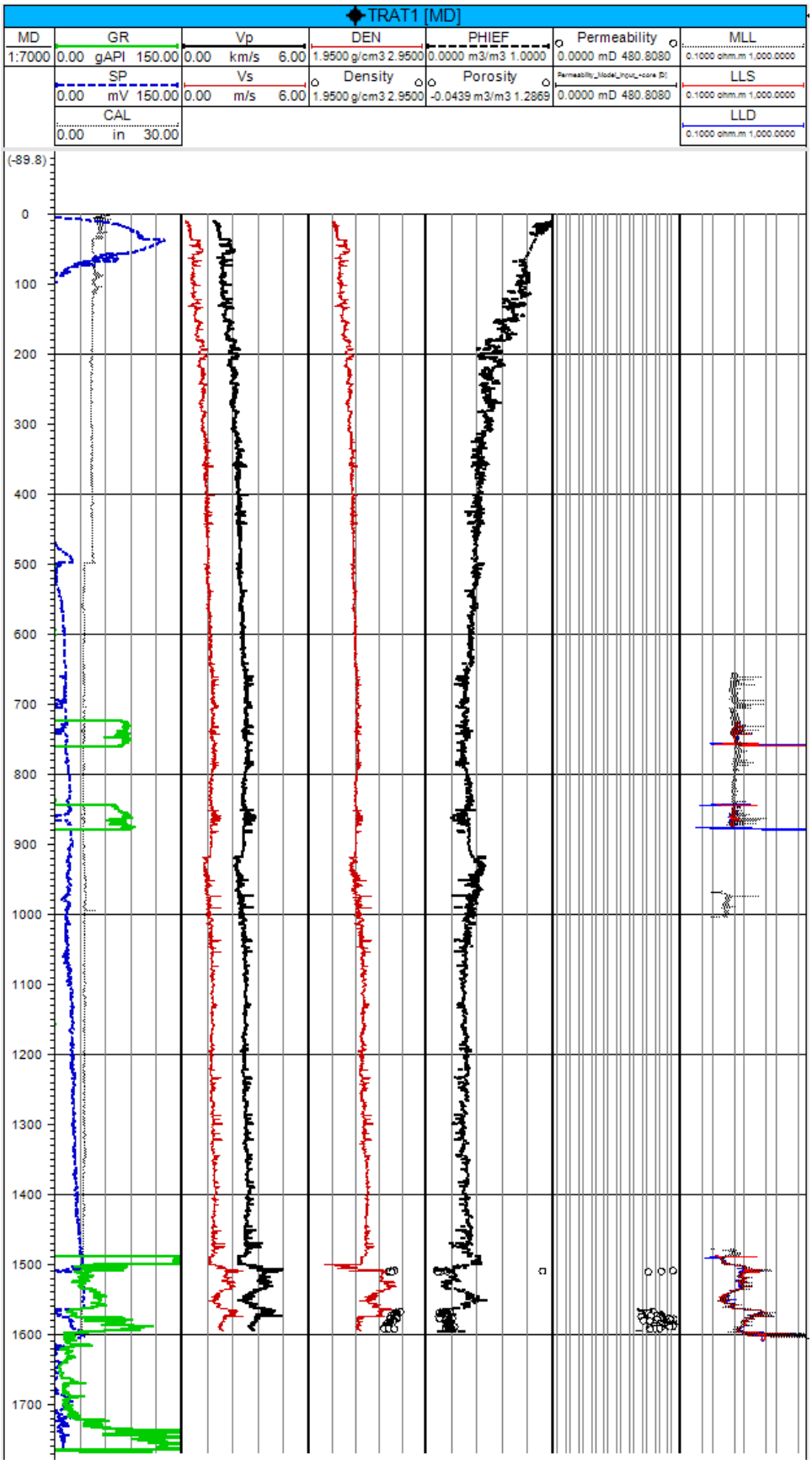

10.6 WELL LOG PLOT TRAT2

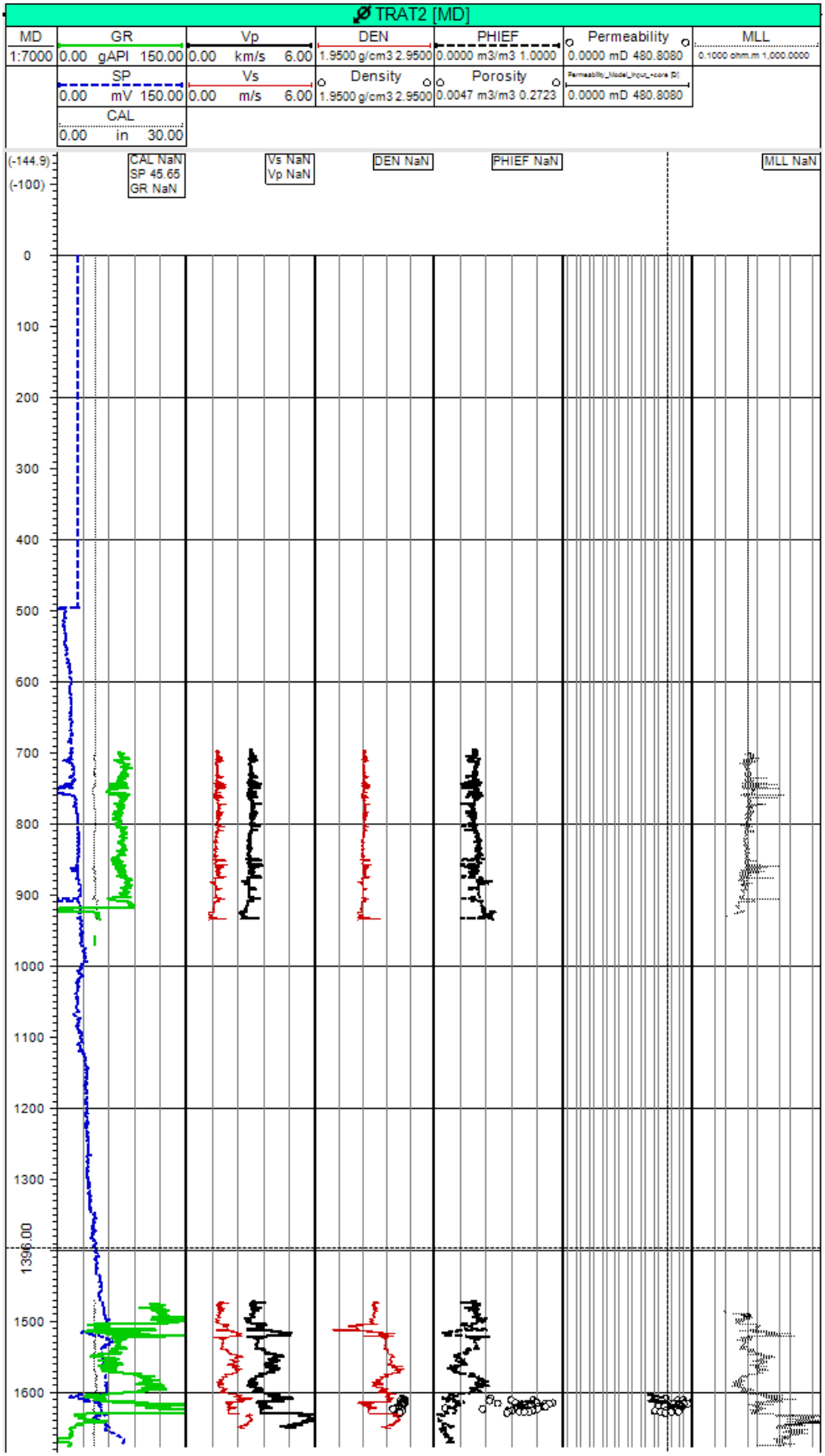

10.7 WELL LOG PLOT TRAT3

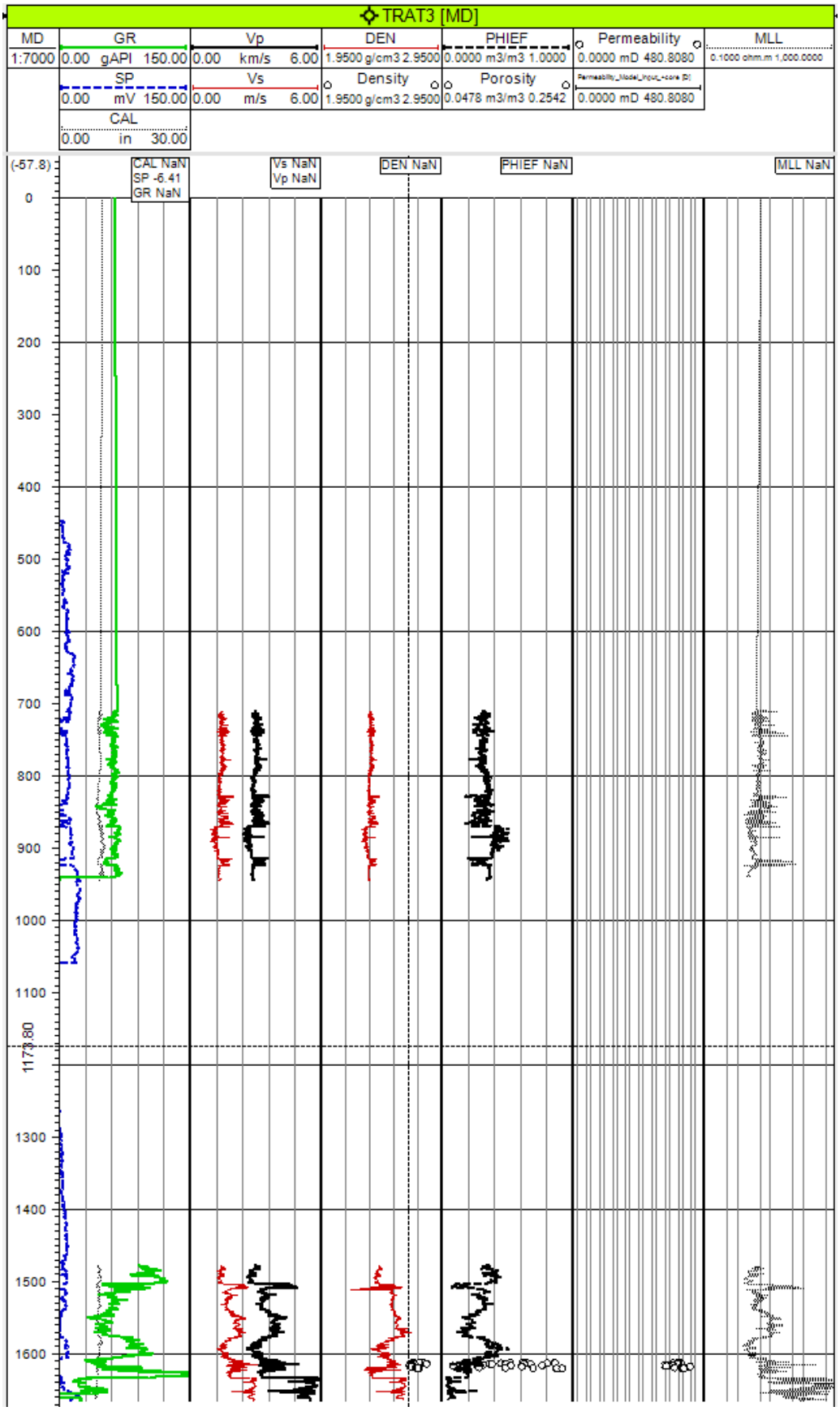

10.8 WELL LOG PLOT TRAT4

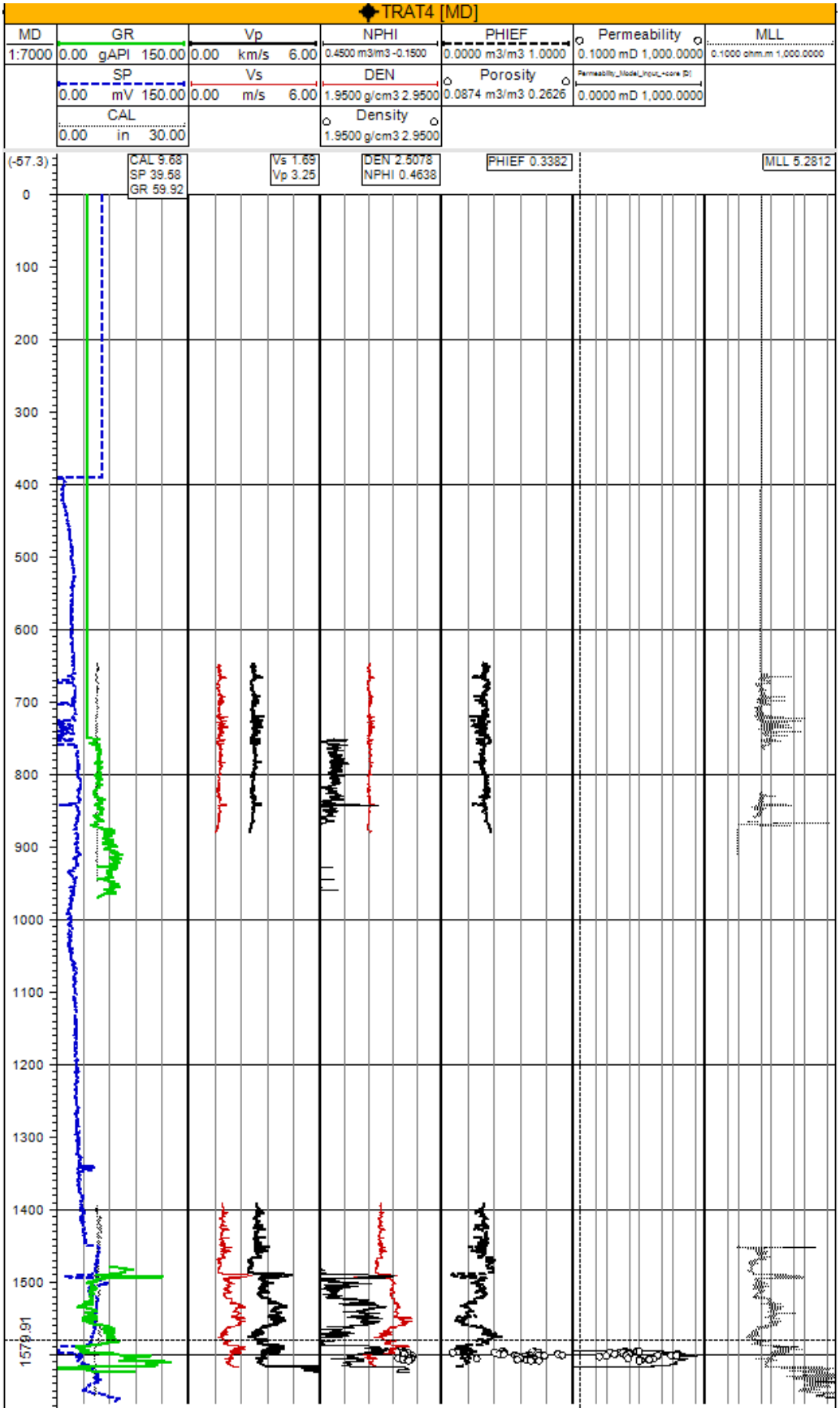

10.9 WELL LOG PLOT TRAT6

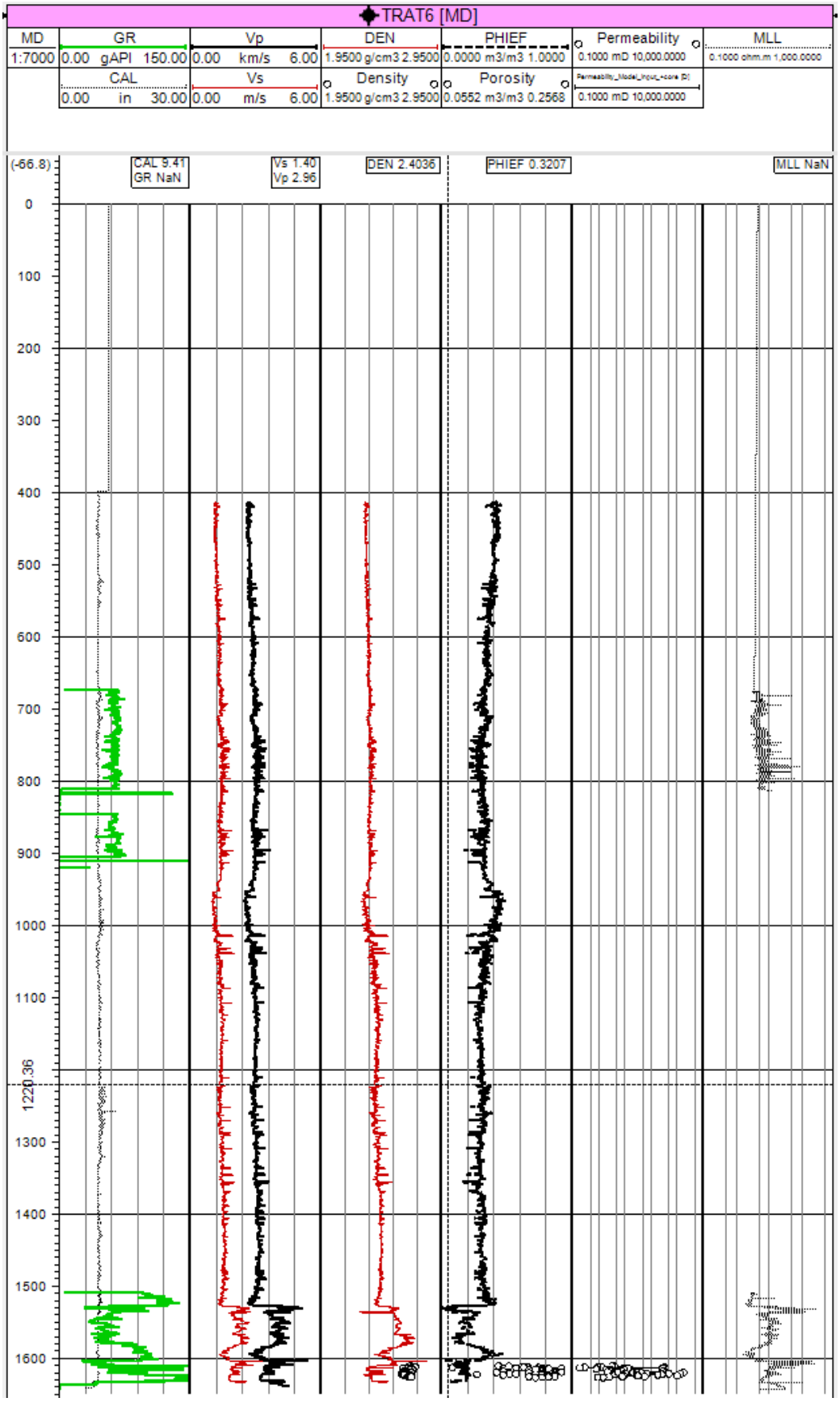

10.10 WELL LOG PLOT TRAT7

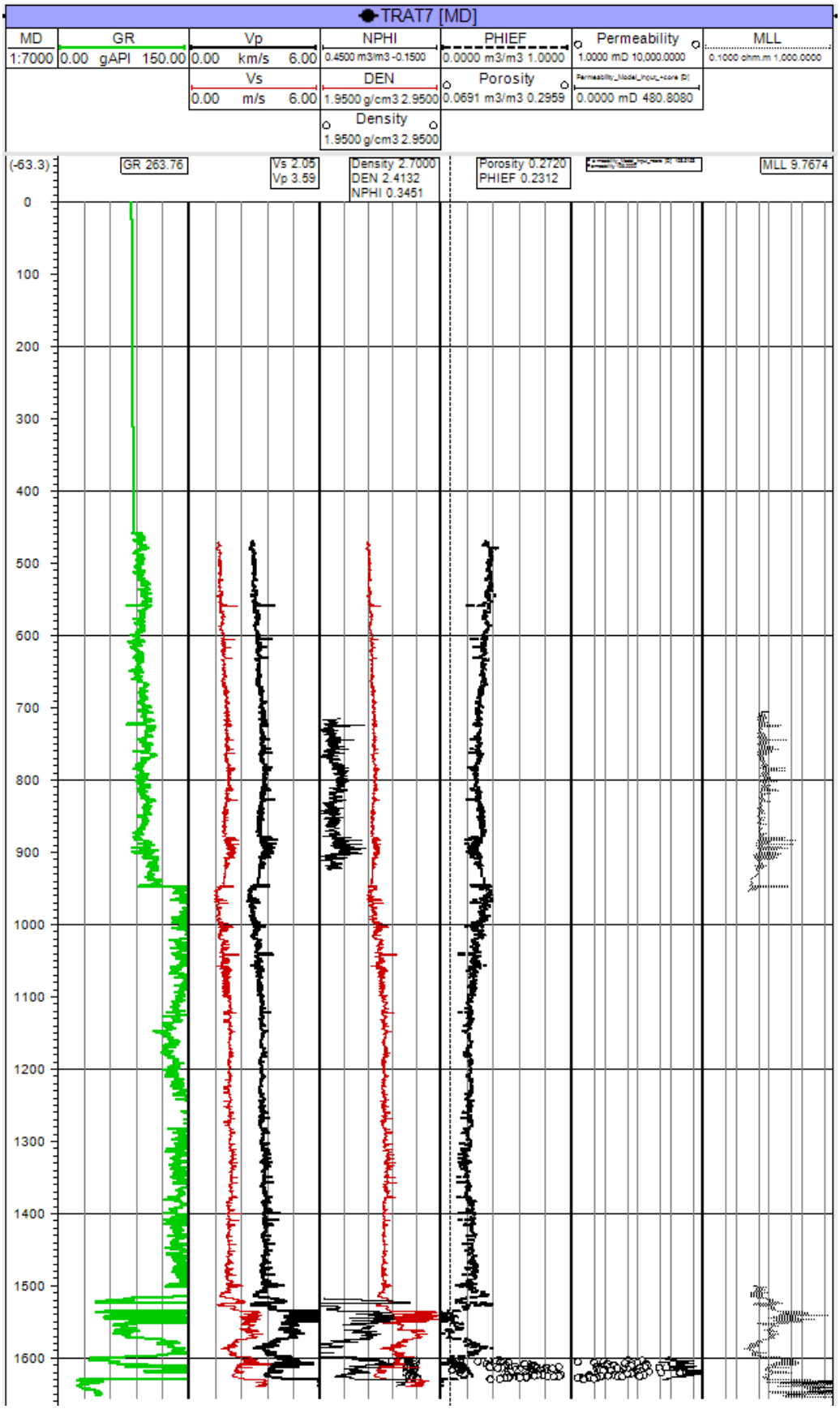

10.11 WELL LOG PLOT TRAT8

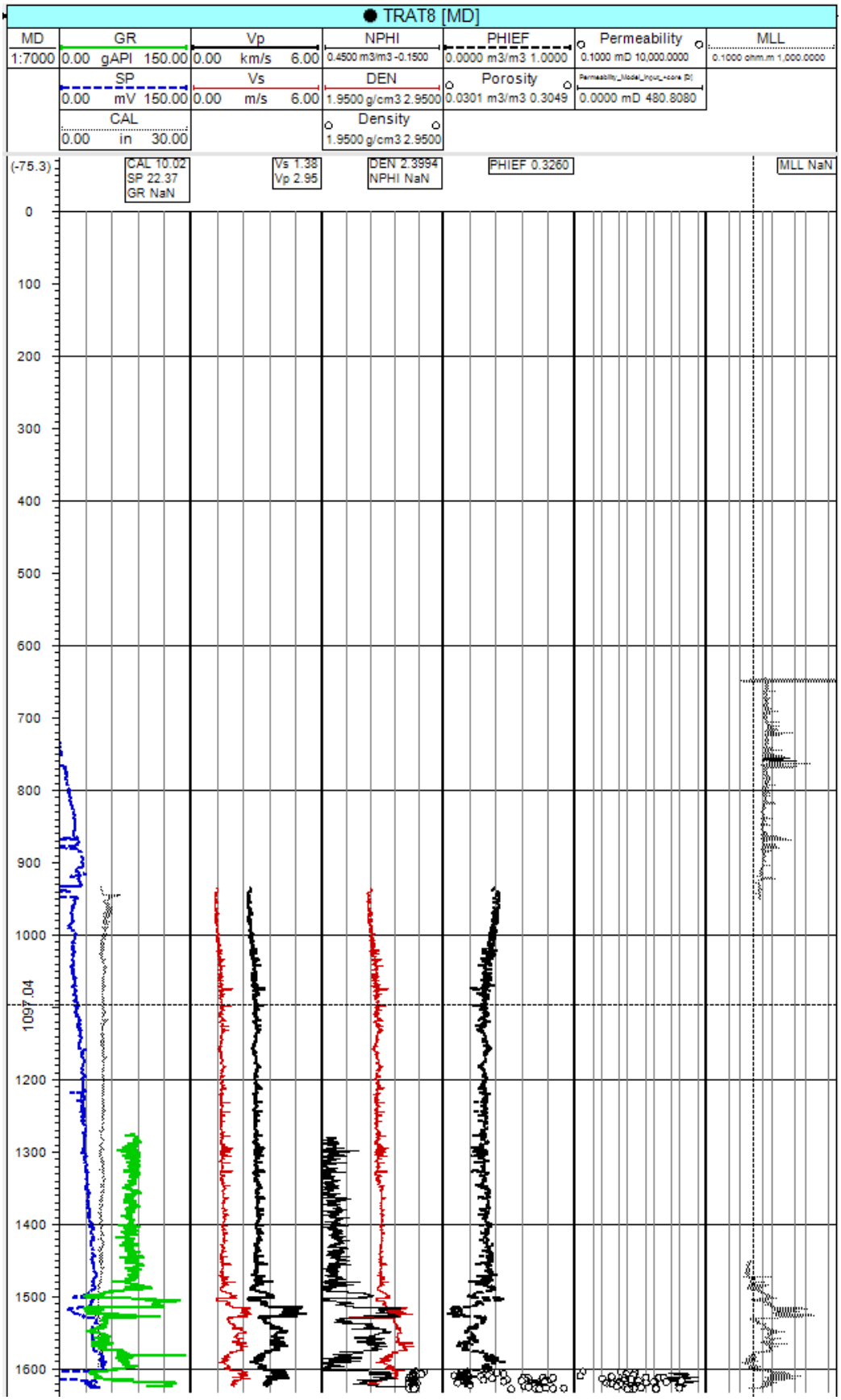

10.12 WELL LOG PLOT TRAT9

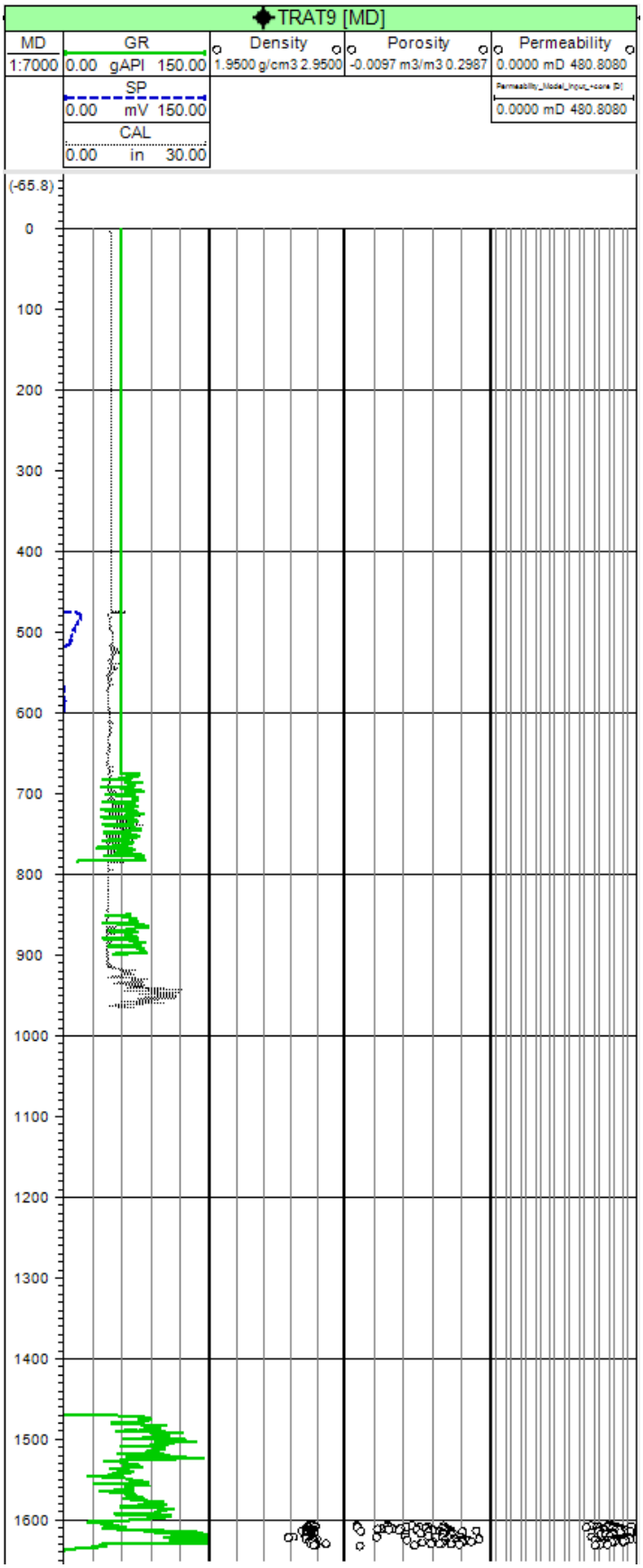

10.13 WELL LOG PLOT TRAT10

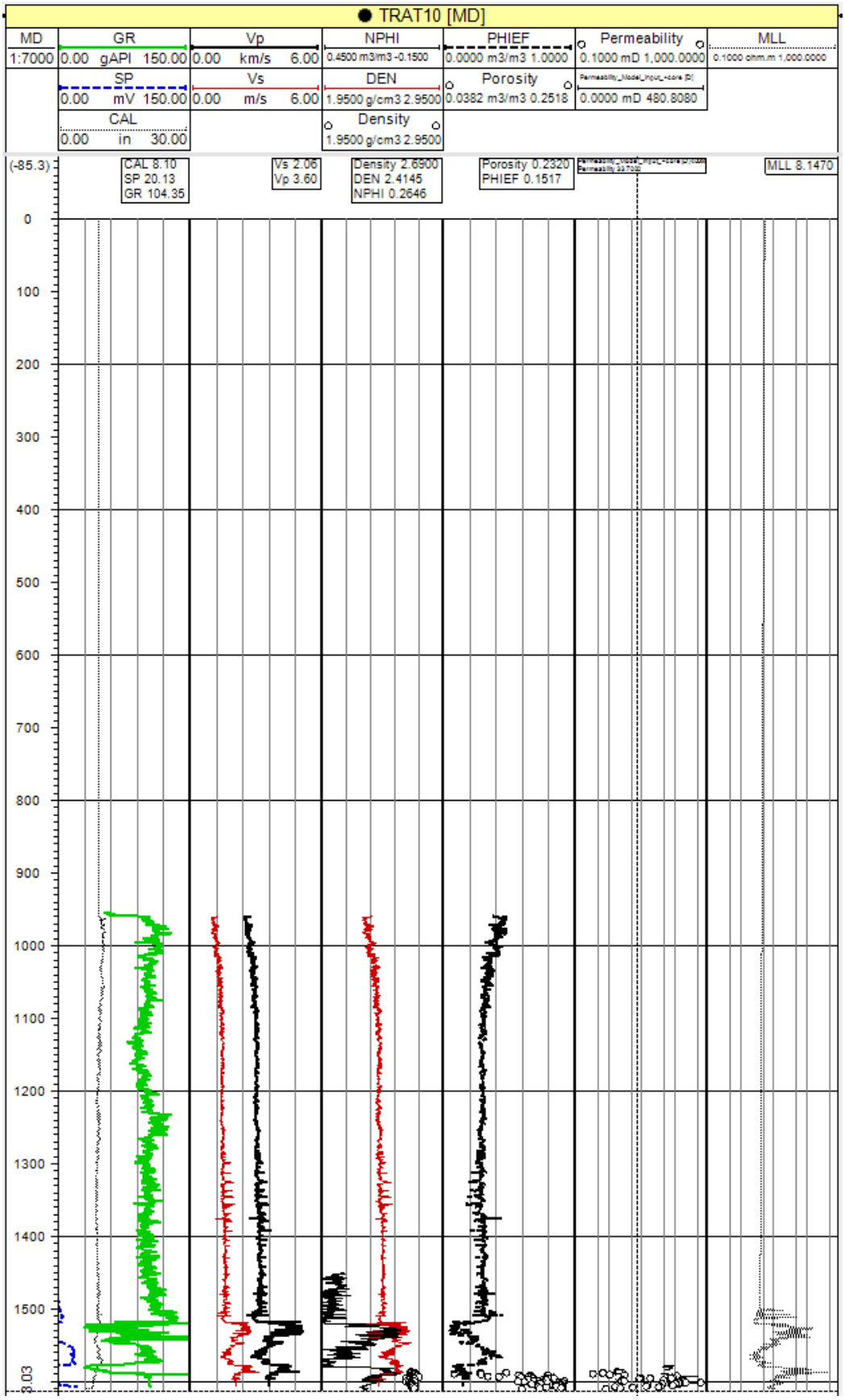

10.14 WELL LOG PLOT TRAT11

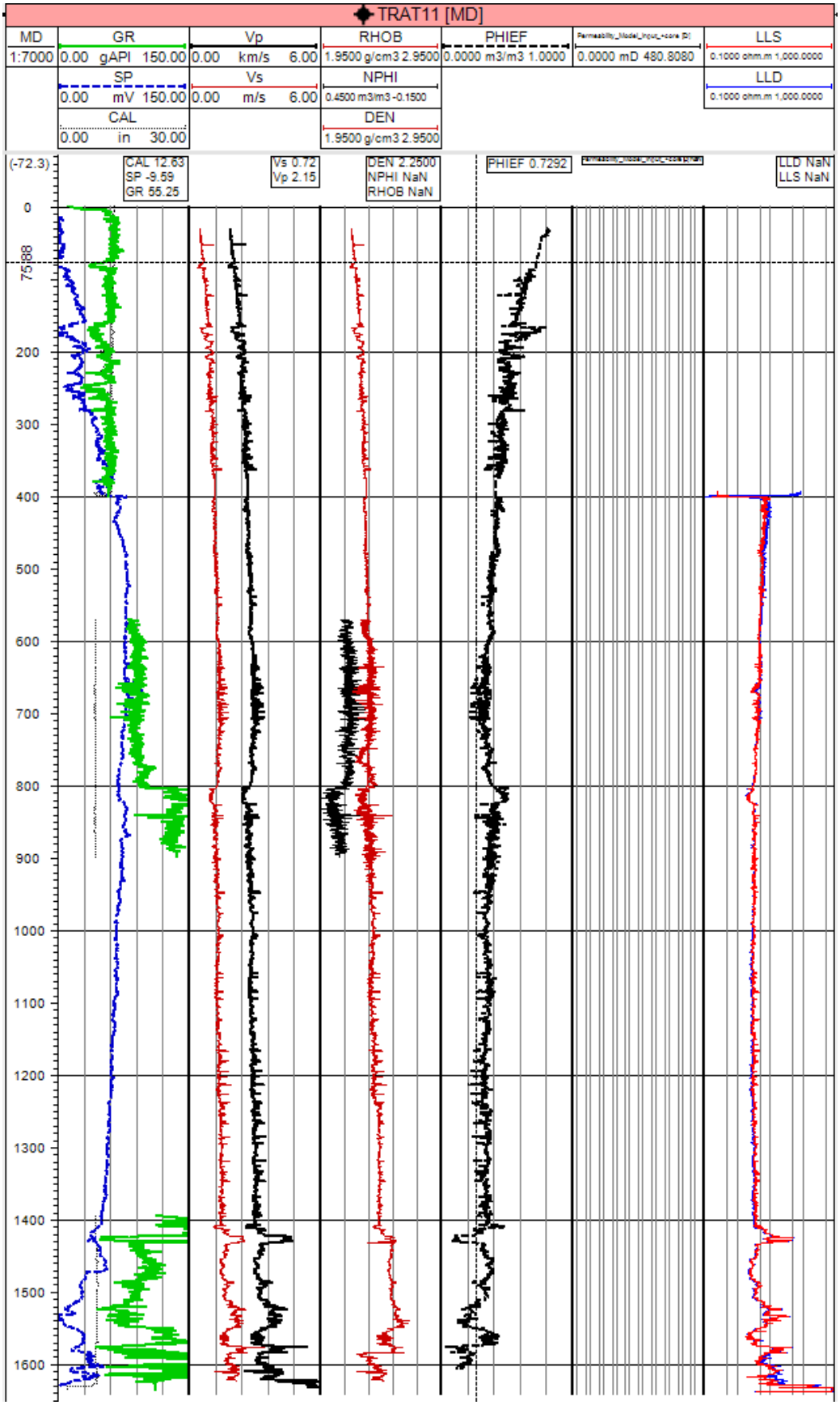

10.15 WELL LOG PLOT TRAT12

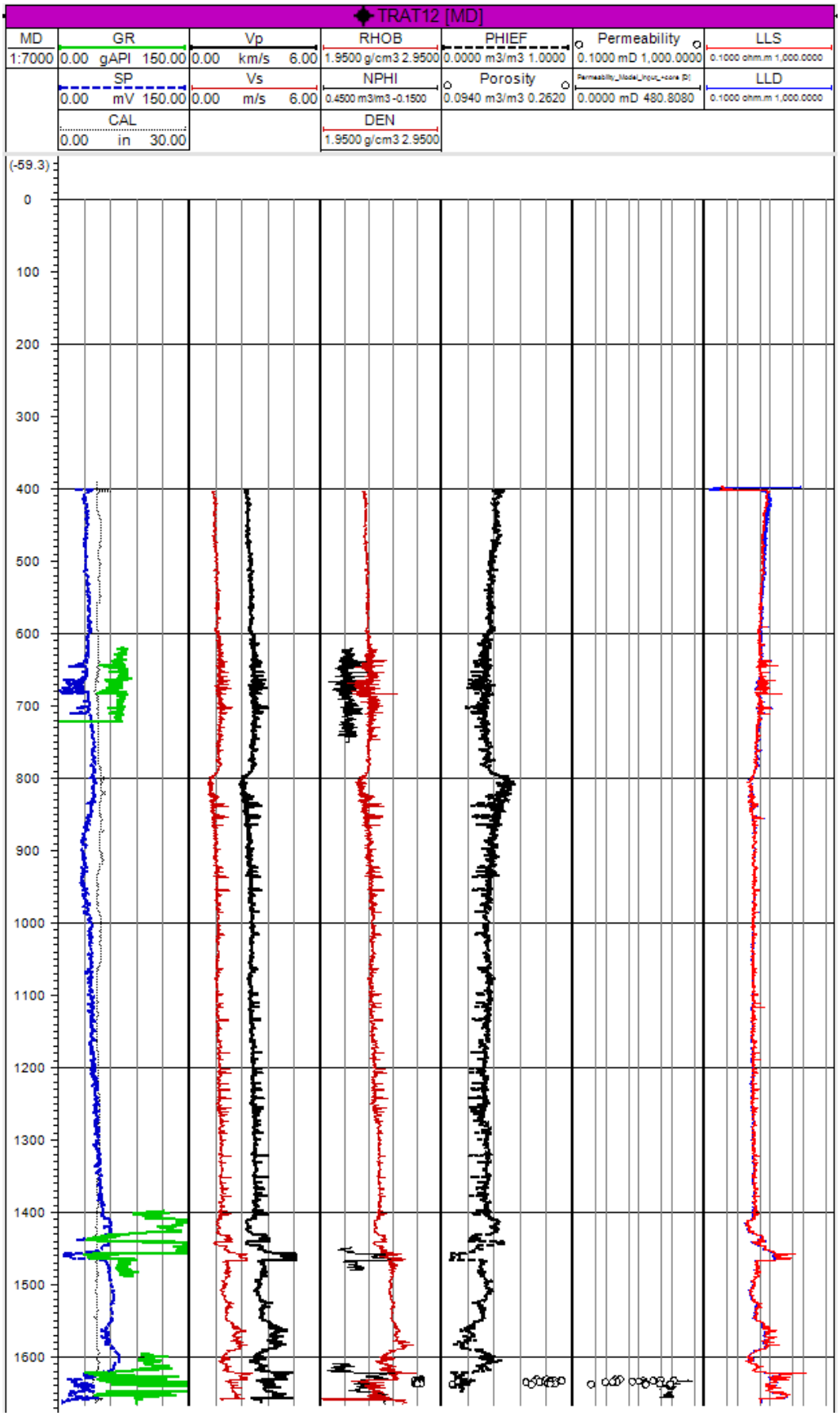

10.16 WELL LOG PLOT WEINBERG1

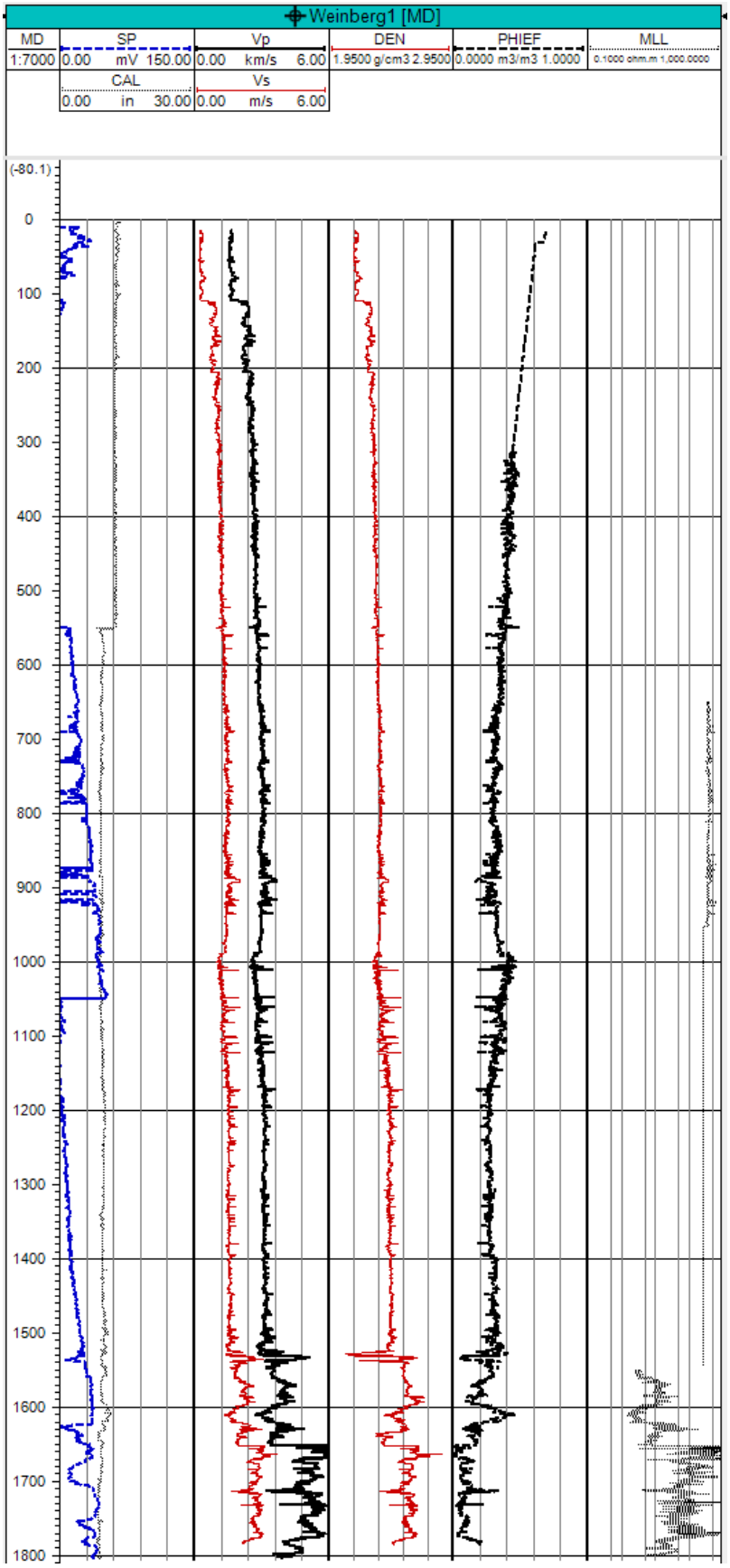

10.17 WELL LOG PLOT GASPOLDSHOFEN1